UC Santa Barbara
UC Santa Barbara Electronic Theses and Dissertations

Title
High-Temperature Growth of Gallium Nitride Using the Ammonothermal Method with Ammonium Chloride Mineralizer

Permalink
https://escholarship.org/uc/item/1tf7z2bm

Author
Malkowski, Thomas

Publication Date
2016

Peer reviewed|Thesis/dissertation

eScholarship.org Powered by the California Digital Library
University of California

UNIVERSITY OF CALIFORNIA

Santa Barbara

High-Temperature Growth of Gallium Nitride Using the Ammonothermal Method with Ammonium Chloride Mineralizer

A dissertation submitted in partial satisfaction of the

requirements for the degree Doctor of Philosophy

in Materials

by

Thomas Franklin Malkowski

Committee in charge:

Professor Steven P. DenBaars, Chair

Professor James S. Speck

Professor Shuji Nakamura

Professor Umesh Mishra

December 2016

The dissertation of Thomas Franklin Malkowski is approved.

James S. Speck

Shuji Nakamura

Umesh Mishra

Steven P. DenBaars, Committee Chair

October 2016

High-Temperature Growth of Gallium Nitride Using the Ammonothermal Method with Ammonium Chloride Mineralizer

Copyright © 2016

by

Thomas Franklin Malkowski

ACKNOWLEDGEMENTS

It would be nice to believe that one person can do everything on their own, but this is not true. Almost by definition, part of the nature of human beings seems to be the connection with others, whether it be to just a few or many. I would not call myself elegant, but I will try to acknowledge those who have helped me. Should this acknowledgment lack the required elegance owed to those named or any forgotten, it should be accepted that it is my fault and not due to any lacking of those mentioned.

Even in my most difficult times I have been blessed. Mom, Dad, Joe, and Ronni all have been champions of my efforts. From talks of general philosophy and the philosophy of the scientist as well as science itself to the specific discussions of my work, they have always been available to lend an ear. I know that perhaps not all of my explanations have made perfect sense, but I cannot stress how much I appreciate their willingness to listen regardless. When I was upset about how things were progressing, they always encouraged me and made me laugh. The greatest gift of any conversation is the birth of a contagious laughter. There were certainly plenty of difficult times during my research, but the presence of my family has made any such difficulties ghosts at the bottom of the ocean.

I would be not only callous but completely wrong to leave out those with whom I share no blood relation. I owe a deep debt of gratitude to my friends Bill Wolf, Sara Sterphone, Eric Rind, Brayden Ware, Hunter Banks, Srinivasan Venkatesh, and Jordan Axelson. I have on many occasions taken myself too seriously and perhaps made mountains from mole hills. But with their help I have been allowed to accept assistance when it is required. Through long conversations (and sometimes short ones), jokes, games, and just chatting I found that they have helped keep me human. It was (and perhaps still is) too easy to absorb oneself into work,

to fall fully into the research. This appears at first glance to be a good thing, but I cannot help but feel that this is not my destiny. I am not the sum of my work and I do not wish to be. With their help I have maintained my other dimensions, and for that I am utterly grateful. To Paul Von Dollen, Steven Griffiths, and Mo Abo Alreesh I owe many thanks for conversations about the essence of our work as well as random jokes. They have helped me put my work into perspective in both good and bad times. But on a more personal note, they have made work not just tolerable but fun. I cannot think of a better group to work with on a daily basis. If I am to reminisce with nostalgia upon my graduate work, it will be with these people in mind.

For enjoying the difficulties of becoming a graduate student and general good times both in class and out, I must thank many of my fellow students. Clayton Jackson, Luke Gordon, Matt Gebbie, Greg Su, Leah Kuritzky, Stacy Kowsz, Erin Kyle, Ben Yonkee, Andrew Espenlaub, and Rachel Koltun to name a few. I must also thank those who have helped enable me to do my job here. A special thanks goes to both Guy Patterson and Doug Rehn for skillfully crafting reactor parts that I so badly needed. A special thanks goes to Guy Patterson also for teaching me so much about machining and being unendingly patient with my lack of skill in that art. Truly without Guy and Doug, this project could never have occurred. I would also like to thank Siddha Pimputkar for our many conversations about reactor design and implementation. Thanks also go out to Tara Owens, Yukina Warner, Aldir Lopez, Sheryl Condino, Alison Woolery, and Jocelyn Guzman for the behind the scenes paperwork that allowed me to focus on research. I would also like to thank Youli Li, Tom Mates, and Mark Cornish for assistance with XRD, SIMS, and SEM, respectively, and keeping the instrumentation working so well. Without their efforts, data collection would be nearly impossible.

I must also thank my committee for their efforts in keeping me on track. With so many questions that need answering, sometimes it is difficult to choose which way to go. I must thank Professor Jim Speck for sitting through our group meetings and providing insight and encouragement. To paraphrase his words, bulk crystal growth is hard. While it seems like a strange statement, as a student I cannot emphasize how much I appreciate the understanding. I must also thank Professor Steve DenBaars for allowing me to join his group and for being incredibly patient with my progress. He allowed me the leeway to accomplish a very trying task, one that took much more time than I ever anticipated. I must also thank Professor Shuji Nakamura for his advice as well as allowing me to work in his lab. Similarly, I must thank Professor Umesh Mishra for his advice and generosity. As a blanket statement, I also want to thank my entire committee for being willing to serve in such a role without which this work would not have been possible.

VITA OF THOMAS FRANKLIN MALKWOSKI
October 2016

EDUCATION
May 2010
Bachelor's in Science in Engineering Physics with honors
University of Illinois at Urbana-Champaign
Minors in mathematics and materials science and engineering

PUBLICATIONS
T. F. Malkowski, S. Pimputkar, J. S. Speck, S. P. DenBaars, S. Nakamura. *Acidic Ammonothermal Growth of Gallium Nitride in a Liner-Free Molybdenum Alloy Autoclave*. Journal of Crystal Growth. In Press. DOI: 10.1016/j.jcrysgro.2016.07.045 (2016)

S. Pimputkar, T. F. Malkowski, S. Griffiths, A. Espenlaub, S. Suihkonen, J. S. Speck, S. Nakamura. *Stability of Materials in Supercritical Ammonia Solutions*. Journal of Supercritical Fluids. vol 110, pg 193-229 DOI: 10.1016/j.supflu.2015.10.020 (2016)

J. J. Adams, E. B. Duoss, T. F. Malkowski, J. A. Lewis, J. T. Bernhard. *Design of Spherical Meanderline Antennas*. Proceedings of the 2011 IEEE Antennas and Propagation Society International Symposium and UNSC/URSI National Radio Science Meeting. Pg 765-768 (2011)

J. J. Adams, E. B. Duoss, T. F. Malkowski, M. J. Motala, B. Y. Ahn, R. G. Nuzzo, J. T. Bernhard, J. A. Lewis. *Conformal Printing of Electrically Small Antennas on Three-Dimensional Surfaces.* Advanced Materials, vol 23, issue 11, pg 1335-1340 DOI: 10.1002/adma.201003734 (2011)

J. J. Adams, S. C. Slimmer, T. F. Malkowski, E. B. Duoss, J. A. Lewis, J. T. Bernhard. *Comparison of Spherical Antennas Fabricated via Conformal Printing: Helix, Meanderline, and Hybrid Designs.* IEEE Antennas and Wireless Propagation Letters, vol 10, pg 1425-1428. DOI: 10.1109/LAWP.2011.2178999 (2011)

B. Y. Ahn, S. B. Walker, S. C. Slimmer, A. Russo, A. Gupta, S. Kranz, E. B. Duoss, T. F. Malkowski, J. A. Lewis. *Planar and Three-Dimensional Printing of Conductive Inks*. Journal of Visualized Experiments, issue 58. 10.3791/3189 (2011)

ABSTRACT

High-Temperature Growth of Gallium Nitride Using the Ammonothermal Method with Ammonium Chloride Mineralizer

by

Thomas Franklin Malkowski

Gallium nitride (GaN) has become an important semiconductor for the optoelectronics and power electronics fields in the pursuit of high efficiency devices. However, the lack of a natural native GaN substrate has forced growth of GaN devices on foreign substrates such as sapphire, silicon carbide, and silicon. To further enhance efficiency and develop devices with longer lifetimes, the number of defects present in devices must be reduced. The development of a native GaN substrate of high crystalline quality would directly enable defect reduction.

The ammonothermal method of GaN growth has shown significant promise as a technique for the production of high quality GaN crystals of industrially significant size (crystals on the order of centimeters in the largest dimension). The ammonothermal method is a solvothermal method that uses a mineralizer (here ammonium chloride) with supercritical ammonia to transport GaN from a source material from one temperature zone to grow a seed crystal in another temperature zone. High pressures, high temperatures, and the presence of a highly corrosive chemistry make development of an economical growth reactor challenging. This

body of work outlines the development of a growth reactor capable of high temperature ammonothermal growth of GaN using ammonium chloride mineralizer.

Initial development of the ammonothermal reactor required identification of suitable reactor materials. A materials stability study was conducted by exposing samples of materials to the ammonothermal environment and measuring mass loss as well as any chemical or mechanical changes that occurred. An Inconel 625 alloy reactor was employed, although the reactor itself was somewhat susceptible to corrosion from the ammonothermal environment. The study yielded a subset of materials that may be suitable for use as gaskets and other single use items which include niobium, molybdenum, titanium, vanadium, tungsten, gold, and platinum. Alloys of molybdenum and cobalt may also be useful. High strength titanium-zirconium-molybdenum (TZM) was also identified as a corrosion resistant material and was selected for reactor design.

A TZM reactor was then designed and fabricated. Subsequent high pressure, high temperature tests indicated that TZM was essentially inert and growth of GaN crystals followed. All GaN growth was accomplished at or above 650°C using seed crystals grown by hydride vapor phase epitaxy. Seeds were characterized by micrometer measurements for growth thickness, x-ray diffraction (XRD) for crystalline quality, and secondary ion mass spectrometry (SIMS) for impurity concentrations. The growth quality appeared to match the seed quality as measured by XRD. Growth coloration ranged from slightly gray to green or yellow with growth rates up to 191 μm/day. Most seeds exhibited significant faceting at the edges of the sample, forming semipolar planes. SIMS was performed on a couple of samples which indicated oxygen concentrations of $\sim 10^{18}$ cm^{-3}.

Table of Contents

1. Gallium Nitride as an Optoelectronic Material 1
   - A. The GaN Unit Cell 2
   - B. Non-Native Substrates 6
     - ***Sapphire*** 7
     - ***Silicon Carbide (SiC)*** 9
     - ***Gallium Arsenide (GaAs)*** 11
     - ***Silicon*** 13
   - C. Hydride Vapor Phase Epitaxy (HVPE) of GaN 14
   - D. The Sodium (Na) Flux Method 17
   - E. The Ammonothermal Method 22
     - ***Basic Ammonothermal Growth*** 23
     - ***Acidic Ammonothermal Growth*** 29
2. Corrosion of Materials in the Ammonothermal Environment 34
   - A. Basic Ammonothermal Corrosion with Na Mineralizer 34
     - ***Pure Elements*** 36
     - ***Metal alloys*** 40
     - ***Carbides, Nitrides, and Oxides*** 43
   - B. Acidic Ammonothermal Corrosion 46
     - ***Pure elements*** 47
     - ***Metal Alloys*** 52
     - ***Carbides, Nitrides, and Oxides*** 54

C. Conclusions on the Corrosion Study 57

3. Design of a TZM Reactor and Bulk Growth of GaN with NH_4Cl Mineralizer at High Temperature 59

A. Design of a Tube Reactor Made of TZM 59

B. The Theory of Solvothermal Growth 74

Growth Far From Equilibrium 76

Growth Near Equilibrium 77

C. Ammonothermal Growth of GaN in a TZM Reactor Using NH_4Cl Mineralizer 78

Polycrystalline GaN and Heteronucleation 80

Methodology and Observations in Seeded Growth 85

Single Crystal Growth in a TZM Reactor Using NH_4Cl Mineralizer 92

LIST OF FIGURES

Figure 1. a) Conventional unit cell for wurtzite GaN. b) Primitve unit cell for wurtzite GaN. Note for both images, a3 goes into the page at an angle of 120° to a1 and a2 and at 90° to c. 4

Figure 2. Polarity and symmetry in c-plane and the c-direction. Slices of the c-plane are shown at different z-heights in a) and b). The red hexagon is to show the hexagonal symmetry of this plane. Panel c) shows the m-plane. The yellow arrows indicate the direction of the dipole moment between the N and nearest Ga atom. Note that the dipole moments all face in the same direction, leading to a spontaneous polarization field. 5

Figure 3. C-plane view of the sapphire (Al_2O_3) unit cell. The black hexagon is drawn in to demonstrate the hexagonal symmetry of the c-plane. 8

Figure 4. C-plane view of the SiC unit cell. The image shown is of the 6H-SiC polytype. Again, the red hexagon is to illustrate the hexagonal symmetry of the plane. 10

Figure 5. C-plane view of GaN in either the wurtzite or zinc blend form with N removed. Wurtzite GaN has only the green and blue Ga atoms, whereas the stacking sequence for the zinc blende GaN is green, blue, magenta, and then back to green. 11

Figure 6. The unit cell of zinc blende GaAs a) without the (111) plane and b) with the (111) plane (shown in gold). 13

Figure 7. Schematic of an HVPE reactor. The growth chamber is made of a high temperature ceramic, often quartz. 15

Figure 8. Schematic of a basic ammonothermal reactor used at UCSB. From ref. [100]. 23

Figure 9. Solubility vs temperature for ammonothermal systems with Na, K, or Cl mineralizers. From ref. [102]. 25

Figure 10. Absolute mass loss (top) and relative mass loss (bottom) of oxides in Na-NH_3 solution. 45

Figure 11. Inconel 625 reactor body after a run with NH_4Cl mineralizer. Yellow powder that was highly soluble in water was often found (left) as were red crystallites (right). The red crystallites were water soluble but took much longer to dissolve than the yellow powder. Note also the scaling and spalling of the walls on the right. 47

Figure 12. Plot of enthalpy change per Cl atom present in chloride crystals known to form. The light blue bar is the enthalpy of the NH_4Cl mineralizer, the reference for corrosion. It would be suspected that enthalpies with a less negative value are unlikely to form while more negative enthalpies are likely to form. The red line is a guide to the eye indicating the value of the NH_4Cl enthalpy. All cations left of NH_4Cl on the graph were not found to degrade by a chloride formation while those to the right are suspected to form chlorides in situ. 50

Figure 13. Hastelloy C-276 capsule before (left) and after (right) acidic ammonothermal run. NH_4Cl powder was placed directly inside the capsule and the cap was placed on top before the capsule was placed inside the

REACTOR. CRYSTALLITES FORMED ON THE INNER WALLS AND BOTTOM OF THE CAP AND PITTING WAS CLEARLY VISIBLE. 54

FIGURE 14. CONE-IN-CONE SEAL DESIGN. THE LIGHT GRAY IS A MALE COMPONENT WITH A MALE CONE, THE DARK BLUE IS THE FEMALE COMPONENT WITH THE FEMALE CONE. THE COLLAR CREATES A SURFACE THAT THE GLAND CAN EMPLOY A FORCE AGAINST TO PRESS THE MALE COMPONENT INTO THE FEMALE COMPONENT. 61

FIGURE 15. PHOTOGRAPH OF REACTOR MALE CONE LEADING TO THE HEAD ASSEMBLY. BOTH PLASTIC DEFORMATION (ESSENTIALLY AN INDENTATION OF THE METAL SURFACE DUE TO COMPRESSIVE STRESS) AS WELL AS SURFACE CRACKS ARE PRESENT. THE SURFACE CRACKS PROPAGATE AROUND MUCH OF THE CONE AND ARE SUSPECTED TO BE EITHER DUE TO THE UNSUPPORTED CONE OR COMPRESSIVE STRESS UPON SEALING. 63

FIGURE 16. BEAD SEAL DESIGN. THE SCHEMATIC (LEFT), THE CONE-IN-CONE BODY ADAPTED TO THE BEAD SEAL WITH A $1/16^{TH}$ RADIUS (MIDDLE), AND THE TOP VIEW OF THE BEAD SEAL (RIGHT). THE BEAD DESIGN REQUIRES A COMPLIANT GASKET TO PLASTICALLY DEFORM TO CREATE THE SEAL. 64

FIGURE 17. PRESSURE RATINGS FOR A CYLINDRICAL BODY WITH AN OUTER TO INNER DIAMETER RATIO OF 16:7. THE DIFFERENT METHODS FOR CALCULATING THE SAFE PRESSURE ARE SHOWN BY USING FAUPEL'S BURST PRESSURE FORMULA, THE ASME PRESSURE GUIDELINE FOR MONOBLOCK CYLINDERS, AND THE VON MISES STRESS CALCULATION TO ENSURE THE INNER WALL STRESS IS LESS THAN THE YIELD STRESS OF THE MATERIAL. THE FAUPEL BURST PRESSURE INCLUDES A SAFETY FACTOR OF 4. 66

FIGURE 18. SCHEMATIC OF TZM REACTOR USED TO GROW GAN WITH NH_4CL. THE TOP BAFFLES ARE USED TO SEPARATE THE COLD ZONE FROM THE HEAD ASSEMBLY AND THE

bottom baffle is used to separate the hot and cold zones. The brown components are the valve (left) and the pressure transducer (right) and are made of stainless steel. Dashed regions indicate where insulation is present outside the reactor. 72

Figure 19. Hot zone after a growth run. T_{COLD} = 500°C, T_{HOT} = 650°C, P~100 MPa. 80

Figure 20. Scanning electron micrograph of white powder collected from the head assembly of a growth run. Ga and Cl atomic concentrations were measured at 29% and 71%, respectively. 83

Figure 21. Gallium oxide mesa on a GaN template. The atomic composition as measured by EDX are as follows: Ga 31%, O 60%, N 8%, Cl 1%. The material was grown in normal solubility conditions with a hot zone at 535°C and a cold zone at 245°C. 84

Figure 22. Furniture setup for a growth run. The GaN source and seeds are in position for retrograde solubility. Holes similar to the seed mount holes are present around each baffle. When wire is fed through these holes around the baffles, the baffle is locked in place. The top right and bottom right images show the GaN source and seed, respectively. 86

Figure 23. Images of 160415I A1 a) before and b) after and 160415I c) before and d) after growth. Each small square division is 1 mm on a side. 95

Figure 24. XRD of sample 160415I A1 before and after growth. Note that the peak does not significantly alter its FWHM, indicating that the quality of the seed is reproduced in the grown material. 95

FIGURE 25. OPTICAL IMAGES OF 160517I A1 A) BEFORE GROWTH AND B) AFTER GROWTH AS WELL AS 160517I A2 C) BEFORE GROWTH AND D) AFTER GROWTH. NOTE THE LACK OF COLORATION IN THE GROWN MATERIAL ON A1, ALTHOUGH THERE IS A SLIGHT GRAY TINT, LIKELY DUE TO FREE CARRIER ABSORPTION. PANELS C) AND D) ILLUSTRATE THE ETCHING THAT OCCURRING, ESPECIALLY AROUND THE HIGHLY DEFECTIVE STRIPES FROM THE LEO GROWTH. 98

FIGURE 26. XRD DATA FOR SAMPLE 160517I A1. NOTE THAT FOR BOTH SIDES, THE GROWN MATERIAL HAS A LARGER FWHM, WHICH MAY INDICATE DEFECT FORMATION. HOWEVER, THE SPREAD IN WHERE THE PEAKS ARE CENTERED ALSO INDICATES THAT THE BEAM DIRECTION IS NOT THE SAME FOR THE BEFORE AND AFTER GROWTH MEASUREMENTS. DUE TO THE LEO STRIPES PRESENT, DIFFERENT BEAM DIRECTIONS MAY HAVE SIGNIFICANTLY DIFFERENT FWHM AND EVEN SOMEWHAT DIFFERENT PEAK SHAPES.......... 98

FIGURE 27. SIMS DATA FOR 160517I A1 AFTER GROWTH. C, O, AND CL (THE DATA WITHOUT SYMBOLS) WAS TAKEN USING A CE GUN. AL, FE, MO, NB, AND TI (DATA WITH SYMBOLS AND LINES) WAS TAKEN USING AN O GUN. NOTE THAT THE DEPTHS ARE ESTIMATES, AS THE SEED SURFACE WASN'T COMPLETELY PLANAR AND NO DEPTH MEASUREMENT WAS MADE TO DETERMINE THE EXACT ETCH DEPTH. THE AL CONCENTRATION IS SOMEWHAT ANOMALOUS, AS NO REACTOR COMPONENT HAS AL AS AN ALLOYING ELEMENT OR COMMON IMPURITY. HOWEVER, THE NB GASKETS WERE POLISHED ON AN AL BLOCK, AND THUS THE AL CONCENTRATION MAY COME FROM THE POLISHING METHOD AND THEREFORE THE GASKETS. 99

Figure 28. Optical images of 160604I A1. Images are taken normal to the c-plane a) before and b) after growth. Images inclined to the c-plane c) before and d) after growth. Growth rates measured at positions 1-5 are as follows: 1-175 μm/day, 2-97 μm/day, 3-136 μm/day, 4-148 μm/day, and 5-82 μm/day. Note the faceting at positions 1 and 3. 101

Figure 29. XRD ω-scan of 160604I A1. The large shift between peaks may be from slight misalignment of the sample on the XRD mount or a rotation with respect to the LEO grown material. It is interesting to note the increased separation of the peaks after growth. The distinct peaks indicate multiple grains are present and are illuminated by the x-ray beam. 101

Figure 30. Optical images of 160614I A1 normal to the c-plane a) before and b) after growth and tilted from the c-plane c) before and d) after growth. Growth rates for positions 1-4 shown in d) are as follows: 1-48 μm/day, 2-32 μm/day, 3-145 μm/day, 4-96 μm/day. Note the step in d) around the edges of the sample and the smoother surface of the thicker step compared to the rounded surface in the sample center. 103

Figure 31. XRD data for 160614I A1 before and after growth. Note the large number of peaks that are present as seen in other samples. 103

Figure 32. XRD data for $(20\bar{2}1)$ of 160614I A1. Note that the FWHM is essentially the same, but again a new peak appears to be present closer to where the original peak was. 104

Figure 33. Optical images of 160630I A1 normal to the c-plane a) before and b) after growth and tilted with respect to the c-direction c) before and d)

after growth. The seed fractured during removal from the reactor rather than before or during the run. 105

Figure 34. XRD of $(\mathbf{0002})$ plane of 160630I A1. Due to the fracturing of the seed, the front and back side of the sample could not be distinguished. However, it can be seen that the red face before (at 18.72°) has essentially the same FWHM as both peaks after growth. The peak at 19.2° has two FWHM indicated because the fit was best for two Gaussian peaks centered at nearly the same coordinates with similar peak intensity but different FWHM. 106

Figure 35. XRD of $(\mathbf{1011})$ plane of 160630I A1. The significant increase in the FWHM may be due to deterioration of the crystal quality. 106

Figure 36. Optical images of 160707I A1 normal to the c-plane a) before and b) after growth and tilted from the c-direction c) before and d) after growth. Note the step formed in panel d, similar to prior growths.............................. 108

Figure 37. XRD data of $(\mathbf{0002})$ peaks of 160707I A1. Note the peak after growth was best fit with two Gaussian peaks and thus has two FWHM associated with it. 108

Figure 38. XRD data for $(\mathbf{2021})$ peak of 160707I A1. The exceptionally narrow peak is indicative of high quality material. 109

Figure 39. Optical images of 160714I a) A1 before growth and b) A1 after growth as well as c) A2 before growth and d) A2 after growth. Note that the seeds were grown at the same position in the reactor and the growth on A1 (panel b) is much thicker than the growth on A2 (panel d). 110

FIGURE 40. OPTICAL IMAGES OF A) 160517I A1, B) 160604I A1, AND C) 160614I A1. ARROWS INDICATE WHERE THE FACETING INCLINED BETWEEN THE M-PLANE AND C-PLANES IS OCCURRING. 115

FIGURE 41. OPTICAL MICROGRAPHS OF FACETS ON A) 160517I A1, B) AND C) 160604I A1, D) AND E) 160614I A1. NOTE ALL SEMIPOLAR PLANES OBSERVED HAVE M-PLANE CHARACTER. 116

1. Gallium Nitride as an Optoelectronic Material

"But what can be the attraction of getting to know such a tiny section of nature so thoroughly, while one leaves everything subtler and more complex shyly and timidly alone?"
-Albert Einstein, *Address on the occasion of Max Planck's 60th birthday*

Gallium nitride (GaN) is a compound semiconductor that has found significant use in the last three decades following the demonstration of the first bright blue light-emitting diode (LED). It is generally alloyed with aluminum nitride (AlN) or indium nitride (InN) to achieve the desired bandgap and thus the desired emission wavelength. Using the indium nitride-gallium nitride (InGaN) alloy system, light emitters with wavelengths spanning the entire visible spectrum can be achieved.[1] The impact of the blue GaN LED has had such a significant impact that a Nobel Prize was awarded to Isamu Akasaki, Hiroshi Amano, and Shuji Nakamura for its invention.[2] Much has happened in the development of GaN devices since the invention of the blue LED and GaN technology has spread to use in laser diodes (LDs) as well as power electronics.[1,3,4]

The expansion of GaN into all of these technological sectors initially proceeded without the use of native GaN substrates (substrates made out of GaN). Early LEDs and LDs were grown on sapphire, silicon carbide (SiC), or silicon.[5–9] GaN does not exist naturally and thus any native GaN substrate must be created artificially. Heteroepitaxial GaN, GaN grown on any substrate that is not GaN, was thus preferred. Although native substrates are now somewhat available, they are still quite expensive. The most common method to enable high quality GaN layers on non-native substrates is to grow a low temperature buffer layer. These buffer layers are either AlN or GaN.[5,8,10,11] The buffer layer is grown at low temperature and starts as an amorphous material, eventually recrystallizing as the GaN is grown on top. In the case of AlN, the buffer layer begins as a partially amorphous film that recrystallizes as the

temperature is increased to begin GaN growth.[12] In the case of a GaN buffer layer, the metastable cubic phase and the thermodynamically stable hexagonal phase initially form mixed together with a huge number of defects. Heating of the film to the growth temperature allows reorientation of the grains as well as coalescence.[11] In both cases, the buffer layer serves to partially break the coherence between the sapphire (or other non-native substrate) and the resulting GaN film, thus relaxing some of the strain.[13] Another method to allow highly strained coherent layers to be grown is the use of superlattices.[14] Such a practice is common for multi-quantum well (MQW) structures for LDs and LEDs. Superlattice structures are commonly used in the active region (the light emitting region) of optoelectronic devices because the In that is used to reduce the bandgap to achieve the desired emission/absorption wavelength also induces strain.[1,7,15,16] As the native GaN substrate is still in development, we will begin with a discussion of the common non-native substrates. But first we must understand the native structure of GaN to identify how it will interact with a given substrate.

A. *The GaN Unit Cell*

The phrase "epitaxial growth" by its very definition requires that there is a definite relationship between the crystal structure of the substrate and the material grown on top of it. Thus, the choice of substrate can have a very dramatic impact on the quality of the resulting growth. The substrate and the epitaxial film (the "epi-film") should then have the same or at least similar crystal structure. The 2D nature of the interface between the substrate and the epi-film relaxes this constraint a bit further and allows epitaxial growth as long as the symmetry of the interfacing planes is the same. Gallium nitride has the wurtzite crystal structure while sapphire and Si have the corundum and diamond crystal structures, respectively. SiC has many different crystal structures, but they are essentially stacks of

hexagonal packing and zinc blende regions. Zinc blende (more appropriately called sphalerite) is the cubic analog to the wurtzite structure and metastable GaN can be grown in the zinc blende structure. [17–19] From here forward, referencing the GaN crystal structure will be referring to the wurtzite crystal structure unless it is specifically stated otherwise. Because of the different structures and symmetries possible, it is prudent to analyze the GaN crystal structure before we consider how it would interact.

The wurtzite crystal structure is a hexagonal crystal structure and can be defined by two lattice constants, c and a. The c-axis (which has a repeat distance of c) is orthogonal to the hexagonal symmetry, while the a1, a2, and a3 axes (all of which have a repeat distance of a) form the plane containing the hexagonal symmetry. An image of the conventional GaN unit cell is shown Figure 1a. Figure 1b details the primitive unit cell for GaN. The unit cells convey the same information, but do so in different ways. The conventional unit cell is easier for the human to analyze the structure and see which atoms are placed where. The primitive unit cell is the smallest true repeat unit of the crystal structure. Note that the primitive unit cell contains two Ga and two N and has only one lattice point while the conventional unit cell contains eight Ga and eight N. It is important to note that the a3 axis is actually redundant in naming of planes. If one considers the hkil plane (formed by considering where the plane intersects each axis and then taking the reciprocal of that to get the number that would correspond to h,

k, i, or l), then based on the symmetry of the cell, i is always defined by –(h+k).

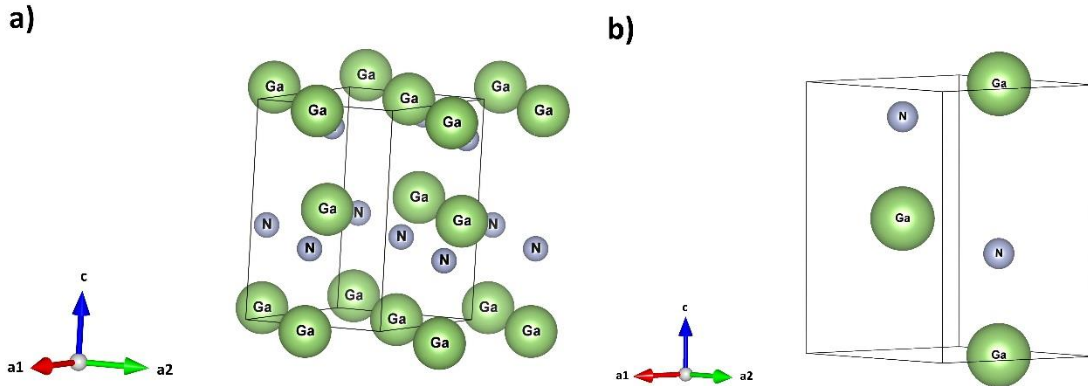

Figure 1. a) Conventional unit cell for wurtzite GaN. b) Primitve unit cell for wurtzite GaN. Note for both images, a3 goes into the page at an angle of 120° to a1 and a2 and at 90° to c.

There are several major families of planes that are commonly discussed in GaN. These are the $\{10\bar{1}0\}$ (or m-plane), $\{11\bar{2}0\}$ (or a-plane), and {0001} (or c-plane). The spontaneous polarization is in the c-direction and thus c-plane has the highest polarization. This spontaneous polarization field can affect devices in the form of the quantum confined Stark effect (QCSE), where the polarization field serves to separate electrons and holes. In light-emitting devices, this spatial separation of holes and electrons reduces the efficiency of the radiative process and thus reduces the efficiency of the device. The QCSE also serves to shift wavelength at low current densities, but at higher current densities the impact of the polarization field is reduced and an effective blue shift occurs.[20] Both m-plane and a-plane are orthogonal to c-plane and have no spontaneous polarization field, although they can have a piezoelectric polarization field due to lattice strain. Obviously, many other planes exist but some important semipolar planes (planes with an inclination less than 90° to c-plane) include

$\{20\bar{2}1\}$ and $\{11\bar{2}2\}$.[1,20] The spontaneous polarization field occurs due to the polar bonding between Ga and N as well as the lack of symmetry normal to the c-plane. Within the c-plane we have layers of either Ga or N atoms that are symmetric as shown in Figure 2a and 2b. The symmetry of these sheets prevents any polarization field from forming, thus any direction that is orthogonal to the c-direction has no polarization field. However, if we look in the c-direction in m-plane, for example, we see that there is an uneven spacing between Ga and N. This uneven spacing allows dipole moments that exist in the same direction and thus create a polarization field (see Figure 2c).

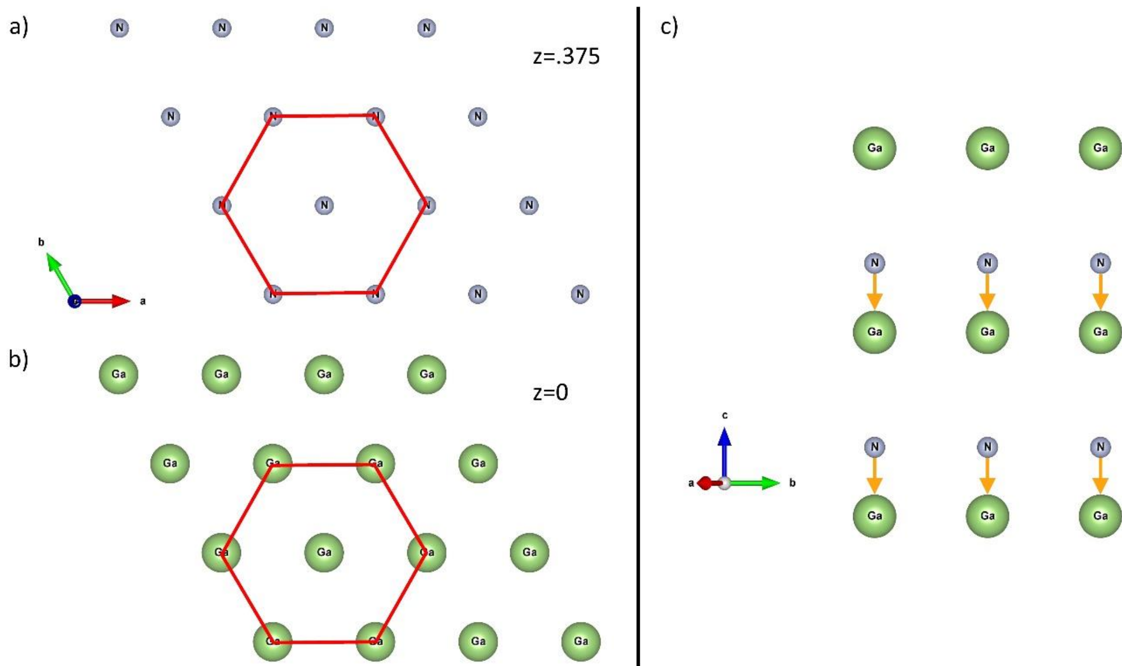

Figure 2. Polarity and symmetry in c-plane and the c-direction. Slices of the c-plane are shown at different z-heights in a) and b). The red hexagon is to show the hexagonal symmetry of this plane. Panel c) shows the m-plane. The yellow arrows indicate the direction of the dipole moment between the N and nearest Ga atom. Note that the dipole moments all face in the same direction, leading to a spontaneous polarization field.

Although often polarization fields can be a hindrance, they can also serve a purpose. One major use is the polarization locking of the emitted photons. This can be found most readily

in light-emitting devices on planes such as $(11\bar{2}2)$.[21,22] The polarization field here is actually a piezoelectric field induced by the strain in the heterojunctions. GaN is a piezoelectric crystal, which means as GaN is strained it develops an internal electric field. The field serves to separate the three valence bands that are primarily formed by the sp3 hybridization of the N p-orbitals. The separation of the valence bands causes a preferential transition which yields a particular polarization of the photon. The degree of separation between bands strongly impacts the ratio of the photon polarization and thus determines how polarized the emitted photons are.[21,23,24] The piezoelectric properties of GaN means it can be used in microphones or piezoelectric sensors to convert electrical signals into sound and vice versa as well as function as a filter.[25,26] While certain planes are mentioned above, the formation of the piezoelectric polarization is not a special case. Any device with regions that contain heterojunctions will almost certainly have lattice mismatch and thus lattice strain leading to polarization fields.

B. Non-Native Substrates

The prior discussion has given some overview of the natural structure of GaN and the way it alters its behavior based on strain. Lattice mismatch, the difference in lattice constant between an epi-film and the preceding layer, can cause strain that results in piezoelectric fields as well as cause dislocations to relax this strain. Thermal coefficient mismatch (the difference in thermal expansion coefficients (TECs) between GaN and substrate) can also induce strain. Due to the lack of a bulk GaN substrate, much work has been done to engineer the strain developed in these heteroepitaxial structures. The most common non-native substrates include single crystals of sapphire (aluminum oxide or Al_2O_3), silicon carbide (SiC), gallium arsenide (GaAs), or silicon (Si).[27] Each substrate material will be discussed in further sections below, but each of these materials has a plane in which hexagonal symmetry can be found. Sapphire

has hexagonal symmetry in the (0001) plane, SiC in the 6H polymorph has it in the (0001) plane or in the 3C polymorph it has it in the (111) plane, GaAs in the (111) plane, and Si has hexagonal symmetry in the (111) plane. Other materials include Ti metal, TiN, and HfN.[28–31] However, only sapphire, SiC, GaAs, and Si have been used to an appreciable extent.

Sapphire

The crystal structure of sapphire with an emphasis on the hexagonal (0001) plane is shown in Figure 3. Sapphire single crystals are grown using the Czochralski method, where a small seed crystal is dipped into a melt and slowly withdrawn. The melt pulls up with the seed via surface tension and cools, solidifying and continuing the crystal.

Although the corundum and wurtzite crystal structures are different, the shared symmetry has allowed high quality growth of GaN on sapphire to occur. The lattice constants of sapphire are 4.76 Å in the a-direction and 12.99 Å in the c-direction.[32] It is important to note that this is dramatically different from GaN, which has 3.189 Å in the a-direction and 5.185 Å in the c-direction.[33] As a result, the equivalent directions between GaN and sapphire (for example, [1000]) would be rotated 30° with respect to each other. This serves to reduce the lattice mismatch, making epitaxy possible.[27] The TEC for GaN is ~4 ppm/°C while the TEC for sapphire is ~5 ppm/°C.[27,34] This leads to a rather high compressive stress in the GaN when

cooling.[35]

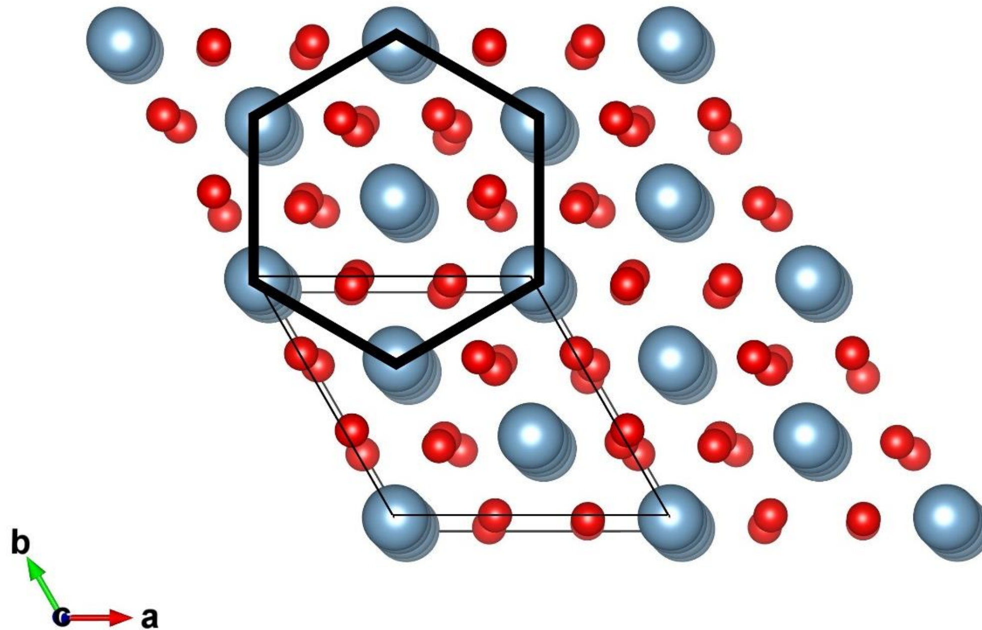

Figure 3. C-plane view of the sapphire (Al_2O_3) unit cell. The black hexagon is drawn in to demonstrate the hexagonal symmetry of the c-plane.

Epitaxial growth of GaN on sapphire is still making progress toward more advanced techniques. Within the last few years, GaN on patterned sapphire has become of interest as it improves the crystal quality while remaining less costly than some other alternatives.[36,37] However, other techniques such as epitaxial lateral overgrowth (ELOG) and pendeoepitaxy (PE) are also of interest as they can dramatically reduce the dislocation density in small regions. Epitaxial lateral overgrowth achieves this by first depositing a highly defective GaN buffer layer and then masking portions of the substrate with a material such as SiO_2 before a regrowth. The mask prevents nucleation of GaN while in the open regions the GaN will grow out, eventually also growing laterally over the mask. This lateral overgrowth does not propagate the threading dislocations (TDs) that originate at the heterojunction and thus it has

a much lower dislocation density. The final result is a substrate with regions of very high dislocation density (where the GaN grew up through the mask) with regions of low dislocation density (where the GaN grew laterally over the mask).[37–43] However, sometimes a buffer layer is not used.[42] PE is a method similar to ELOG but lacks a mask. Instead, the buffer layer of GaN is etched to create open regions between stripes of GaN. The lack of any substrate or mask in the open regions allows the GaN grown laterally to have very low dislocation density, similar to the effect found in ELOG.[40,44] The low defect regions may have dislocation densities several orders of magnitude lower than the high defect regions, enabling sensitive devices such as lasers to be fabricated in the low defect regions.[9,14,42] Many LEDs have been grown on sapphire substrates even without the use of ELOG or PE with good results.[6,23,45]

Silicon Carbide (SiC)

SiC is another wide bandgap semiconductor similar to GaN. It has a bandgap of ~3 eV (although this will depend upon the polytype). The bandgap is indirect (meaning the electron states with a minimum energy difference in the conduction and valence bands have different momenta), which reduces radiative efficiency. This precludes SiC acting as an optoelectronic material, but it can still function in an electronic device or act as a substrate.[46,47] The stable crystal structure of SiC is somewhat less well defined than that for most systems. A polytype defines a particular crystal structure by indicating the number of layers that exist in a unit cell. The polytypes have very little energy difference and thus many different polytypes can exist at room temperature. A few of the more common types include 4H-SiC (4 layers of Si atoms per unit cell), 6H-SiC (6 layers of Si atoms per unit cell, shown in Figure 4), and 3C-SiC. The H and C indicate the type of symmetry, H meaning hexagonal and C meaning cubic. To put this in perspective with GaN, 3C-SiC has the zinc blende structure of the cubic form of GaN

with Si replacing Ga and C replacing N. The above mentioned 4H-SiC and 6H-SiC are mixed forms of wurtzite and cubic. It is important to note here the similarity between the wurtzite and zinc blende crystal structures, as the difference is a simple stacking sequence difference. Moving in the c-direction, there are two different possible stacking sequences for layers of Ga that can occur. They are usually referred to as ABCABC (zinc blende) or ABAB (wurtzite).[48] Figure 5 depicts the three possible layers (a green layer, or A, a blue layer, or B, and a magenta layer, or C). The wurtzite unit cell only has A and B, or the green and blue, while the zinc blende has A, B, and then C. It is then obvious how 3C-SiC has the 3 in it, the three refers to the A, B, and C layers. Taking this to the extreme, 2H-SiC has the wurtzite crystal structure. The lattice constant of 6H-SiC is 3.081 Å, making the lattice mismatch to GaN rather small.[49]

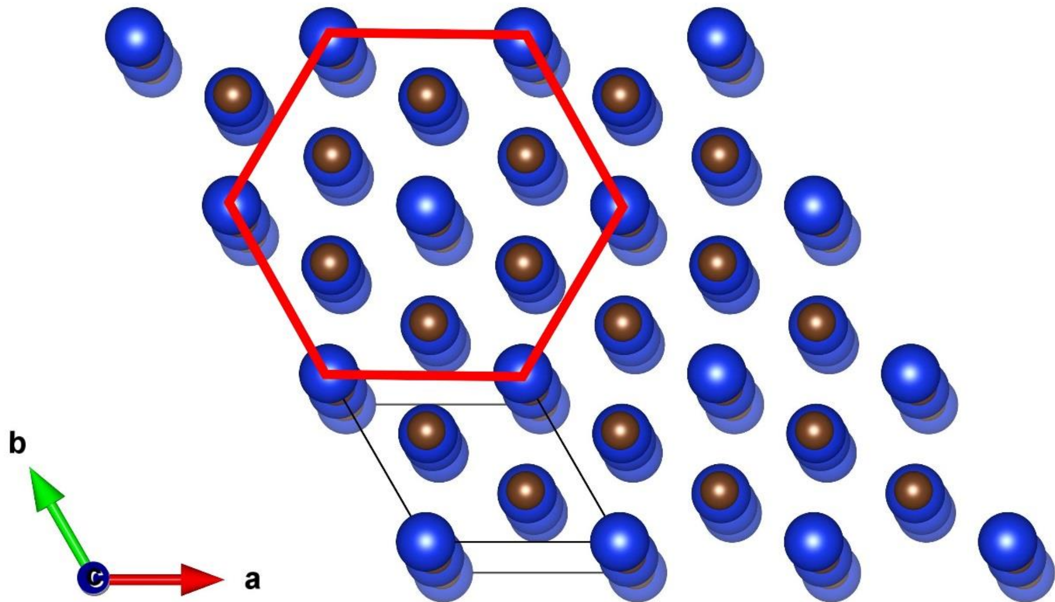

Figure 4. C-plane view of the SiC unit cell. The image shown is of the 6H-SiC polytype. Again, the red hexagon is to illustrate the hexagonal symmetry of the plane.

In spite of the relatively small lattice mismatch, some strain engineering is typically used in GaN on SiC growth. This usually comes in the form of ELOG for LDs.[46,50] More fundamental studies of growth have demonstrated very high quality ELOG films using PE or ELOG with defect densities as low as 10^4 cm^{-2}, down from 10^8-10^{10} cm^{-2}.[51,52] Edmond et al. attempted growth of a laser without any sort of defect reduction but found the device failed to lase.[46] This illustrates that even with a relatively small lattice mismatch, defect densities can dramatically degrade the performance of high power density devices.

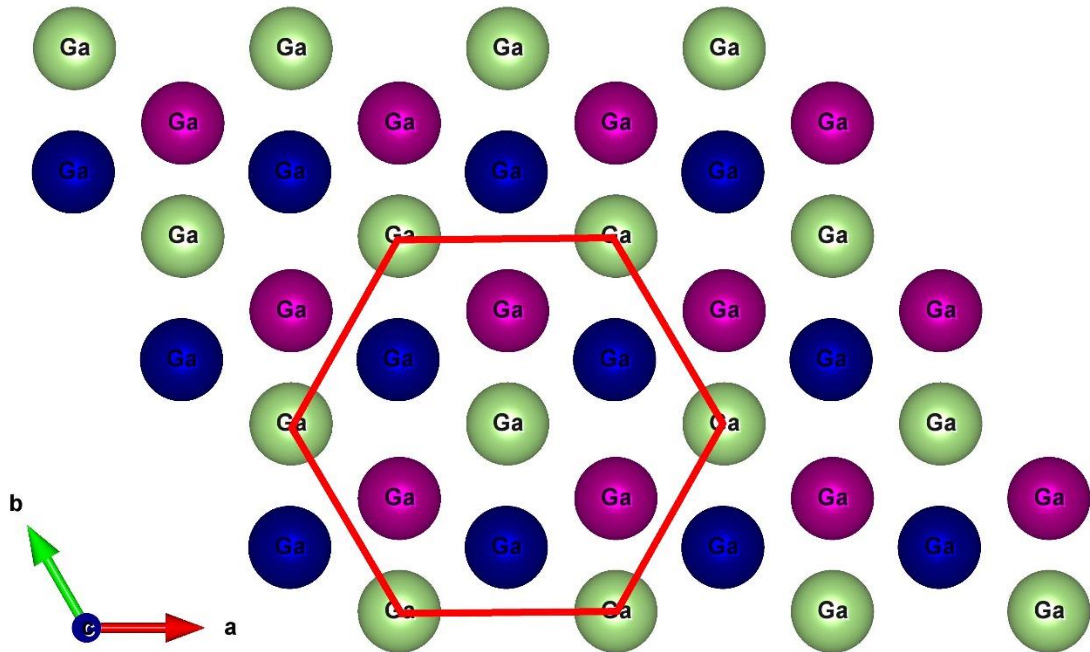

Figure 5. C-plane view of GaN in either the wurtzite or zinc blend form with N removed. Wurtzite GaN has only the green and blue Ga atoms, whereas the stacking sequence for the zinc blende GaN is green, blue, magenta, and then back to green.

Gallium Arsenide (GaAs)

GaAs is another group III-V compound semiconductor, similar to GaN. However, it has been in use for a while longer and it is thus a more mature technology. The growth method of

GaAs is liquid-encapsulated Czochralski, similar to the Czochralski method mention above where a seed is dipped into a melt of GaAs. As the surface tension holds the melt and seed in contact, the melt nearest the seed cools and solidifies, continuing the GaAs crystal. The liquid-encapsulation concept comes from a liquid boron oxide (B_2O_3) that covers the melt surface as well as the seed. The encapsulant serves to prevent decomposition of GaAs. The pressure required to prevent GaAs from decomposing into As gas and Ga metal is 2.2 bar at the melting point.[53] The GaAs crystal has cubic symmetry with the zinc blende structure (the same as metastable GaN). However, the lattice constant is largely mismatched with the effective "a" lattice constant (the distance between Ga in the GaAs surface) being 4.0 Å (calculated by $a_{hex} = a_{cubic}/\sqrt{2}$) compared to GaN at 3.189 Å.[27] The unit cell of GaAs is shown in Figure 6. In spite of the large lattice mismatch, GaN can be grown on GaAs (111) as long as either the growth temperature is kept relatively low (below 850°C) or a low temperature GaN is grown at or below 850°C before device growth occurs.[27] ELOG of GaN on GaAs has also been reported for both wurtzite as well as zinc blende GaN.[54,55] However, it is also common for research on zinc blende GaN to use GaAs substrates.[19,54,55]

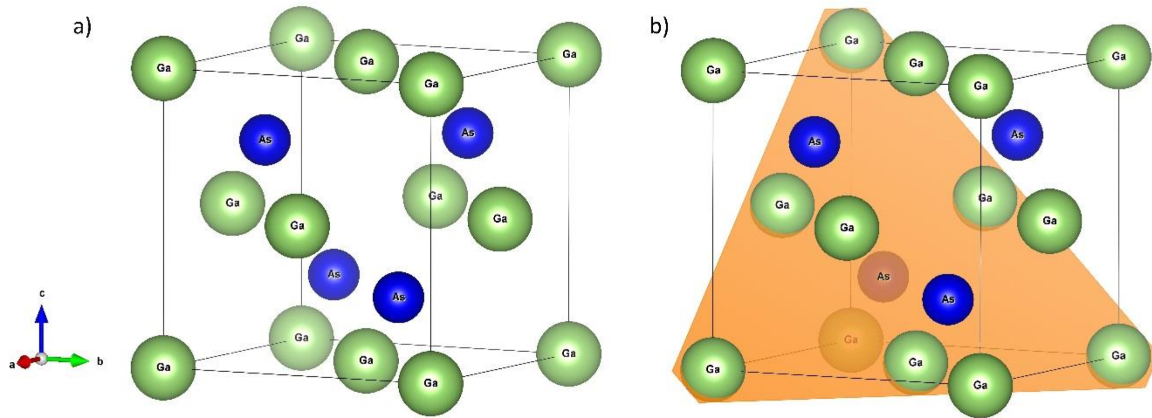

Figure 6. The unit cell of zinc blende GaAs a) without the (111) plane and b) with the (111) plane (shown in gold).

Silicon

Silicon (Si) may be the most mature semiconductor material. Similar to other substrates discussed, Si is grown via the Czochralski method. Boules as large as 300 mm in diameter and weighing as much as 300 kg can be drawn.[56] It has been demonstrated as well that these boules are nearly perfect, lacking any microdefects such as dislocation loops.[57] Silicon has the diamond crystal structure, similar to the zinc blende crystal structure except all atoms are Si. Thus, we again have a (111) plane that has the required symmetry to match c-plane GaN. The a lattice constant of Si is 5.431 Å, leading to an effective "a" lattice constant of 3.84 Å.[27] Similar to the case of GaAs, this leads to significant strain in the grown GaN. Unfortunately, the TEC of Si is also smaller than GaN, so as the epi-film and substrate cool from growth temperature to room temperature, the tensile stress on the GaN increases.[27,34] However, patterning of the Si, ELOG, and PE are all avenues to allow GaN devices to be grown on Si.[27,58,59] Buffer layers involving SiN_x, AlN, and GaN have also been used to develop GaN

with sufficient quality for LEDs, micromechanical resonators, filters, as well as high quality high electron mobility transistors (HEMTs).[25,60–62] Armitage et al. also demonstrated GaN on Si using a HfN buffer layer in both Si (001) and Si (111).[63] Carburizing of the surface has also been used, as it has been noted above SiC has a closer lattice constant.[64,65] Zinc blende GaN has also been grown on (001) Si, although this is a less common use.[19,64] Si substrates are notoriously cheap due to the size and maturity of the industry, making use of Si substrates attractive.

C. Hydride Vapor Phase Epitaxy (HVPE) of GaN

HVPE has become a main workhorse of GaN production for pseudo-bulk substrates of GaN.[66] The substrates are not truly bulk, as they are still seeded on non-native substrates. This heteroepitaxy leads to an initial stress that eventually cracks the grown material, creating a limitation of how large the crystal can be. However, boules several millimeters thick are available and can be sliced to yield non-polar and semi-polar GaN.[67,68] If this were a true bulk process, the growth should be able to continue until the growth equipment itself is the limiting factor.

HVPE, as its name suggests, is a vapor growth method. Carrier gases include N_2 and H_2 while reactive gases include NH_3 and a Cl source such as HCl or Cl_2. Although the details of optimization can become rather involved, the process itself is relatively simple. A source of Ga, often a container of molten Ga metal, is heated and hot HCl gas is flowed over it. The HCl gas reacts with the Ga, forming volatile GaCl or $GaCl_3$. The GaCl is channeled into a growth chamber where a substrate that is heated with a susceptor sits. A separate channel brings NH_3 into the growth chamber and the NH_3 and GaCl reactor to form GaN on the substrate. A schematic of an HVPE reactor is shown in Figure 7. Parasitic deposition is also

common, causing growth of GaN in areas other than the substrate.[69] There is also excess NH_3 and HCl that pass out of the growth chamber and into exhaust. This results in a buildup of solid NH_4Cl as the gases cool enough to react and solidify.[70] The use of these boules as substrates for devices requires the removal of the substrate and with the thickness being several millimeters, non-polar and semi-polar oriented GaN can be sliced from the boule. Non-polar GaN has a normal orthogonal to the c-direction, so its width (at least on one side) is limited to the thickness of the boule. Similarly, semi-polar GaN is limited to $\frac{t}{cos\theta}$ where t is the thickness of the GaN boule and θ is the angle between the c-direction and the normal of the surface. Thus, at the moment there exists no straightforward method for large non-polar or semi-polar substrates.

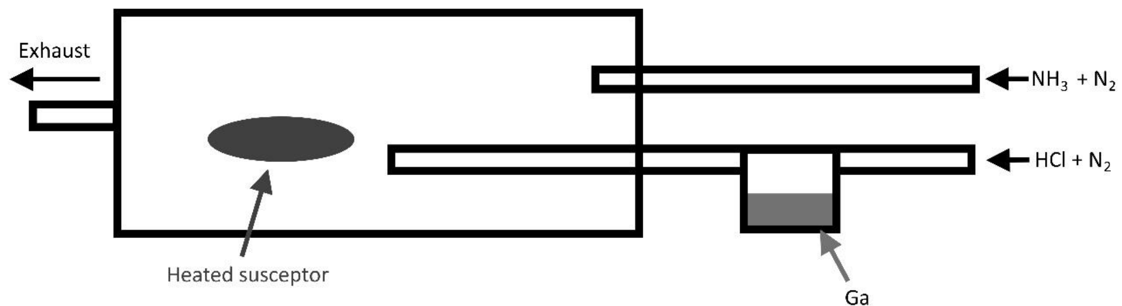

Figure 7. Schematic of an HVPE reactor. The growth chamber is made of a high temperature ceramic, often quartz.

The quality of the HVPE grown material is limited by the fact that is still is initiated on a foreign substrate, but the material quality is still rather high. Similar to MOCVD, foreign substrates for HVPE GaN include GaAs and sapphire. Material with threading dislocation densities (TDDs) as low as 10^6 cm^{-2} have been reported.[69,70] The high quality material is grown either by reducing dislocations using ELOG, which will allow regions of high TDD to exist,

or by growing thick material. Growing thick material allows bending of the dislocations which tend to cease propagating upwards with the growth interface.[71] The interface between the sapphire and GaN still initially has TDDs as high as 10^8-10^9 cm^{-2}, similar to MOCVD mentioned previously.[72,73] Sumitomo Electric developed a method very similar to ELOG which they referred to as dislocation elimination by the epitaxial-growth with inverse-pyramidal pits (DEEP), where dislocations are concentrated in a specific region. Like ELOG, a SiO_2 mask is placed on the substrate with small openings in the mask where the GaN can grow through and then coalesce. Around these mask openings, faceting occurs and the faceting of the GaN forms "V-pits", inverse hexagonal or inverse dodecahedral pyramids. The dislocations tend to cluster around the V-pits, leaving high quality material in-between. TDDs were estimated to be as low as 2×10^5 cm^{-2}.[72]

For the use of HVPE grown GaN as device substrates, the non-native substrate must also be removed. Sumitomo Electric simply mechanically polished away the GaAs substrate.[72] Void-assisted separation (VAS) has also been used. The process starts by growing a GaN template several hundred nanometers thick and then depositing a thin layer of Ti metal. The GaN and Ti are then annealed in N_2 and NH_3 at high temperature, causing the Ti layer to nitride and form a porous network instead of a continuous film. The H_2 that forms from decomposing NH_3 also etches the GaN in the regions not covered by the TiN layer. GaN is then grown on top of the TiN. Although some of the void areas through the TiN have GaN grow up through them, not all do. These voids are eventually overgrown by lateral growth of nearby GaN islands. The high temperature growth of the GaN and lack of N_2 in the void can also cause some decomposition of the GaN, leading to voids above the TiN template as well as below. Eventually, the islands coalesce into a thick film with a weakly bonded interface to

the initial substrate. Removal of the substrate can be achieved by separation with a knife and is assisted by the thermal stress induced by the difference in TEC between the substrate and the GaN. GaN boules as large as 3.2 inches in diameter have been made with this method. Dislocation densities are reduced to ~10^6 cm^{-2} via dislocation bending through GaN island facets and void filling.[71] Laser-assisted separation has also been used, where a laser rapidly heats the GaN/substrate interface causing delamination.[74] Unfortunately, laser-assisted separation did not appear to be reproducible enough for industry.[66]

D. The Sodium (Na) Flux Method

The Na flux method of GaN growth was pioneered by Yamane et al. in 1997, although Na flux had been used for other nitrides prior to this.[75] The method is a solvent based method where molten Na metal is the solvent and Ga and N are the solutes. The method is rather straightforward: Ga and a Na source are mixed together and heated in a N_2 gas environment. As long as the N_2 gas pressure is greater than the equilibrium N_2 pressure over GaN at the growth temperature, GaN growth will proceed. It is important here to note that this implies the chemical driving force for growth of GaN is controlled by the N_2 pressure, as the system is generally almost isothermal. This is in contrast to other solvothermal methods such as the ammonothermal method (see Chapter 1, section E: The Ammonothermal Method), where the system is transporting material and the chemical driving force is determined by the temperature difference. Early work used NaN_3 as the sodium source and as a source of N, but Na metal can also be used.[75–77] The N_2 pressures are rather mild, around 5 MPa, while temperatures range from 700°C to 1000°C.[78] There are some hazards in the process, however. Na is chemically reactive with almost any O containing species including air and water. The reaction rate is relatively slow for large chunks, as the surface simply oxidizes, but Na metal

is pyrophoric in nature. Thus, ethanol and isopropyl alcohol have been used to react with the Na more controllably.[75,76,79] This method does pose some risk as well; if the Na should somehow get hot enough (for example, if it was accidentally exposed to water), then an alcohol fire could ensue. However, the violent reaction with water precludes the oxidation of the Na without some sort of mediator. Recent work by Lakshmanan et al. has found that the use of Epsom salt solutions ($Mg(SO_4)_2 \cdot 7H_2O$) are highly effective in rapidly and safely dissolving Na in the correct concentrations (1.4-2.4 M). Higher concentrations led to slower dissolution and sometimes incomplete dissolution of the Na while less concentrated solutions led to violent reactions.[80]

While the reactivity of Na metal is an inherent danger that must be mitigated, the low pressures and moderate temperatures make this process for bulk GaN rather appealing. Stainless steel shells can be used as pressure vessels and the gas handling equipment doesn't need to be highly corrosion resistant as long as it is not in contact with the growth environment at temperature, which would expose it to Na vapor. Stainless steel (in particular, 316 stainless steel) has been used by the pioneers of the Na flux method for GaN, making the material for reactor construction relatively cheap.[75,81–83]

The Na flux method has also shown great signs of success in the ability to grow high quality GaN in terms of both purity and crystal quality. Early growths indicated feasibility with polycrystalline growth. The method was actually used to grow ternary nitrides such as Ba_2ZnN_2, Sr_2ZnN_2, $Ba_3Ga_2N_4$, $Ba_5Si_2N_6$, and Ba_3GeN_2 before the growth of GaN was developed.[75] Seeded growth proceeded shortly thereafter on an AlN template growth on sapphire. Interestingly, other substrates such as Si (111), sapphire, and SiC were also tested in the flux but only AlN yielded seeded GaN growth. The authors suggested (although they

did not prove) that the AlN template served to reduce the surface energy for GaN nucleation, again indicating the importance of the substrate for GaN growth.[81] The bare stainless steel appeared to react with the Na-Ga mixture, thus crucibles of boron nitride (BN) were tested. No significant reaction was found while columnar GaN was found to nucleate on the walls.[76] The change in growth habit from changing the Na/Ga ratio indicates that a significant change in chemical driving force may be taking place. With growths at 750°C, Yamane et al. found that the GaN growth habit changed from granules at very high Na concentrations to platelets at intermediate concentrations to GaN prisms at small concentrations. The change is likely due to a change in the chemical driving force for growth (or free energy change) which indicates that increasing the Na concentration increases this driving force when going from moderate to high Na concentration.[79] As early as 2001, Aoki et al reported growing clear GaN needles.[84] That same year, Aoki et al. also reported growing 5 mm by 3mm platelets using a shaped crucible (the 5 mm and 3 mm were the largest dimensions).[85] The role of nucleation and growth has been investigated to some extent in early studies attempting to use low supersaturation to nucleate and then increasing the chemical driving force for growth after. This was achieved by increasing the N_2 pressure during the growth period, which resulted in larger GaN crystals. In the same study, the authors found that the addition of a small amount of NH_3 to the growth environment increased the growth rate.[86] The thermodynamics of nitrogen solubility in Na-Ga melts is not yet well understood, however. Aoki et al. performed a study to determine GaN dissolution into Na at multiple temperatures and N_2 pressures, but no direct measurement of nitrogen in the melt was made. The ion-coupled plasma (ICP) method was used to determine the Ga dissolved in the melt, which yielded 0.5 mol%. Aoki et al. assumed that some 0.25 mol% of N stayed in solution, but no direct measurement was

made.[87] The dissolution of the Ga could have been solely due to the formation of the Ga dissolved species with no increase in N dissolved. The very small amount of GaN decomposition would lead to very small changes in pressure which may have not been detected. If their assumption is correct, however, then the solubility of N in Ga-Na fluxes is orders of magnitude higher than in either pure Na or pure Ga. The Na flux method actually can dramatically benefit from the addition of small amounts of other elements. The addition of Li, for example, increases the yield of GaN and allows a lower N_2 pressure to be used while increasing the Li content changes the crystal habit to flat platelets instead of hexagonal prisms.[88–90] However, Li does incorporate in the crystal, which can be detrimental to electronic devices grown on a Li contaminated substrate.[88,91] The addition of Ca also helps increase the transparency in the Na flux, as crystals grown in pure Na tended to be black.[92–95] The addition of C in the form of graphite has also been shown to decrease polycrystalline GaN (polyGaN) nucleation on the walls and flux surface. It was also found that the C did not significantly incorporate, thus proving itself as a very valuable additive.[83,96,97] Suppression of polyGaN is necessary due to the high pressures of N_2 gas used. The higher N_2 pressures are used to increase growth rate and the carbon additive allows higher growth rate without sacrificing Ga to polyGaN. With the addition of C and Ca, high quality crystals as large as 2 inches in diameter and several millimeters thick have been grown.[83] The crystal quality has also been shown to have dislocation densities as low as 2.3×10^5 cm^{-2}.[98] Attempts were made to grow on 4 inch Si (111), but the strain in the growth caused cracking.[97] An apparatus was also developed to increase the growth rate by allowing mechanical mixing of the flux by swinging the entire reactor system.[95]

The thermodynamics of the Na flux method are still unclear. As mentioned above, it is known that the addition of different elements can change the crystal growth habit in ways similar to the way in which changing the temperature and N_2 pressure modify the growth habit. High chemical driving force (given by lower temperature or high N_2 pressure) tend to favor very small GaN granules with moderate driving force leading to platelets with large c-plane surfaces and small driving forces leading to hexagonal prisms.[84,99] Similarly, the Na concentration also affects the morphology with similar morphology changes. High ratios of Na/(Na+Ga) led to GaN granules, intermediate values led to GaN platelets, while low ratios led to prisms at 750°C.[79] Interestingly, this is trend appears to be somewhat reversed when C is added. Mori et al. report more platelet like growth at lower Ga (or higher Na) along with increased growth rate.[96,97] The addition of small amounts of C (0.5 mol%) increased the growth rate while higher concentrations (1-3 mol%) decreased growth rate, although it was still higher than no C, and >3 mol% C almost completely suppressed growth at 860°C.[96] It is speculated that the C exists as the cyanide ion (CN^-) due to the low solubility of C in Na-Ga.[83] The charged ion may interact with the polar faces of a GaN crystal including c-plane as well as semipolar faces. This charged ion interaction may change the surface energy rather than the chemical driving force, as the addition of C reduces polyGaN nucleation. However, the shift of prism or pyramidal GaN to platelet GaN indicates an increase in chemical driving force (in the absence of any surfactants or surface modifiers). An explanation of the effect of C on morphology could then be that C changes the surface energy of the GaN, lowering the c-plane surface energy relative to the non-polar planes.

E. The Ammonothermal Method

The ammonothermal method of GaN growth is another method that uses a solvent. However, in the ammonothermal method supercritical ammonia is used as a solvent and different chemical species called mineralizers are added to increase the solubility of GaN in solution. Supercritical fluids are in a temperature and pressure regime where there are no distinct vapor and liquid phases. Compression of the heated fluid will only result in a higher pressure but no liquid will condense. Supercritical fluids have significant dissolving power but also have very low viscosity, making them useful in transporting material in a dissolved state. A typical ammonothermal system will have two temperature zones, one for dissolving source material and one for growth of the seed crystal. One or more baffles will separate the two temperature zones such that convection is disrupted, allowing better defined temperatures in the zones. The baffles, source, and seed will be held up by some internal structure, here referred to as the furniture. Although internal heating may be possible, external heaters are often used because of the high pressures involved. Figure 8 shows a schematic of such a reactor used at UCSB with Na mineralizer.

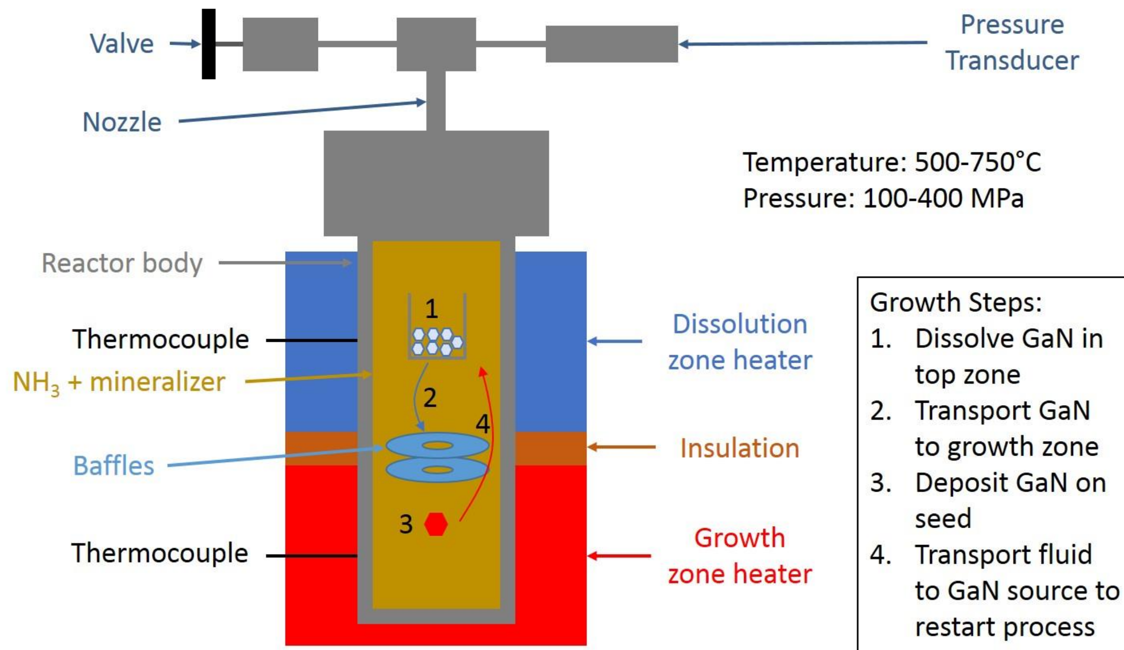

Figure 8. Schematic of a basic ammonothermal reactor used at UCSB.

Typical pressures for the basic mineralizers are >200 MPa while acidic systems tend to be lower in pressure, between 80 and 150 MPa. The ammonothermal method uses either basic mineralizers such as Na or K or acidic mineralizers such as Cl and F. The mineralizer types are named basic or acidic because of the manner in which they interact with NH_3. Basic mineralizers tend to form NH_2^- ions, akin to bases forming OH^- in aqueous solutions. Similarly, acidic mineralizers form NH_4^+ ions, akin to the H_3O^+ (usually described as H^+) ions formed in aqueous solutions. It has not been directly verified that these ions do form at the temperatures of ammonothermal growth, but each the mineralizer classes act somewhat differently regardless.

Basic Ammonothermal Growth

Basic ammonothermal growth uses alkali metals, but even within the basic regime the type of mineralizers used can alter many important parameters of the growth environment. For

example, Dwiliński et al. found that $LiNH_2$ gave rise to GaN particles with photolumenscence shifted towards higher energy compared to KNH_2 when synthesizing GaN from Ga metal.[101] Retrograde solubility is the behavior when an increase in temperature results in a decrease in solubility, whereas normal solubility is the behavior when an increase in temperature results in an increase in solubility. Although basic mineralizers exhibit this behavior in the growth regime, it should be noted that at lower temperatures the solubility of GaN may be normal. Thus, a peak solubility occurs with normal solubility at temperatures below the peak and retrograde solubility above the peak. Figure 9 shows a plot of the measured solubility of GaN in the basic system with Na and K as mineralizers. It is important to note, however, that more recent studies have shown that Ga can leach into the reactor body, thus rendering these solubility plots incorrect. The principle of retrograde solubility is illustrated though and the plot of NH_4Cl shows only normal solubility. In theory, retrograde solubility can be a helpful phenomenon. In the case of retrograde solubility the growth occurs at the highest temperature the system experiences. If the temperature is limited by the reactor then the retrograde system will be able to have growth occurring at the highest temperature where diffusion is faster and thus defects are less likely to be generated (all other things being the same).

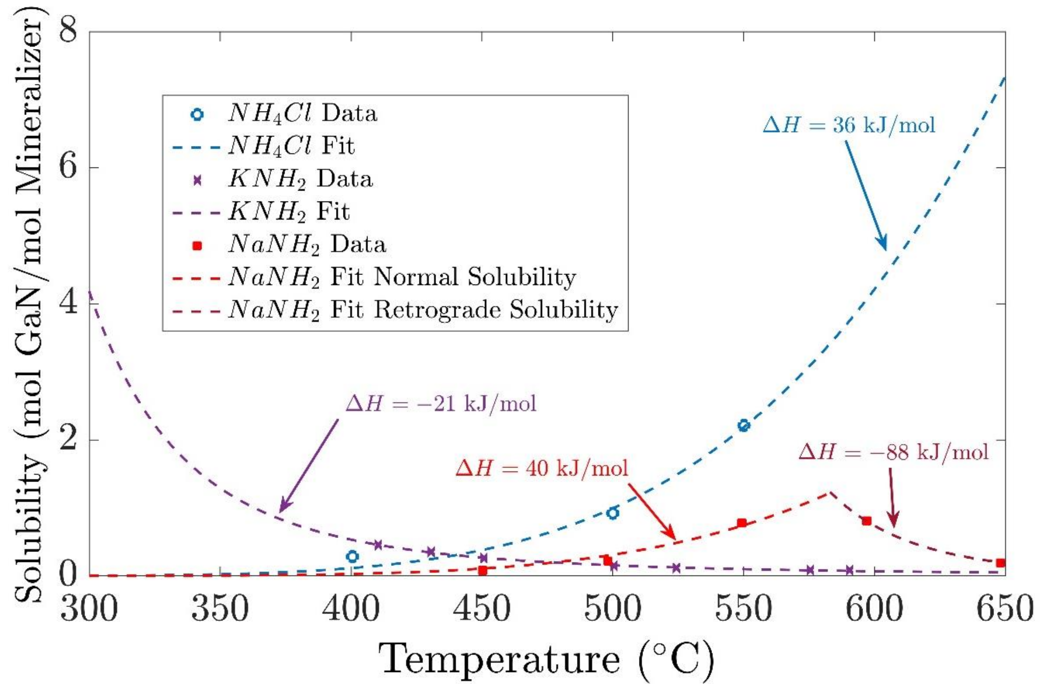

Figure 9. Solubility vs temperature for ammonothermal systems with Na, K, or Cl mineralizers. Data is from ref. [102].

Early reports of ammonothermal GaN growth go back as far as Dwiliński et al.'s report on growth of GaN powder in 1995.[103] Although the crystallites were small, they had very low strain. These crystallites also exhibited yellow coloration, a trait that will be seen in growth in the decades to come as well.[104,105] Early work also used Li as a mineralizer which has the advantage of lowering the reaction temperature quite significantly (300°C vs closer to 500°C).[103,106] Crystallites that were obtained with Li mineralizer at lower temperature (300°C) also had the yellow coloration but increasing the temperature to 400-500°C yielded white powder.[106] The possibility of growing small crystallites implies that growth of larger crystals is possible, but it also creates the possibility of self-nucleated seed crystals, which will probably be of much higher crystal quality than seeds grown from non-native substrates. Mixing of mineralizers is also possible and usually a "neutral" mineralizer that does not

change the balance of NH_4^+ or NH_2^-, such as NaI or KI, will be mixed with either a basic or acidic mineralizer.[107–110] This was more common in earlier research but appears to have fallen from favor.

While small crystallites dominated early research, the end goal of any bulk crystal growth technique is large crystals with perfect quality. Seeded growth has thus become common, often using HVPE grown seeds. A major issue that has been very common is the incorporation of impurities, especially O, into the crystal. An early report by Callahan et al. gave O concentrations as high as 10^{20} cm^{-3} for N-face GaN and high 10^{19} cm^{-3} for Ga-face GaN grown in the c-direction. This can be contrasted with the actual atom density of GaN, which is around 9×10^{22} cm^{-3}. However, Fe, Ni, and C also contaminated the crystal in high concentrations (10^{19}-10^{20} cm^{-3}).[111] The use of a silver capsule has been found to mitigate the incorporation of transition metals that may come from the reactor walls, but O and Na (the mineralizer used) are still present in concentrations of around 10^{18} cm^{-3}.[100] Thus, the search for ultrahigh purity GaN crystals is still underway. However, different impurities lead to different negative effects and sometimes these effects don’t matter. Transition metals, such as Ni and Fe, as well as C cause significant coloration of the crystal. These impurity atoms often act as optical absorbers but can also be electrically active. For example, Fe and C both act as deep acceptors which may be useful in the growth of semi-insulating GaN.[112] Alternatively, power electronics have no requirements for optical properties but a conductive substrate might be useful so high O concentrations (which would increase broadband optical absorption) would not only be tolerable but may be desirable. Such optical absorption would not be tolerable in a device such as an LED. Another common optical feature of ammonothermal GaN is yellow coloration.[106,113,114] It is suspected that one source of the coloration is Ga-vacancies (V_{Ga}). V_{Ga}

tend to be stabilized by hydrogen and can form a V_{Ga}-hydrogen complex with one or more hydrogen atoms present (hydrogenated V_{Ga} or V_{Ga}-H) with different absorption peaks for the different H occupancies.[105] V_{Ga}-oxygen complexes may also give rise to the yellowish color. Adekore et al. doped ammonothermal GaN with Er and a significant amount of erbium oxynitride was found in the reactor afterwards. The doping of Er was also found to reduce the yellow coloration, possibly relating V_{Ga}-O complexes to yellowish coloration as well. It cannot be ruled out that both V_{Ga}-H and V_{Ga}-O give rise to the yellow coloration.

The question of the feedstock of GaN in any system is of interest for multiple reasons including the chemical driving force as well as impurities. The main contaminant for Ga sources is usually O, possibly in the form of water or O_2 gas. GaN grown from polyGaN with high O concentrations is unlikely to have an O concentration lower than the feedstock. Although a few metals were tried, it has been found that many oxides are not stable in the presence of Na mineralizer.[115] If the oxide is not stable then one would expect the parent metal would fail to act as an O getter. Thus, a clean source of Ga or GaN is required for high purity. PolyGaN is a very common GaN source, but because the solvent contains ample N the source only needs to have Ga that is accessible. For example, Ga metal has also been used as a Ga source.[106,116] Wang and Callahan also used Ga-containing intermediates such as $NaGa(NH_2)_4$.[116] It is interesting to note that the use of these different Ga sources will alter the Ga chemical potential, thus changing the chemical driving force for growth. This has the potential to change growth rate as well as growth morphology but it has not been significantly studied. Tuning the chemical potential by altering the Ga source will also add another layer of complexity in controlling the system. Perhaps as ammonothermal growth becomes better understood, the use of alternative sources of Ga will become a significant research topic.

The pressure of the system also is indicative of the N chemical potential, which very well may alter GaN growth. The pressure is usually dictated by the amount of NH_3 and the temperature profile of the reactor, although potentially other gases could be added. The free energy of the NH_3, H_2, and N_2 will determine the chemical potential of N in the gas phase. As the GaN free energy is largely pressure independent, the chemical potential of N in GaN will be also largely pressure independent. Thus, the change in N chemical potential will directly affect change in free energy of the formation of GaN from the intermediates. Equivalently, we can write: $\Delta G_{GaN} = \Delta G_{Ga} + \Delta G_N$, where ΔG_{Ga} and ΔG_N are the changes in the Ga chemical potential and N chemical potential, respectively. It has been observed that NH_3 decomposes at ammonothermal growth temperatures, leading to a pressure increase. Further loss of H_2 gas via diffusion through the reactor walls continues to drive decomposition via Le Châtelier's principle.[100] This leads us to the inevitable conclusion that the driving force for growth is not constant for long-term growth.

Average growth rate is another important metric for bulk crystal growth, as the economics of the industry requires low cost for the method to be viable. Initial growth rates were respectable, on the order of ~100 μm/day.[114,117] Significant improvements have been made on this with the addition of a Ag liner leading to growth rates as high as 344 μm/day.[100] These growth rates are on the (0001) planes (a sum of growth on the (0001) and $(000\bar{1})$ surfaces). Growth rates on the non-polar planes are usually lower, closer to 50 μm/day.[100]

High crystal quality is also of great importance. Perfect crystal quality may be the most important argument for the requirement of a truly bulk growth technique. The ammonothermal technique has shown exceptional crystal quality. Often, seed quality is replicated or somewhat improved upon as dislocations grow together. Pimputkar et al. showed replication of crystal

quality in the Ag liner system.[100] The ideal is to self-nucleate a seed that will have no defects and grow it to large scales. Such a seed would have properties similar to those published by the Ammono Company. The Darwin width is the smallest peak width that is attainable given the structure of the crystal and the particular reflection that one is observing. The material grown by the Ammono Company has XRD FWHMs of around 10 arcseconds for the (0002) peak, essentially the Darwin width.[118] This implies that the crystal quality is not necessarily limited by the technique, rather the growth is only as good as the seed from which it starts. However, this applies more to seeds that are already of high quality, as some improvement can be made from seeds that have higher defect densities by dislocation bending.[119] Dwilinski et al. measured etch-pit densities (a measure the of TDD by pit formation at the TDs) as low as 5×10^{3} cm^{-2}. They measured no dark spots in CL (TDs also are suspected to act as non-radiative recombination sites and thus would produce dark spots in CL).[118] However, Meissner et al. showed that high Fe concentrations (or possibly other deep level acceptors) could create significant error in CL dark spot measurements.[120] Regardless, exceptional crystal quality has been demonstrated with basic ammonothermal growth.

Acidic Ammonothermal Growth

Acidic ammonothermal growth employs halide compounds (such as NH_4Cl or HCl) to form a higher concentration of NH_4^+ ions. Presumably, the ion concentration is higher but direct measurements of ion concentration do not appear to be available in literature. The most explored of the halides is Cl^-, but I^- has also been significantly explored. F^- has become a major topic of interest as Bao et al. published impressive m-plane growth rates using NH_4F mineralizer, with growth rates as high as ~300 μm/day.[121] The effect of mineralizer type is more profound in the acidic system. Ehrentraut et al. crystallized GaN out of solution and

found significant variation in the phase of GaN (zinc blende vs wurtzite) depending on whether Cl^-, Br^-, or I^- was present. I^- gave rise to essentially pure zinc blende GaN at the temperatures probed whereas Cl^- only gave a small amount at very low temperature and yielded pure wurtzite GaN at higher temperatures.[122] Similarly, the addition of LiCl at low temperature to a NH_4Cl mineralizer lead to significant changes in mass transport.[123]

Solubility with acidic mineralizers has been researched more than with basic mineralizers, but a consensus does not appear to have been reached. Again, Cl^- has been investigated the most and that is the mineralizer that has had the largest spread in data. Regardless of the mineralizer, the solubility has been normal in all cases below 600°C.[124–127] Unfortunately, this is limited to temperatures of about 550°C and growth data from Yoshida et al. (as well as data that will be discussed in Chapter 3, section C of this thesis) indicates that this trend does not continue much past 600°C. Yoshida et al. grew in a retrograde solubility regime using NH_4Cl with a growth temperature of 700-720°C and a dissolution temperature of 650-700°C.[128] It does not appear that there is any high temperature data for any acidic mineralizer available at the moment. Even the Cl^- data that is available strongly conflicts. At a temperature of 550°, ratios of GaN/NH_4Cl are 0.44, 2.2, or 0.051 depending on the data source.[124,126,127] This spread in data may come from contamination, as the spring in Schimmel et al.'s work wasn't mention being coated and Tomida's entire reactor was uncoated.[126,127] As both of those components are Ni alloys, corrosion of the components could poison the environment and alter the measured solubility.[115,129,130] Without reference data of a clean environment, the impact of the contamination could range from having essentially no effect to drastically altering the behavior.

Contamination is also a common problem in the acidic environment. Many of the engineering metals used for high temperature, high pressure reactors are not stable in the acidic environment. Early work actually used quartz capsules that were pressure balanced with water.[131,132] Brittle materials such as quartz can tolerate high compressive loads, but pressure balancing adds another layer of complexity to the system. One could imagine that having such a capsule present would also act as another thermal barrier, making precise temperature control of the zones more difficult for an externally heated reactor. A more common practice is the use of a precious metal liner (usually Pt, but not necessarily, which is highly effective but also very expensive).[133–136] Early work lacked the liner technology or had liners which did not cover all components that might corrode. The result was significant transition metal contamination leading to optically absorbing crystals.[137] Higher purity crystals have been fabricated using precious metal capsules or better lined reactors, leading to highly transparent crystals such as those reported by Jiang et al., Mikawa et al., and Yoshida et al.[128,136,138] The grown material is transparent, but is still strongly colored. This coloration appears to have a significant yellowing, similar to the absorption ascribed to the V_{Ga}-H or V_{Ga}-O complexes described for the basic ammonothermal growth. This is at least partially supported by the significant presence of both H and O in acidic systems. Even with the removal of the transition metals from the impurity list, often O is a very prevalent contaminant. SIMS values for O concentrations tend to be around 10^{18}-10^{19} cm^{-3}.[121,138] Jiang et al. instead report a free carrier concentration of 1-3×10^{18} cm^{-3}, which indicates some shallow donor impurity such as O or Si is present in similar concentrations.[136] As discussed in the basic ammonothermal section, this contamination of O isn't necessarily a problem.

The feedstock issues discussed in the basic ammonothermal section are also present for the acidic system. The use of Ga metal has been explored, but the use of Ga metal consumes some of the NH_3 solvent and leads to increased pressure from the produced H_2.[123,139,140] It is more common for feedstock to be polyGaN, leading to the same requirement of clean polyGaN for high purity growth. Other Ga intermediates have also been explored, such as GaI_3 and $\{Ga(NH)_{3/2}\}_n$, but were mainly employed in an effort to produce cubic GaN.[131,141] The same problems may also arise with controlling the chemical potential difference as discussed previously.

Growth rates in the acidic system tend to be comparable or faster than those found in the basic system. Extreme growth rates as high as 40 μm/h (960 μm/day) have been reported, with 10-30 μm/h (240-720 μm/day) being more typical, although the actual mineralizer is not specified.[142] Bao et al. has reported growth rates of ~300 μm/day on m-plane and 200 μm/day on c-plane on HVPE grown seeds or 465 μm/day and 410 μm/day in the m- and c-directions, respectively, on a self-nucleated seed using NH_4F mineralizer.[121,143] Growth rates for c-plane GaN of ~150 μm/day and ~100 μm/day for NH_4I and NH_4Br, respectively, have been reported as well.[121] It would seem that NH_4F is an extremely promising mineralizer for fast growth. However, caution should be exercised when interpreting this data. Growth rate will be a complex function of mass transport, mineralizer content, mineralizer type, as well as reactor design and the temperatures involved. These values simply indicate what is known to be possible, but may not be the limit of what is possible.

Also similar to the basic ammonothermal growth, acidic growth of GaN has shown exceptional quality crystals. XRD FWHM of <50 arcseconds for the (0002) and TDDs in the range of 7×10^4-1×10^6 or FWHM of 10 arcseconds for the (0004) and TDDs in the range 10^2-

10^3 have been reported.[136,138] This is again indicative that exceptionally high crystal quality can be attained by both types of chemistry in the ammonothermal method and likely will be limited more by the seed than the chemistry.

2. Corrosion of Materials in the Ammonothermal Environment

"It is true that in human thought the particular precedes the general. Accordingly, the philosophy will not advance until the branches of science have made independent progress."
-Alfred North Whitehead, *Principle of Relativity*

Design of a chemical reactor can arguably start from two major constraints: the desired environment to be used (pressure, temperature, chemistry, etc.) and the materials that can provide this environment. If one does not know the material properties of the reactor then it cannot be safely designed for use in the specified manner. Many physical properties of materials are known, such as the elastic modulus, density, yield strength, etc., but the chemical corrosion aspect is environment specific. In fact, not only does it depend on the chemicals present, it also depends on the temperature and sometimes pressure. This chapter discusses the examination of a set of materials often used in engineering applications and their behavior in basic and acidic ammonothermal environments. Because the ammonothermal method is fairly niche, corrosion in this environment is not highly established. The extent of the examination is mainly restricted to the extent of corrosion or failure of the materials in an effort to determine whether or not they are safe to use. However, some trends will be discussed, perhaps lending themselves to further research which may clarify the corrosion mechanisms.

A. Basic Ammonothermal Corrosion with Na Mineralizer

"Mechanistically, dissolving alkali metals in water is a strongly exothermic process in which electrons move from the metal into the aqueous solution where they react to form hydroxide and hydrogen. The related heat release can be sufficient for melting of the metal, massive steam formation and ignition of the hydrogen gas, which leads to an explosive behavior"
-Ref. 144

The use of alkali metals or their amides, imides, hydrides, or any salt that only included only the alkali metal, N, and H as a mineralizer is the earmark of the basic ammonothermal technique. In early work, azides (N_3^-) were often used. This, however, produced significant amounts of N_2 gas and the purity of the chemicals was also somewhat lacking.[103,108] Later work switched over to amides (NH_2^-), but the most recent work tends to use Na metal that forms $NaNH_2$ in contact with liquid NH_3.[100,111,113,117,145] Regardless, the formation of NH_2^- species is likely, as is the formation of Na^+ (or other alkali metal ions). For all samples discussed in this section, Na metal was the mineralizer used. The materials investigated are categorized here as pure elements (ie Au, Ag, Fe, etc.), metal alloys (Mo alloys, precious metal alloys, etc.), carbides, nitrides, and oxides. At the end of each section, the general trend of useful stability will be summarized.

The corrosion runs of each sample were set up as follows. René 41 reactors were used and pressures of ~250 MPa were targeted. Reactors were stored in an oven to try to reduce water adsorption on the inner surface. The samples were cleaned in deionized water, acetone, and isopropyl alcohol (IPA) for 3 minutes each and characterized by weighing as well as visual inspection and taking pictures, thickness measurements using either a micrometer or calipers, as well as optical microscope images. The sealing bolts on the reactor were lubricated with a high temperature nickel antiseize. The samples were loaded into the reactor and placed in a glovebox where 1.5-1.7 g of sodium metal were loaded after the oxidized and mineral oil outside of the sodium was cleaved off using a knife. The reactor was sealed using a torque wrench with a Ni-200 gasket and then removed from the glovebox. Final torques were set on the sealing bolts to seal at high pressure and the reactor was weighed. The reactor was then evacuated and cooled using liquid nitrogen and filled with 30-35 L of gaseous NH_3 as

measured by a mass flow controller. The reactor valve was then closed and the reactor was allowed to warm up and dry (as the cold body condenses significant ice and then water). The reactor was weighed again before it was loaded into the containment vessel where heaters, thermocouples, and a pressure transducer were placed to control and monitor the reactor during the run. The containment vessel was then sealed to provide a hermetic and explosion proof barrier between the lab and the reactor. A N_2 purge was used while the run was going. After the run was over, the reactor was removed from the containment vessel and vented through a dedicated exhaust line. The produced pyrophoric materials (likely $NaNH_2$) were slowly reacted in a fumehood with H_2O/IPA mixtures of increasing H_2O content (starting from 5% H_2O and eventually cleaning with pure H_2O). The samples were then cleaned in H_2O, acetone, and IPA in an ultrasonic bath and subsequently characterized by weighing, optical photographs, as well as optical microscopy and sometimes scanning electron microscopy (SEM) including EDX.

Pure Elements

Many metals are known to be chemically active with oxygen (and thus why many metals oxidize). However, nitriding does not follow exactly the same trend. Our investigation of the pure elements is not fully restricted to metals, but it is strongly focused on it. In general, the pure elements don't have a positive stability trend in the basic environment.

Transition metals such as Co, Mo, Nb, Ni, V, W, and Fe tended to do rather well in the environment with Na mineralizer. Cu, Y, Ti, Zr, and Ta faired quite poorly. Significant degradation tended to occur as either dissolution of the material, as was the case with Cu and Y, or as chemically driven degradation of the physical properties of the material. Ti and Zr appeared to nitride or hydride and significantly embrittled, leading to cracking of the plates.

Copper does not form a stable nitride, as the crystalline form has a positive enthalpy of formation (and is thus likely to have a positive free energy).[146] One may speculate that Cu is dissolved in the form of $Cu(NH_3)_n^{2+}$, an ammoniate that is found in aqueous solutions of ammonium hydroxide and is generally quite stable.[147] Y does form a stable nitride. The formation of the nitride, however, does not protect Y in this case. Kempter et al. at first tried to directly nitride Y in N_2 at 900°C but found that it was more efficient to first hydride it at 550°C in H_2 and then nitride it at 900°C in N_2, yielding a cubic sodium chloride crystal structure with a lattice constant of 4.88 Å.[148] With Na mineralizer a substantial amount of H_2 is formed via the reaction $Na + NH_3 \rightarrow NaNH_2 + \frac{1}{2}H_2$, giving credence to this line of thought. The change in lattice structure is rather harsh in this scenario. Y has the hexagonal close-packed (HCP) crystal structure and YH_2 has a cubic structure, presumably the fluorite structure, and YN has the sodium chloride structure. The equivalent lattice distance for the HCP Y (taking $a = \frac{c*\sqrt{3}}{2}$) yields a lattice constant of 4.96 Å or (taking $a = a_{hcp} * \sqrt{2}$) 5.16 Å.[149] In contrast, YH_2 has a lattice constant of 5.20 Å and YN has a lattice constant of 4.88 Å.[148,150] The strain from going from YH_2 to YN is quite dramatic (lattice mismatch of 6.6%), which may cause stress buildup and eventually spalling of the surface and the formation of a powder. It would be expected, however, that tensile stress would be more destructive, leading to the possibility that the hydriding process, which also causes significant swelling, could cause the damage. Ti and Zr failed less from a corrosion perspective and more from embrittlement. Both metals actually fractured from the stress of the embrittlement and swelling. It is expected that the samples hydrided and possibly nitrided.[146] However, dramatic failure of the material in the form of spalling or powder formation was not observed. If the hydride and nitride process is the failure mechanism for all of these samples, then the

explanation for the why Ti and Zr did not spall as badly could be related to the nitridation. Both samples had significant gold coloration (attributable to the both ZrN and TiN) as well as black coloration (attributable to ZrH_2 and TiH_2) which is consistent with Ti being heated in NH_3 yielding TiH_2 and TiN.[151] Nitriding would help prevent hydriding, which may have protected the Zr and Ti. It is known that TiN can act as a H barrier and forms rapidly.[152,153] Ta also forms a weakly stable hydride (Ta_2H) and stronger nitrides and suffered a similar fate to Ti and Zr: significant embrittlement and darkening of the surface.[146] Again, the lattice change from the absorption of H is rather small and initially compressive (3.303 Å for Ta, 3.296 Å for TaH0.2, and ~3.35 Å for Ta_2H), although swelling occurs for the Ta_2H along with a loss of cubic symmetry.[154,155] The question of why the other metals did not corrode is a more difficult question to answer with certainty. Co and Mo may be somewhat stable as they are fairly weak nitride formers, although MoN and Mo_3N_2 were observed later. Nb likely hydrided and formed NbH_x, leading to the observed swelling of the sample as well as the brittle behavior, but no chemical characterization was done to determine if a surface nitride had formed.[156] Ni doesn't form a stable nitride, but a stable hydride may be possible. However, Ni alloy 718 has been found to have a nitride layer that forms at the surface, but it should be noted that this alloy contains 18 wt% Cr which is a strong nitride former.[129] V did pick up a golden color, indicating nitridation. V has a similar strain of ~5 % (comparing V-V distance) compared to Ti when nitriding, both of which are compressive strains.[157,158] Fe also does not form a stable nitride, although it will absorb some hydrogen even in liquid NH_3.[159] The Fe sample did embrittle and picked up some white coloration. A reasonable theory then remains that transition metals simply hydride and subsequently nitride in the basic ammonothermal system.

Another class of pure elements examined was the group II, group III, and group IV elements. Although these are really not a coherent classification, the elements discussed are not readily attached to other groupings. The elements examined include Al, Ge, Si, and Mg. The main reason for choosing these materials was not originally for reactor structural components, but rather to look into doping. None of these materials pass the stability test. Al could have been ruled out initially, as work had already been demonstrated showing growth of AlN from Al shavings with KN_3.[160] A white powder resulted from this run, presumably AlN powder. Ge and Si were co-loaded in the same run and were corroded to a lesser extent. Both also had white powder present, although this may have been from the Al sample, and fracture of the samples indicated stress. SiH_4 is known to be used as a Si source for MOCVD and HVPE and Si_3N_4 is also stable, corroborating the possibility of the hydriding and nitriding corrosion mechanism. Thermodynamically, GeH_4 is similar to SiH_4 and has been used in MOCVD as a Ge source.[161] Although only the enthalpy is available, Ge_3N_4 may also be stable in a strongly nitriding environment. Mg forms a stable nitride, Mg_3N_2, which reacts with water as well as a stable hydride and was also found to be highly unstable.[146,162] Mg also forms amides under ammonothermal conditions.[163] The failure came in the formation of a large amount of surface roughening and material loss through dissolution in either the NH_3 or the H_2O as well as embrittlement.

The last classification of pure elements was the precious metals. With the exception of Ag, all of the transition metals corroded very significantly. Ag, Au, Pt, and Pd were all investigated. None of these metals are known to form any stable nitrides. Unfortunately, the hydriding effects are not well known either. Pd is known to have a significant H solubility.[164] It should be noted though that for Au, Pt, and Pd, blackened surfaces and spalling were

common. In fact, in the case of Pt, a black powder was formed that had exceptionally high catalytic activity. During the cleaning process, a thin surface layer of isopropyl alcohol actually began burning in the presence of this black powder. Although no more characterization was done, this is consistent with the catalytic activity of Pt black (very fine Pt powder).

Pure elements tend to suffer degeneration from what appears to be hydriding and subsequent nitriding in the presence of Na mineralizer under ammonothermal conditions. Although the true thermodynamic free energies are not available for the compounds in question, the corrosion mechanism is at least reasonable and consistent with the little data available.

Metal alloys

Metal alloys can be stabilized by the interaction energy of one metal reacting with another. Compared to the ionic bonding (such as to O), this energy is usually lesser. However, alloying can significantly stabilize a material against attack, as can be found in the case of stainless steel. The Cr assists in protecting the austenite by forming a surface oxide that acts as a passivating layer. The oxide of Fe spalls off and thus if it was allowed to oxidize then the metal would corrode continually in the form of rust. In this section we will discuss the effects of alloying on Co, Cu, Fe, Ni, Pt, and W alloys in the ammonothermal basic system.

The only Co alloy tested was a Co-W-Al alloy with the composition $Co_{80}W_{10.6}Al_{9.4}$. Similar to pure Co, the alloy showed very little to no corrosion. Although Co and W would not be expected to corrode any differently here, one might suspect that Al could be leached out of the sample, causing roughening. The Co and W may act as N barriers, preventing

nitriding of the Al except at directly at the surface. However, no significant characterization was done other than mass measurements and visual inspection.

Two Cu alloys were tested in the system: brass 260 ($Cu_{71}Zn_{29}$) and Constantan ($Cu_{53}Ni_{47}$). Brass 260 blackened and lost significant mass while also embrittling. Constantan was much less affected. The surface took on a dull, matte finish but did not blacken or suffer any spalling. It would appear that the Ni does stabilize the Constantan alloy, although the reason for this is not known.

Fe alloys are the most common engineering material and thus were of great interest. Three alloys of stainless steel were examined: 15-5 PH, 17-4 PH, and 316L. All three had some level of success and had substantial amounts of Cr. This provides the passivated oxide surface. A golden surface coloration and mass gain of the 15-5 PH steel as well as EDX data indicate nitiriding of the surface, possibly the Fe but likely the Cr has a more stable nitride.[146] Both 17-4 PH steel and 316L steel behaved very similarly as well.

The only alloy of Mo that was investigated was titanium-zirconium-molybdenum (TZM). By most standards, this is barely an alloy, as the alloying percentage is very small, ~0.5 wt% Ti, ~0.08 wt% Zr, and 0.02 wt% C.[165] Similar to the pure Mo, TZM showed essentially no degradation. Later growths performed in a basic environment with GaN indicated that less of the molybdenum nitrides formed from TZM than pure Mo. It is not clear why this might be the case, but one could speculate that the alloying elements cause small amounts of lattice strain in grains. In the strained lattice the swelling from the introduction of N would be more energetically costly and, coupled with Mo being a weak nitride former in the first place, could reduce nitriding. There is no significant evidence to support this speculation at the moment.

Ni alloys were also of great interest. The chromel/alumel thermocouple alloys (type K), Hastelloy C-276, and Nicrosil/Nisil thermocouple alloys (type N) were investigated. All appeared mostly stable. The chromel ($Ni_{88}Cr_{12}$) and alumel ($Ni_{92}Mn_2Al_4Si_2$) picked up a light golden tint which would be consistent with nitriding of the Cr. Hastelloy C-276 ($Ni_{58.9}Cr_{18.7}Mo_{10.4}Fe_{6.2}Co_{2.7}W_{1.3}Mn_{1.1}V_{0.4}Si_{0.2}P_{0.1}S_{0.1}C_{0.1}$) also experienced surface discoloration, but subsequent EDX indicated no surface nitride. If the surface was an oxide layer, then perhaps it was dissolved thus removing the oxide and the parent metal to which it was bonded. Discussion of oxides can be found in the next section. Nicrosil ($Ni_{81.2}Cr_{15.7}Si_{2.8}Mg_{0.2}$) and Nisil ($Ni_{91.2}Si_{8.8}$) behaved similarly to the chromel/alumel junction, taking on a grayish to golden coloration. Again, it would seem likely that the Cr present is nitriding. It should be noted as well that both thermocouple alloy sets appeared to give accurate temperature measurements after the experiment.

Two Pt alloys were tested, $Pt_{78}Rh_{22}$ and $Pt_{91}Ru_9$. The $Pt_{78}Rh_{22}$ was slightly stabilized by the Rh present, but it still lost appreciable weight and embrittled. EDX of the sample indicated a non-uniform distribution of Rh with a high Rh inner core (26 %) and a surface of low Rh content (4 %). However, as the Pt sample that massively corroded was present in the same reactor as these samples, it is possible that Pt was deposited on the surface and Rh was not etched. Regardless, the Rh did not fully stabilize the alloy. The Ru did stabilize the Pt when alloyed. A slight weight gain was measured, possibly due to H absorption but also black spots were found on the sample. Unlike most metals, the $Pt_{91}Ru_9$ sample even retained its ductility which would indicate that if H was absorbed it was likely only a small amount.

Three W alloys were tested: $W_{74.7}Ni_{15.6}Cu_{9.6}$, $W_{74}Re_{26}$, and $W_{95}Re_5$. The $W_{74.7}Ni_{15.6}Cu_{9.6}$ alloy did darken slightly and take up a matte finish but no significant mass loss was observed.

Due to the form factor of the alloy, ductility observations were not possible. Both W-Re alloys behaved very similarly and took up a graying surface but also remained malleable.

Carbides, Nitrides, and Oxides

Carbides are often used in machining as they can significantly increase the hardness of the parent metal. However, the two materials investigated here are SiC and WC which are not generally used in machining. SiC is actually a wide bandgap semiconductor and rivals GaN as a research topic for power electronics. It has some potential as a GaN substrate as mentioned in chapter 1. In the basic system, the SiC did suffer some etching (evidenced by mass loss) as well as crystallographic features on the unpolished side of a single side polished sample. Interestingly, the slightly brown sample also became more colorless during the run. It is possible that impurities were removed from the sample, but this seems unlikely as diffusion would have to be extremely rapid. WC, which was really only 90-94 % WC, 6-10 % Co, and 0-4 % Fe, suffered only from slight surface pitting. The reason for the pitting is unknown, but loss of C to CH_4 formation and Fe_4N formation are two possibilities.

Hot-pressed boron nitride (HP-BN), pyrolytic boron nitride (PBN), and Si_3N_4 were also investigated. None of these fared well in the basic ammonothermal environment. Both forms of BN suffered from etching, but degradation of the physical structure of PBN also occurred. The HP-BN appeared to take up crystallographic faceting, as the initially matte surface sparkled afterwards which may indicate facets. Flakes of PBN came off of the PBN sample and black coloration was present. Si_3N_4 was etched and lost some mass. It is not that unlikely that the different nitrides are soluble, as the addition of mineralizer is designed to increase the solubility of GaN.

Oxides are a very common class of materials both for the ease of formation (many elements naturally oxidize in our atmosphere) as well as their usefulness as electrical and thermal insulators. The oxides examined here are relatively common and were partly chosen because of that reason. Single crystal aluminum oxide (sapphire), polycrystalline aluminum oxide, and machinable alumina (aluminum oxide with binder) were investigated and all suffered from significant dissolution. The single crystal sapphire wafer had macroscopic holes forming and suffered dramatic thinning while the machinable alumina sample crumbled from loss of structural integrity. Fused silica (amorphous SiO_2), quartz (single crystal SiO_2), and soda lime glass ($Si_{24.4}Al_{0.5}K_{0.6}Mg_{2.3}Na_{10.0}Ca_{2.5}O_{59.7}$) were also investigated and were all completely dissolved. Alumina silicate ($Al_{13.1}Si_{21.0}Fe_{0.8}K_{0.6}Ti_{0.4}O_{64.1}$) did not suffer quite as dramatically, but its structure was certainly compromised. Significant mass loss as well as swelling, spalling, and cracking characterized the sample. A glass ceramic ($Si_{20.7}Al_{7.9}Li_{3.2}Mg_{1.9}Ca_{1.4}Na_{0.6}Ti_{0.6}Zn_{0.6}Ba_{0.5}K_{0.4}Zr_{0.4}O_{61.8}$) and glass mica ($Si_{15.4}Mg_{8.5}F_{4.2}Al_{3.2}K_{2.1}B_{2.0}O_{64.5}$) both suffered similarly. The glass ceramic suffered a dramatic visible change where the sample changed from transparent and lightly brown tinted prism to an opaque, dark brown prism with significant cracks covering the entire surface. The glass mica only suffered surface effects which included loss of some of the surface due to spalling. MgO also showed crystallographic etching, but the dissolution was far less dramatic than most of the other oxides. Single crystal yttria-stabilized zirconia ($Zr_{29}Y_5O_{66}$) lost very little mass but did have evidence of crystallographic etching when viewed in difference interference contrast microscopy and the originally polished surfaces became diffuse. ZrO_2 also appeared to only lose a very small amount of mass with no other significant signs of etching or failure. Overall, oxides tend to be unstable in the presence of Na mineralizer. Given

the high H_2 pressure and the stability of water, one might speculate that the formation of H_2O and nitriding of the metal ions is a general corrosion method. Neither SiO_2 nor Al_2O_3 were stable and many of the samples tested may have failed due to the lack of stability in SiO_2 or Al_2O_3. The superior stability of MgO and ZrO_2 is not understood, but one possible explanation lies in the stability of sodium silicate and sodium aluminate species, which have very high formation enthalpy and negative free energy of formation.[146] Figure 10 displays the absolute mass loss as well as the relative mass loss of the oxides in the basic ammonothermal environment. Note that the trends show increasing Al_2O_3 and SiO_2 contents increases mass loss, with SiO_2 being more severe than Al_2O_3.

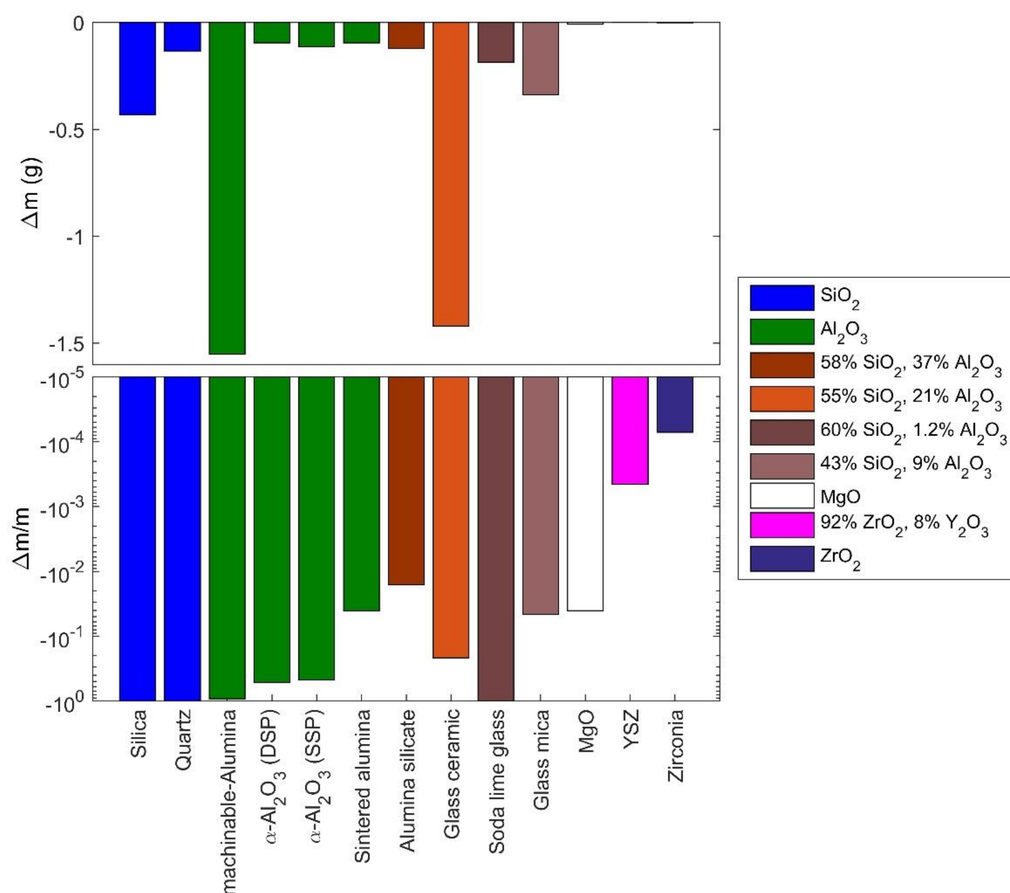

Figure 10. Absolute mass loss (top) and relative mass loss (bottom) of oxides in Na-NH_3 solution.

B. Acidic Ammonothermal Corrosion

"The potential for each of the component substances must have a constant value in all parts of the given mass of which that substance is an actual component, and have a value not less than this in all parts of which it is a possible component."
-J. Willard Gibbs, *On The Equilibrium of Heterogeneous Substances*

The use of halogens is the most common form of the acidic ammonothermal technique. Technically, anything that can produce NH_4^+ ions would be considered an acidic mineralizer, but usually either a halogen gas such as HCl or HF or an ammonium salt such as NH_4Cl or NH_4F are used. This section describes the observed corrosion of materials in the acidic system using NH_4Cl as a mineralizer. It will be noted here and throughout the section that often one finds materials that are very suitable for use in the basic system are very much unsuitable for use in the acidic system and vice-versa.

Loading of the reactor was very similar to the basic corrosion runs and thus only the differences will be highlighted here. Inconel 625 reactors were used with NH_4Cl because René 41 corrodes much more dramatically. It is important to note, however, that Inconel 625 was not in any way inert. Reactor bodies lost over 1 g of wall material for runs where the samples were found to be stable. Images of this corrosion are pictured in Figure 11. The samples were prepared in the same manner as in the basic runs, but instead of Na metal, ~1.40 g of NH_4Cl was measured out using a stainless steel spatula and placed in the reactor. An NH_3 fill of around 18-20 L was used to target a pressure of 100 MPa. All other closing procedures were the same. Unloading sometimes required allowing the reactor to leak into exhaust for as much as several days when reactor corrosion clogged the nozzle. On more than one occasion, leaking of the reactor by breaking the main gasket seal was necessary. For cleaning, no pyrophoric materials were generated so H_2O was used immediately. Machining was necessary to remove some metal deposits for several runs. It is also important to note that Ni-200 gaskets

were used and also corroded very significantly, losing more than 1 g of material. EDX of some of the red crystallites on a Co sample indicated $CrCl_x$. One theory is that the $Cr(NH_3)_6Cl_2$ forms, as very significant nitrogen (nearly 4:1) was also detected. Light elements such as N_2 also tend to be detected at lower concentrations than is actually present. A later scan of HVPE grown GaN indicated $Ga_{67}N_{29}$, which is likely an artifact of the measurement method.

Figure 11. Inconel 625 reactor body after a run with NH_4Cl mineralizer. Yellow powder that was highly soluble in water was often found (left) as were red crystallites (right). The red crystallites were water soluble but took much longer to dissolve than the yellow powder. Note also the scaling and spalling of the walls on the right.

Pure elements

As mentioned previously, materials that fared well in the basic system tended to do rather poorly in the acidic system. Of the transition metals, only Mo was truly unscathed. Later work with thin wires indicated some embrittlement, but initial samples appeared essentially completely unchanged. V and Nb also resisted significant corrosion but more significantly embrittled and swelled which is consistent with hydriding. The surface of the V sample became a light gold color and EDX analysis indicated VN formation. Nb did not change color but did increase in weight. Ti had mixed results. The initial results with Ti plate showed surface discoloration with a blackened surface. This is consistent with a hydrided surface, but

the black surface did not react with water. Oxygen contamination may have played a part, but the black color potentially could be a very rough surface that was nitride. No extra characterization was done with that sample. However, later a capsule was made solely of grade 5 Ti (6 wt% Al and 4 wt% V). The capsule suffered what looked like a pressurization and explosive event from within and the pressure in the reactor underwent a massive increase (+30 MPa). This is consistent with a hydriding event as observed by Baymakov and Lebedev.[166] TiN seems to be relatively stable, and thus it is possible that strongly nitrided Ti could be used in acidic ammonothermal systems. The nitride would even serve to protect the Ti underlayer from H absorption. Bare Ti, however, appears to suffer rather catastrophically. W appeared to have some small minor corrosion, but this may also have been deposition of reactor wall on the sample. The other transition metals investigated include Ta, Y, Zr, Fe, Co, Cu, and Ni. Two major types of corrosion can be characterized in the case of transition metals: the formation of hydrides or nitrides, as was theorized for corrosion in the basic environment, or the dissolution of the metal as a chloride. The formation of hydrides and nitrides was mainly addressed in the basic system and many of the elements that were stable in the basic system are not stable in the acidic. Ta, Y, and Zr appeared to suffer similar nitriding or possibly hydriding events. The Ta sample picked up a distinct golden color and literature reports cracking and “corrosion phenomena,” including cracking and roughening of the surface. Cracking could be due to swelling from hydriding, although they report no chemical analysis at the fractures and our data also lacks any chemical characterization. Y was completely disintegrated in a similar way to the sample in the basic system. Zr also disintegrated and formed a powder very similar to the Ti capsule that hydrided and nitrided. With a similar propensity to form hydrides and nitrides, the similar Zr corrosion result indicates that it also

probably formed hydrides and nitrides. Fe, Co, Cu, and Ni all suffered dramatic corrosion. The Fe embrittled, cracked, and oxidized upon exposure to air. This is consistent with iron chloride formation as iron chloride will oxide upon exposure to both air and water. Co appeared to also partially go into solution with significant discoloration. EDX of the Co gave small Cl signals in regions where Fe and Co were detected, making it unclear if the Cl was bound to Co or Fe. Cu likely went into solution and formed an amalgam with the other samples present, making it indistinguishable from the brass 260 and Constantan that it was loaded with. Ni similarly corroded and had a porous surface afterwards, which indicates local corrosion. This could also point to Cl corrosion but is not definitive.

The group II, group III, and group IV elements also corroded very significantly. Al was disintegrated, forming a brown powder that could be AlN, although this was not verified. Ge and Si both gained mass, indicative of either deposition from the walls or the other samples that were co-loaded with them (co-loaded samples include Fe and Al). The Si sample has brown spots which could also be Si_3N_4. Mg completely dissolved and no sample was recovered post-run.

In stark contrast to the basic ammonothermal environment, Ag was the only precious metal that showed corrosion. Pd and Pt both had a slightly darkened surface which could be corrosion or reactor wall deposition but neither lost their ductility. Au had no surface discoloration and also did not lose its ductility. The reduced H_2 pressure may reduce hydrogen embrittlement but no effort was made to characterize this effect.

A straightforward theory for the difference in corrosion phenomenon is simply the formation of soluble chloride intermediates. However, essentially all of these transition metals form stable chlorides, including Mo, V, and Nb which suffered no significant chemical

degradation. From transition metal ligand theory, we can instead consider the effect of the NH_3 molecules as ligands and see what effect one might expect. Although free energies are not available in these cases, one can use the enthalpy as a metric to compare. Figure 12 shows a bar graph indicating which samples showed corrosion effects consistent with Cl attack vs enthalpy of the chloride formation. Note that these enthalpies are at room temperature and atmospheric pressure and may approximate the reaction in the ammonothermal environment but will not be reliable for the calculation of any thermodynamic quantities. The enthalpies are also normalized to the number of Cl atoms in the molecule, thus characterizing the interaction on a per metal-Cl bond basis.

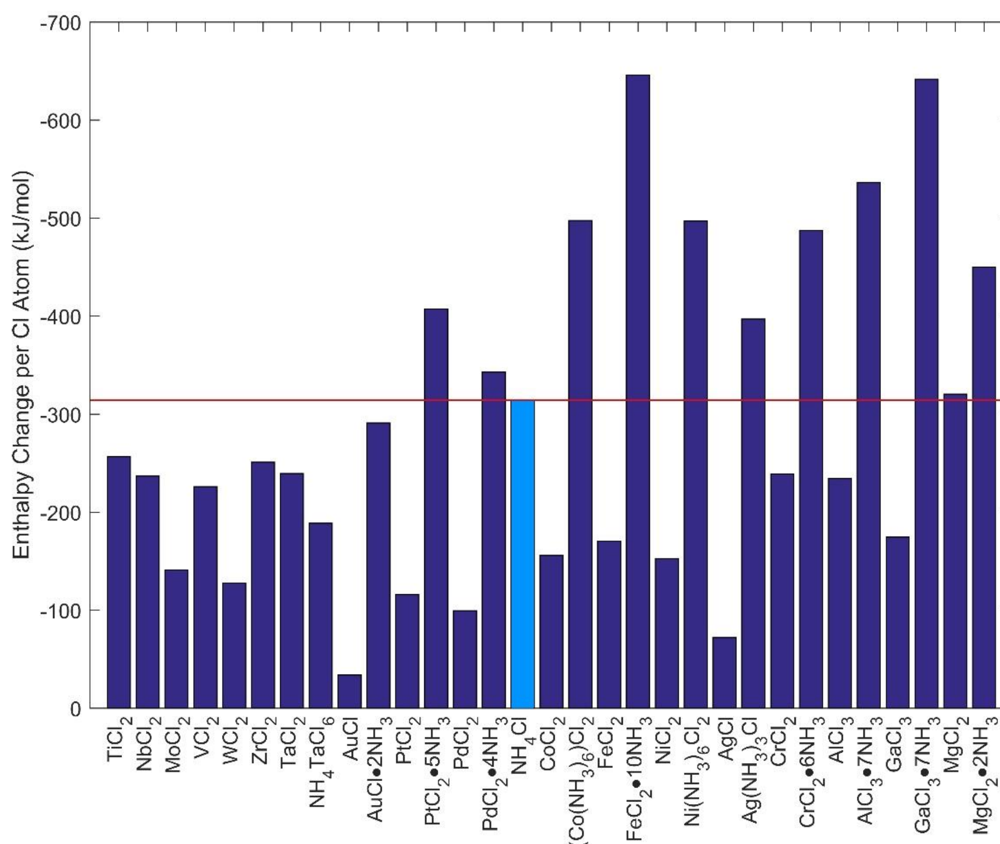

Figure 12. Plot of enthalpy change per Cl atom present in chloride crystals known to form. The light blue bar is the enthalpy of the NH_4Cl mineralizer, the reference for corrosion. It would be suspected that enthalpies

with a less negative value are unlikely to form while more negative enthalpies are likely to form. The red line is a guide to the eye indicating the value of the NH_4Cl enthalpy. All cations left of NH_4Cl on the graph were not found to degrade by a chloride formation while those to the right are suspected to form chlorides in situ.

The enthalpy change with the different cations indicates the strength of the M-Cl bond (where M is the metal). Only compounds that solids (and thus the enthalpies of the solids) are displayed, as in our experiments any gases would escape and be undetectable. Elements that did not appear to corrode or only formed nitrides or possibly hydrides are displayed left of NH_4Cl. Elements to the right formed powders or were found to directly form chlorides. The exception is Zr, which is displayed on the left. Although a more direct chemical measurement would be desirable, the similarity to the TiN/TiH_2 formation found for the Ti capsule as well as the similar propensity to form a hydride or nitride between Ti an Zr indicates that the Zr powder formation was most likely due to hydriding and subsequent nitriding and may not have required any chloride intermediate. Subsequent EDX of the powder removed from the surface indicated similar amounts of N and Zr with less Cl (32% and 33% for N and Zr, 23% for Cl). It may be ZrCl2, but it may also have been ZrN and NH4Cl. It has been determined through measurements of GaN that the N concentration (presumably due to the small atom size) is often underestimated (stoichiometric HVPE GaN was measured at 67% Ga, 32% N). One can see that the graph displays a somewhat convincing trend, where the enthalpy of known chloride and chloride ammoniates at room temperature is an indicator as to whether the metal will corrode significantly or not. Pt and Pd are exceptions to this, but the formation method for the chlorides of these precious metals requires a very strong oxidizer, such as nitric acid in aqueous solutions.[167] This could be an improved method for corrosion resistance in these systems. If TiN or ZrN are truly stable against chloride attack, then capsules or even reactors may be suitable as long as a significant nitride layer is formed. The nitride will

permeate into the metal and be self-regenerating while also acting as a H_2 barrier to prevent hydride formation. Perhaps Ta could also be used in a similar capacity, forming TaN. This suggestion neglects thermal expansion mismatches and stresses from the nitriding, but the formation of a compressive stress at the inner wall is actually a useful method for reactor design and is used in autofrettage.

Metal Alloys

In this section the stability of alloys is discussed in the acidic system. Most of the alloys behaved very similarly to the parent elements, indicating that any new phases developed by the alloying do little to prevent corrosion. However, there are a few exceptions.

The Co-W-Al alloy showed very small amounts of corrosion in contrast to both Co and Al. A small mass loss was measured, however, and subsequent EDX indicated a significant change in the surface. Bulk concentrations of the cations were 80 % Co, 10.6 % W, and 9.4 % Al or ratios of 68:9:8 for Co:W:Al. EDX of the post-run sample showed a dramatic loss of Co and a significant loss of Al with relative ratios of 28:41:20. It should be noted that EDX indicated a much higher fraction of O (55 mol %) on the sample surface. This is the only example in which alloying indicated a highly significant effect, but it does not rule out other alloys as possible stabilizing agents.

In contrast to the Co alloy, Cu alloys corroded in a manner similar to Cu. In fact, the alloys formed an amalgam that could not be distinguished from the pure Cu present.

The stainless steel alloy system is often protected by an oxide layer which is similar throughout most of the stainless steels. Cr is usually the oxide former and the alloys tested include 15-5 PH, 17-4 PH, and 316L stainless steel, all of which have significant Cr. It is not surprising then that each of the Fe alloys performed rather poorly. In each case, the sample

originally appeared black post-run and oxidized upon exposure to water. This is consistent with iron chloride, which appears dark green-black.[168] Although Cr was not directly tested in any of our samples, this is also consistent with $CrCl_x$ forming from Cr in the reactor walls. The Cr surface layer is then removed and the exposed Fe matrix is also attacked by the Cl.

The only Mo alloy tested was TZM. As mentioned previously, this is very nearly pure Mo and it is not surprising that it behavior similarly. The sample experienced no weight or thickness changes, but did take on a blue, leopard-stripe pattern. This could have been oxidation, as the NH_4Cl is known to have oxygen contamination, but subsequent runs did not have this issue. A definitive reason for this discoloration is not known.

The Ni alloys had some improvement but were still fairly vulnerable to corrosion. The chromel/alumel and Nicrosil/Nisil thermocouple wires were heavily corroded and lost most of their ductility. Hastelloy C-276 initially appeared to be fairly stable. It took on a black coloration, but there did not appear to be significant degradation. A follow up experiment was done were a capsule was made from the Hastelloy C-276 and the mineralizer was placed inside. The capsule, which was not hermitically sealed but did have a cap, was placed inside the reactor and filled with NH_3. The capsule inside experienced significant corrosion and the 8.99 g cap lost .1 g of material (see Figure 13). It is speculated that without other, less stable alloys present, Hastelloy C-276 corroded due to the formation of chromium and nickel chlorides.

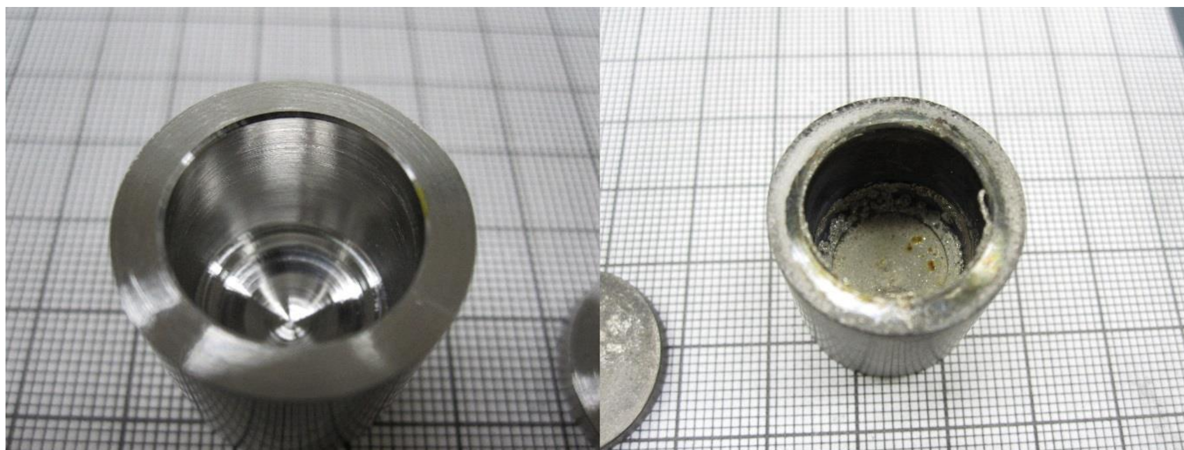

Figure 13. Hastelloy C-276 capsule before (left) and after (right) acidic ammonothermal run. NH_4Cl powder was placed directly inside the capsule and the cap was placed on top before the capsule was placed inside the reactor. Crystallites formed on the inner walls and bottom of the cap and pitting was clearly visible.

The precious metal alloys also behaved similar to their parent metals. Both Pt alloys tested showed a slight increase in thickness but remained ductile. They also showed a slight darkening of the surface, which may by deposition of the reactor wall. However, this was not characterized.

The W alloys were mostly stable in the acidic environment. The $W_{74}Re_{26}$ and $W_{95}Re_5$ both showed not significant change in mechanical properties. A slight dulling of the surface was visible, but this also could have been reactor wall deposition. However, the $W_{74.7}Ni_{15.6}Cu_{9.6}$ alloy did corrode. A brown surface layer coated the sample with some isolated red and green spots. The red spots may be $Cr(NH_3)_6Cl_3$ deposition from the reactor wall. The green spots may be CuCl with $CuCl_2$ impurities or possibly $NiCl_2$.[169–171]

Carbides, Nitrides, and Oxides

In general, the carbides, nitrides, and oxides respond rather well to the acidic ammonothermal environment. MgO is one major counterexample to this trend, but it certainly seems that oxides are far more stable with NH_4Cl rather than Na minerazlier.

SiC and WC both appeared to suffer little to no effect. The SiC underwent a significant color change which may have been due to surface deposition from the reactor walls. No mass or thickness change was detected. WC exhibited patches of blue similar to those seen on the TZM sample (although these samples were not co-loaded) and lost a small amount of mass while slightly swelling. Given that both Fe and Co are alloyed with this WC, a reasonable assumption would be that these metals were leached out of the sample. However, no chemical characterization was done to confirm this.

Chloride chemistry is known to have a higher solubility of GaN compared to Na chemistry, but in the case of HP-BN, PBN, and Si_3N_4, the solubility would appear to be much less compared to the Na system. However, HP-BN and PBN both suffered mass loss in spite of visible rust-colored deposition present on both samples. The roughness of the sample surfaces prevented removal of the deposition without also abrading away sample mass. Si_3N_4 also took on rust-colored deposition while still losing a small amount of mass, indicating some solubility.

While most oxides were heavily corroded in the basic system, most oxides showed very little to no corrosion in the acidic system. Single crystal aluminum oxide, polycrystalline aluminum oxide, and machinable alumina all exhibited the same rust-colored deposition but appeared chemically stable. The machinable alumina rust-colored deposition sometimes came off in flakes when agitated, but the material was an unfired ceramic and was thus already fairly fragile. Further testing of polycrystalline aluminum oxide in a capsule (a tube of Al_2O_3 with two spheres of Al_2O_3 to encapsulate the mineralizer) indicated that some etching may be present. However, the mass loss was 0.95 mg. If this loss is true and from only Al_2O_3, then this much material loss could result in 1.7×10^{19} cm^{-3} for a 1 cm^3 piece of GaN which would

indicate that Al_2O_3 in an acidic system has the potential for significant oxygen contamination. Fused silica and single crystal quartz showed no significant corrosion and even in the capsule design the fused silica increased in mass (single crystal quartz was not tested in a capsule). The mass gain was on the order of 2 mg and the capsule did appear to have rust-colored deposition which could not be abraded away without damage to the capsule. Soda lime glass ($Si_{24.4}Al_{0.5}K_{0.6}Mg_{2.3}Na_{10.0}Ca_{2.5}O_{59.7}$) became a deep red and the initially smooth surface became wavy on mm length scale. Given the high content of Na as well as the presence of Ca and K, it is not surprising that some interaction occurred. The oxides of the alkali metals may very well be soluble in supercritical NH_3 and leaching of these elements from the glass could have driven the observed changes. The alumina silicate ($Al_{13.1}Si_{21.0}Fe_{0.8}K_{0.6}Ti_{0.4}O_{64.1}$) sample also appeared to suffer no corrosion and was subsequently tested in the capsule design. The sample within the capsule picked up 4 mg of mass, likely reactor wall deposition. However, the possibility remains that some etching occurred since the Al_2O_3 capsule had a significantly higher surface area and lost a very small amount of mass. Glass ceramic ($Si_{20.7}Al_{7.9}Li_{3.2}Mg_{1.9}Ca_{1.4}Na_{0.6}Ti_{0.6}Zn_{0.6}Ba_{0.5}K_{0.4}Zr_{0.4}O_{61.8}$) changed color dramatically, picking up a dark brown coloration and exhibited internal cracking throughout the sample. It should be noted with the glass ceramic that it even exhibited changes in pure NH_3, picking up a yellowish coloration. Glass mica ($Si_{15.4}Mg_{8.5}F_{4.2}Al_{3.2}K_{2.1}B_{2.0}O_{64.5}$) exhibited rust-colored stains on the surface and still lost mass, indicating some etching was occurring. Under acidic conditions, MgO dissolved and no sample was recovered from the run. Yttria-stabilized zirconia and zirconia both fared quite well. Yttria-stabilized zirconia took on the rust-colored stains and showed mass loss, but during the run a corner of the sample was chipped thus

obfuscating reason for the mass loss. The zirconia, however, lost mass and also changed color from white to a dark purple. The reason for this coloration is unknown.

C. Conclusions on the Corrosion Study

"The first of these tasks, namely, that of establishing the principles which are to serve as the starting point of his deduction, is of an entirely different nature… The scientist has to worm these general principles out of nature by perceiving certain general features which permit precise formulation, amidst large complexes of empirical facts."
-Albert Einstein, *Inaugural Address to the Prussian Academy of Sciences*

From a practical standpoint, a material does not need to be fully corrosion resistant to be useful. As long as the corrosion does not inhibit or contaminate the growth or cause safety concerns then it can be deemed acceptable. Such is the case with materials that may be applied as single use gaskets. With this in mind we can state that many of the pure elements are reasonable materials to at least investigate. For the basic system these include Co, Mo, Ni, Nb, Ag, Ta, W, V, and Fe. Useful alloys include $Co_{80}W_{10.6}Al_{9.4}$, Constantan ($Cu_{53}Ni_{47}$), the stainless steels (15-5 PH, 17-4 PH, and 316L), TZM, chromel/alumel ($Ni_{88}Cr_{12}$)/($Ni_{92}Mn_2Al_4Si_2$), Hastelloy C-276 ($Ni_{58.9}Cr_{18.7}Mo_{10.4}Fe_{6.2}Co_{2.7}W_{1.3}Mn_{1.1}V_{0.4}$-$Si_{0.2}P_{0.1}S_{0.1}C_{0.1}$), Nicrosil/Nisil ($Ni_{81.2}Cr_{15.7}Si_{2.8}Mg_{0.2}$)/($Ni_{91.2}Si_{8.8}$), $Pt_{91}Ru_9$, $W_{74.7}Ni_{15.6}Cu_{9.6}$, $W_{74}Re_{26}$, and $W_{95}Re_5$. For the acidic system the useful pure elements include Au, Mo, Nb, Pd, Pt, W, V, and Ti while the useful alloys include $Co_{80}W_{10.6}Al_{9.4}$, TZM, $Pt_{78}Rh_{22}$, $Pt_{91}Ru_9$, $W_{74}Re_{26}$, and $W_{95}Re_5$. In the case of carbides, nitrides, and oxides, the basic system has proven highly corrosive. SiC and WC along with yttria-stabilized zirconia and ZrO_2 appear stable while essentially all oxides with Al_2O_3, SiO_2, or MgO components corrode significantly. In the acidic system, nearly the opposite is true: Al_2O_3, SiO_2, and ZrO_2 are all fairly stable. SiO_2 shows the least changes, while Al_2O_3 may vaguely dissolve and ZrO_2 shows discoloration but not significant failure from an engineering perspective. MgO also corrodes in the acidic

system. It should be kept in mind that "useful" here is a term that is applied to structural components in the system. For use as dopant sources or some other chemical interaction, the act of corrosion may indicate a use that is not highlighted here.

3. Design of a TZM Reactor and Bulk Growth of GaN with NH_4Cl Mineralizer at High Temperature

"In the temple of Science are many mansions, and various indeed are they that dwell therein and the motives that have led them thither."
-Albert Einstein, *Address on the occasion of Max Planck's 60th birthday*

The previous two chapters seem to have little to do with one another. One is concentrating on growth of GaN and the other focuses on the effect of mineralizers on materials in supercritical ammonia at high temperature. The intersection of these topics comes together in an effort to design a robust reactor that is capable of growing high purity, high quality GaN controllably. This goal has an added constraint that is not previously mentioned which is the structural material of the reactor must have high strength (and hopefully resistance to creep) at high temperature. The ammonothermal environment requires somewhat high pressures (usually described as moderate in lieu of the high nitrogen pressure method which uses >1 GPa pressure). For acidic growth, the standard pressures for growth are around 80-120 MPa and thus the reactor designed and described in this chapter targets that pressure range as a standard operating pressure. The first section will describe some of the important mechanical properties of TZM and the design of the reactor. The second section will discuss the GaN grown in the reactor and the characteristics as well as general behavior trends observed.

A. Design of a Tube Reactor Made of TZM

"The study of material behavior under pressure is of interest to investigators in a wide variety of disciplines. However, regardless of the specific area of interest, the first requirements of any investigation in this field are a suitable vessel to contain the required pressure and the specific experiment, and a means of generating the pressure."
-Ref. 172

TZM is a pseudo-ductile material at room temperature. This really means that the ductility of TZM depends on how it is stressed. In tensile stress, TZM can elongate and shows some

signs of ductility at temperatures as low as -50°C. However, using the fracture strength as the ductility criteria, where the ductile-to-brittle-transition is indicated by a sudden and significant increase in the fracture strength, the ductile region doesn't begin until 100-150°C. This ductile behavior also depends on the orientation of the stress with respect to the grains, as TZM often has sheet-like grains.[173,174] TZM is also a high strength, refractory alloy with a recrystallization temperature of 1400°C (the temperature at which grains grow and defects are eliminated).[175] TZM is also known for being creep resistant ($<10^{-6}$ h^{-1} at 1100°C and 200 MPa).[175] A stress of 200 MPa is comparable to the stress on the inner wall of a reactor with a 2.5:1 outer to inner diameter ratio and an internal pressure of 140 MPa. However, 1100°C is also significantly higher than the temperatures where ammonothermal growth has been done. Oxidation is also a significant problem for the molybdenum alloys. Smolik and Petti have performed mass loss measurements on TZM samples in air and found that a loss rate of 6.24 µm/h at 599°C occurred due to oxidation and volatization of the oxide.[176] Ammonothermal growth runs can last hundreds to thousands of hours and such an etch rate could be catastrophic. Even if the oxide is not volatilized, internal oxidation of the Zr and Ti can further embrittle the TZM.[165] This can be combated by either removing oxygen from the environment or coating the TZM with an oxidation resistant material such as TiN. In the first reactor body, both methods were applied but the second reactor body is not TiN coated.

The original inspiration for the tube reactor design was the simple high pressure tubing design with a cone-in-cone seal. Standard seals for pressurized systems often use elastomers (commonly o-rings) but at very high pressures and temperatures elastomers can decompose or simply be extruded. Thus, metal-metal seals are required. Metal cone-in-cone seals are common for high pressure applications and are still commonly used today with stainless steel

tubing.[172] The design is straightforward and simple: two mating parts consist of a male cone and a female negative cone in a solid metal (see Figure 14). The male and female cones have a slight mismatch in angle (although this is not strictly required) and the line at which the cones first contact will form the seal. The ideal situation is to have highly polished surfaces and only elastic deformation occurs, thus making the seal completely reusable. However, slight imperfections in the machining usually requires that plastic deformation also takes place to form a strong seal. Since the pressure inside will force the male cone outward, the seal will be somewhat reinforced by an internal pressure. This is referred to as a self-energizing seal, where the pressure involved reinforces the seal, and is generally necessary for exceptionally high pressures. The required elastic/plastic deformation that occurs requires some initial sealing force that is supplied by the bolts also used to hold the sealing surfaces together.

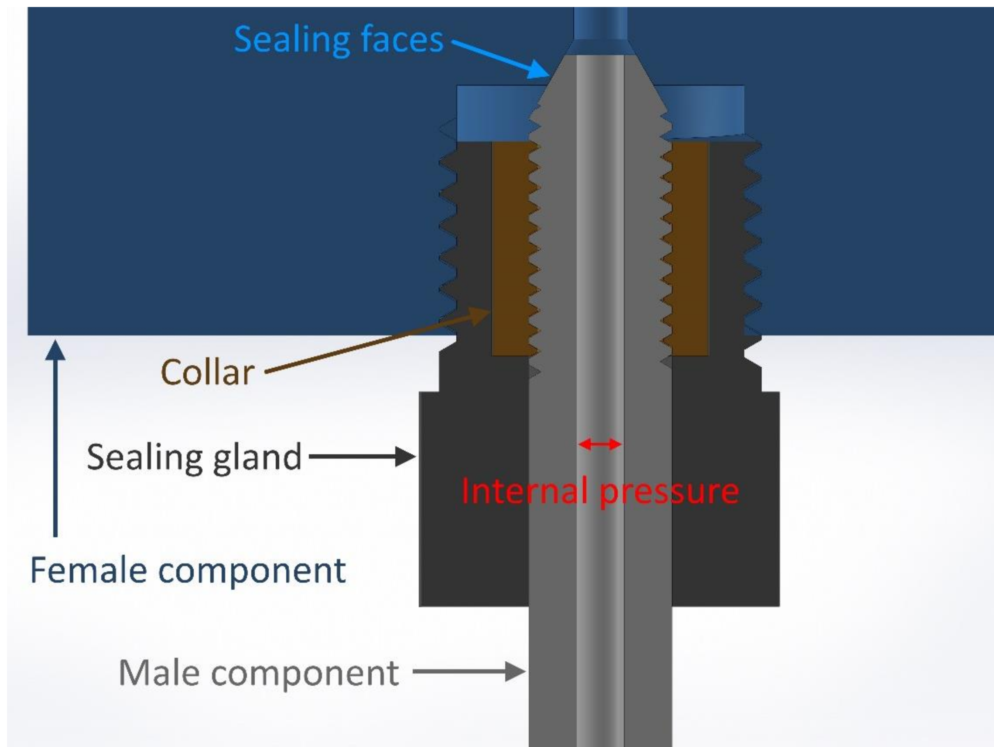

Figure 14. Cone-in-cone seal design. The light gray is a male component with a male cone, the dark blue is the female component with the female cone. The collar creates a

surface that the gland can employ a force against to press the male component into the female component.

One important thing to remember with this sealing method is the requirement that the sealing components have a certain amount of ductility. One could imagine the extreme, where a completely brittle material such as glass, is squeezed by being forced into a cone shape (the male component being forced upwards into the female component in Figure 14). A brittle material will not deflect inward but instead either chip or crack. With this sealing method, the result was similar with TZM. The seal also required a compliant layer between the cones. Initial tests with the bare cone-in-cone failed to provide any significant seal. A Nb washer was cut to fit around the tip of the cone to provide the compliant layer and successfully created a high pressure seal. However, high pressure and temperature runs lead to failure of the tip of the reactor body. The male cone began to crack. After remachining and completely removing the crack from the body, several more high pressure runs indicated that this cracking phenomena was repeatable and thus not sustainable for a long-term reactor design. Figure 15 shows an optical photograph of the male cone post-run with both visible surface cracks and plastic deformation.

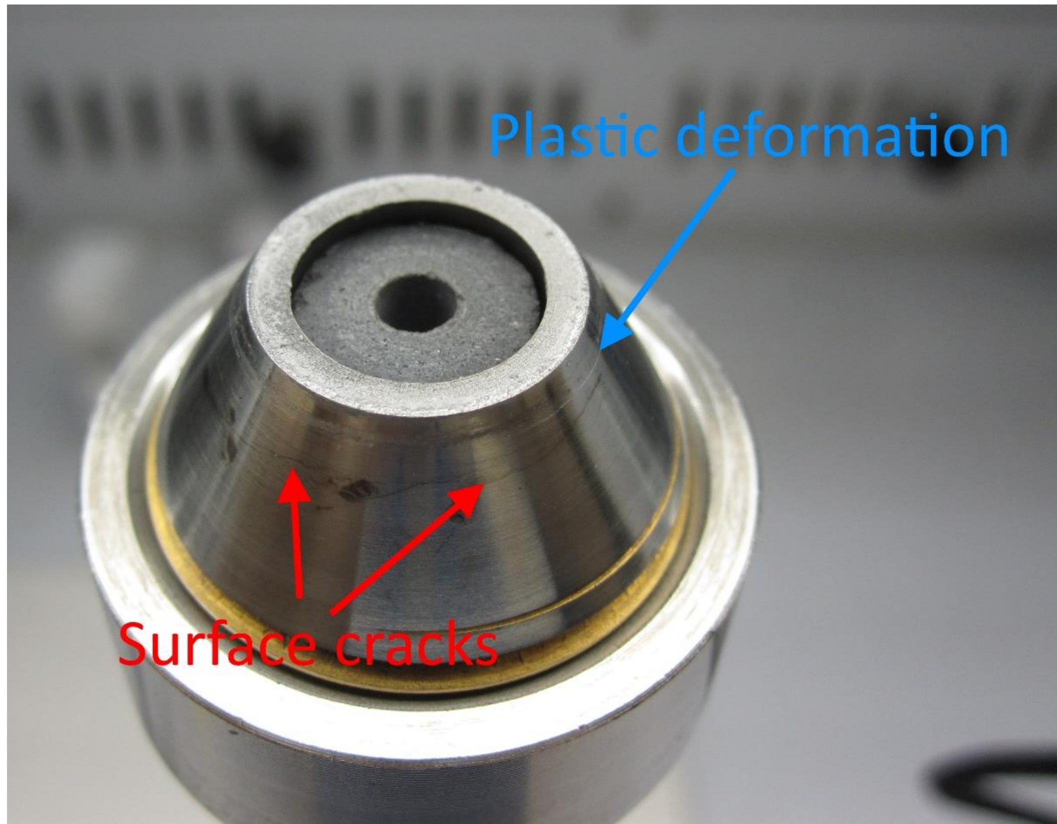

Figure 15. Photograph of reactor male cone leading to the head assembly. Both plastic deformation (essentially an indentation of the metal surface due to compressive stress) as well as surface cracks are present. The surface cracks propagate around much of the cone and are suspected to be either due to the unsupported cone or compressive stress upon sealing.

The clear signs that a standard cone-in-cone design would not work were followed by the concept of using a stress intensifying feature to increase the pressure at the seal point while not placing a large force on the reactor body itself. For the sake of being simple to machine, this feature needed to be small and mechanically robust. A small bead was decided upon with a radius of curvature of 1/16th of an inch and a total height of .02 inches (later changed to 1/32th of an inch and a height of .02 inches). The bead with a curvature circumvents the issues of being sharp and potentially fragile when compared to a knife edge. When pressed against a flat surface the bead also has a tangent line around it that can form a small sealing surface

that will sustain a high pressure with only a moderate force on the reactor body. Figure 16 shows a model view and the machined reactor body with the seal design.

Figure 16. Bead seal design. The schematic (left), the cone-in-cone body adapted to the bead seal with a 1/16th radius (middle), and the top view of the bead seal (right). The bead design requires a compliant gasket to plastically deform to create the seal.

The bead design itself (without a gasket) is difficult to seal because the bead would need to be exceptionally well polished and nearly perfectly aligned, thus a compliant metal gasket is used to enable a lower force seal. This also reduces the wear on the bead by allowing the gasket to flow rather than deforming the bead. However, the bead will still wear and need remachining occasionally. Some of the design features from the cone-in-cone design are still used. The method for producing an upward sealing force was kept, which is the reason why the reactor body is still threaded. It is interesting to note that the gasket and bead design is actually not a self-energizing seal but the design is still quite effective.

Sealing is one of two major design constraints for a safe reactor. The second constraint is that the reactor can handle the required pressure and temperature (note that we are already assuming that chemical corrosion is not an issue). While 100 MPa seems like a high pressure, by the standards of extreme pressure systems it is actually rather mild. Davidson and Kendall wrote a technical report in 1969 that detailed extremely useful information on the practical theory of high pressure vessel design. Their discussion is applicable for vessels designed for

operating pressure as high as 55 kbar (~5570 MPa). However, their work is still highly applicable to the ammonothermal regime and was consulted in pressure containment design. Many TZM reactors have also been used in geological research, including William's design that used copper gaskets and coned connections and was usable up to temperatures of 1200°C at 100 MPa.[177–181] The most straightforward design is to have multiple components that are solid, monolithic pieces. As TZM is brittle at room temperature, this reduces the likelihood of crack formation as only joints will have bends. The pressure rating for the reactor body is shown in Figure 17. Although the data is the best available, it should be noted that TZM from different manufacturers has had yield and tensile strength values that differ by as much as 25%.

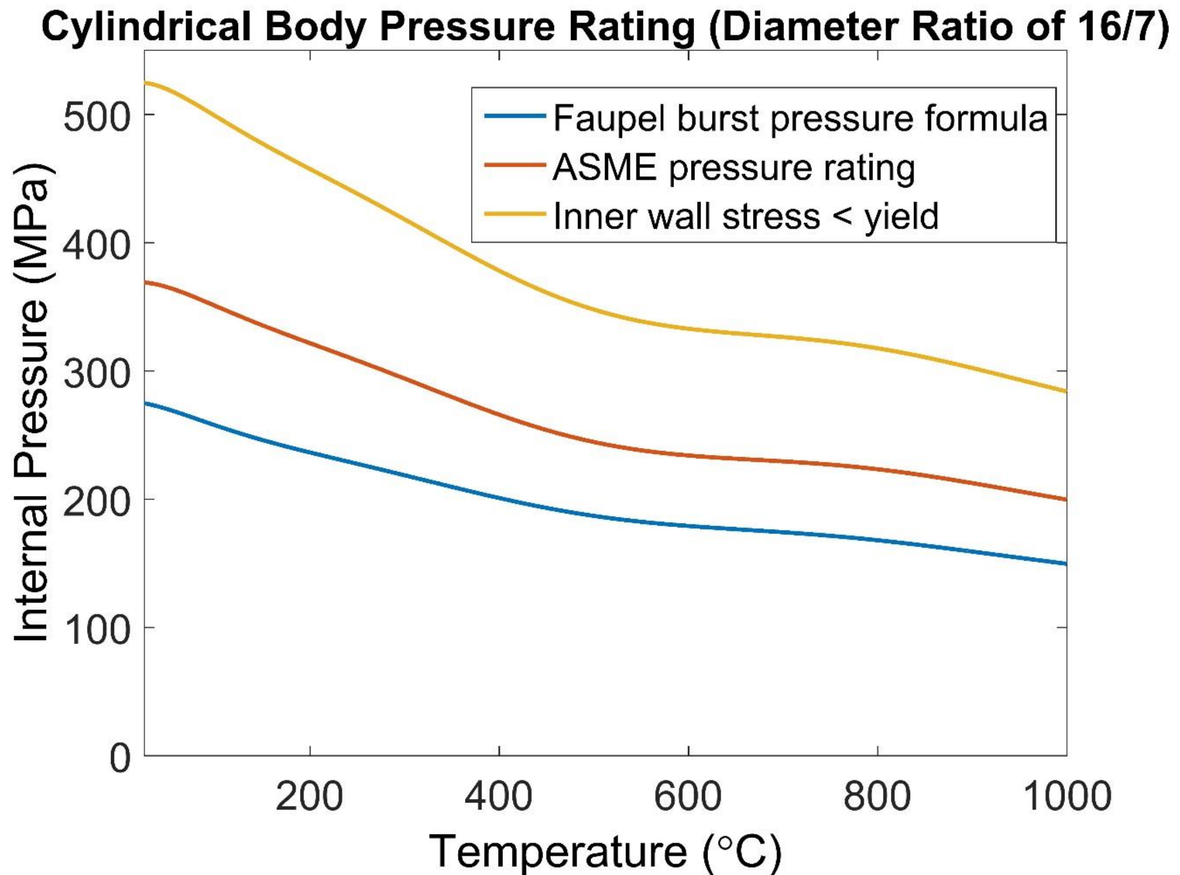

Figure 17. Pressure ratings for a cylindrical body with an outer to inner diameter ratio of 16:7. The different methods for calculating the safe pressure are shown by using Faupel's burst pressure formula, the ASME pressure guideline for monoblock cylinders, and the Von Mises stress calculation to ensure the inner wall stress is less than the yield stress of the material. The Faupel burst pressure includes a safety factor of 4.

All of the pressure ratings in Figure 17 assume the reactor body is the pressure limiting component. Faupel's formula considers both the ultimate tensile strength of the body material as well as its yield strength in the equation $p_{burst} = \frac{2}{\sqrt{3}} * \sigma_y * \left(2 - \frac{\sigma_y}{\sigma_{UTS}}\right) * \ln(k)$ where σ_y and σ_{UTS} are the yield strength and ultimate tensile strength of the material, respectively, and k is the outer to inner diameter ratio. The calculation above displays ¼ of the burst pressure, as safety factor of 4 was used. The inner wall must also not reach the yield point as it is not desirable to generate defects in the reactor by yielding the reactor wall. Yielding the inner wall is actually used in the case of autofrettage. However, those materials are ductile materials and

thus are acceptable to approach the yield point in a controlled manner. The other components of the reactor are standard components made by High Pressure Equipment Company and are made of 316 stainless steel. The stainless steel parts are rated to 30,000 psi (200 MPa). As the body does not approach this pressure rating, the body and the seals are considered the pressure limiting components.

The usefulness of the modular reactor design extends beyond the simplicity of calculating strength and failure scenarios and extends into reactor maintenance. Testing of components can be done with separate pieces to determine leak points and replacement parts can be more easily fabricated. The use of a tube with a sealed end requires knowledge of the radius of curvature at the bottom of the bore to know the stress and potential cracking or failure events that may follow. An open tube with seal points at both ends doesn't require this knowledge. The open bore also facilitates cleaning as well as visual inspection of the reactor walls in the bottom zone.

Testing of the reactor design really has three major steps, the first of which is a high pressure cold test. To accomplish this task, a high pressure generator from High Pressure Equipment Company (model 31-5.75-5 extra capacity high pressure generator) was used. Care must be used when doing this with a brittle material such as TZM. Small crack propagation may lead to catastrophic failure. However, TZM works well in tensile loading and in this case no bending stresses are involved, thus testing was deemed reasonable. To prevent the possibility of explosive decompression of the pressurized fluid, water was used. Leakage of high pressure gases will lead to a very large volume expansion while a fluid such as water will only expand slightly to alleviate the pressure. Thus, no explosion hazard exists because little momentum can be imparted. Testing of the TZM occurred at room temperature and 150-175

MPa. The pressure was left for a minimum of 30 minutes, but generally longer times were used. The leakage of water also allows the experimenter to determine where the leak is coming from. Again, this is extremely useful as the junction of each section of the reactor is a potential leakage source. A He detector with a vacuum source was also used occasionally, but this lacks the pressure component of the leak scenario for a running reactor.

The second leak test is the high temperature leak test. This is accomplished by ensuring the reactor is leak tight consistently using the cold leak test method first and then running the system with NH_3 gas. The reactor is sealed and pumped out and filled with N_2 gas and then pumped out again before filling with NH_3 gas. The system is filled with NH_3 in the same way as for a normal growth run (see section C of this chapter). The reactor is loaded into resistive heaters with silica ceramic insulation and taken up to growth temperatures (generally 600°C) at growth pressures (~125 MPa). The pressure and temperature are maintained for three days to ensure that no leak forms from creep. TZM is highly resistant to creep, especially at lower temperatures, but the gasket may be made of a softer metal, such as Nb, which may not be as tolerant. And even though TZM is creep resistant, it is still advisable to monitor creep in the system. Periodic checks of the reactor body design described above indicate no creep (with strain measurable to around .0004) at average temperatures around 600-700°C and pressures around 100 MPa after nearly 2000 hours of operating time. The small variations in the diameter of the body may mask small creep, however, and thus periodic monitoring is highly recommended.

The final test before a reactor is officially commissioned for standard use is a chemistry test. Similar to the high temperature test, the chemistry test has the corrosive mineralizer added into the system. This test really ensures that the gasket is not only pressure ready, but that the

mineralizers do not cause additional swelling or corrosion that may induce leaks. The reactor is loaded as in the high temperature test but with mineralizer (in this case NH_4Cl) and then heated up for three days. Assurance that the mineralizer does not cause leaks is not strictly required if all reactor materials, including the gasket, are known to be inert or highly corrosion resistant. However, even mild corrosion can cause leaks if the material is not truly inert.

Although most of the chemicals used in a growth run are already present in the "final" test mentioned above, the true test of whether a reactor will function for growth is in the actual growth runs. The presence of whatever gallium transport species exist (which will be called Ga intermediates) may also alter the behavior of the gasket and reactor. Energy dispersive x-ray spectroscopy (EDX) of TZM components exposed to hundreds of hours at growth temperatures with Ga intermediates indicated no Ga absorption into the TZM, making reactor body-Ga intermediate interactions unlikely. The growth runs also are the initial steps toward understanding what temperature differentials and gradients are required to drive growth. The theory of growth and the physics of the growth event will be discussed in the next section of this chapter. But the reactor plays a very significant role in the physical environment. The baffles partially determine fluid flow by blocking some, but not all, mass transport between zones. They must prevent the development of an isothermal system between the growth and dissolution zones while still allowing significant mass transport to allow growth to occur. The thermal conductivity of the reactor wall and the thermal transport of the fluid (H_2, N_2, NH_3, and NH_4Cl) will determine the maximum sustainable temperature difference between zones. TZM has a very high thermal conductivity and thus it is expected that the temperature of the walls is very similar to the fluid at the walls. If TZM were a poor thermal conductor, the fluid could potentially cool the walls faster than heat could pass in, creating a significantly different

zone temperature than would be specified by external thermocouples. Internal thermocouples would certainly be advantageous, but the engineering required to realize this for the TZM reactor is difficult and has not yet been done. Heaters with power outputs of 300 W that are three inches tall were used. One can approximate the maximum temperature difference one could expect radially by using the steady-state heat equation $\vec{Q} = \kappa * A * \vec{\nabla}T$ where $\vec{Q}$ is the heat flow in, κ is the thermal conductivity of the reactor wall, A is the surface area, and $\vec{\nabla}T$ is the temperature gradient. This can be rearranged by considering only the radial direction in cylindrical coordinates and noting that the area is simply the circumference multiplied by the height of the reactor. It then simplifies to a scalar equation $\Delta T = \frac{Q*\ln\frac{r_o}{r_i}}{\kappa*2*\pi*h}$ where ΔT is the temperature difference between the outer and inner reactor walls, r_o is the outer wall radius, r_i is the inner wall radius, h is the height, and the other variables are as stated before. With $\frac{r_o}{r_i} = \frac{16}{7}$ and a thermal conductivity of 120 W/m*K, the largest ΔT one would expect is 4°C. This, of course, is an oversimplification, but it should give a somewhat reasonable estimate as a maximum wall temperature difference.

One drawback of the TZM reactor is heat loss. This can be accommodated by using robust insulation and powerful heaters, but it must be considered when designing the heating infrastructure for the reactor. Many reactor alloys such as the Ni superalloys have thermal conductivities of 10-20 W/m*K.[182,183] TZM has a thermal conductivity nearly an order of magnitude higher and thus will suffer significantly higher heat loss. In the design that eventually came to be used, the head assembly (the top portion of the reactor that seals to the body) was party stainless steel and thus needed to be kept cooler to avoid both corrosion as well as softening of the metal (see Figure 18 below). Forced convection using simple mounted

equipment fans served to cool these components and a significant section of unused internal reactor volume was kept to create a smaller temperature gradient. The fluid within will also carry significant heat and so four baffles with tight tolerances to the reactor walls were placed. The open area of the bore was reduced to 10% at the baffles and the series of four baffles together appeared to dramatically reduce fluid flow from the growth and dissolution zones to the head assembly. This was concluded by the lack of any GaN deposition in the head assembly during the runs in spite of an external temperature of less than 300°C.

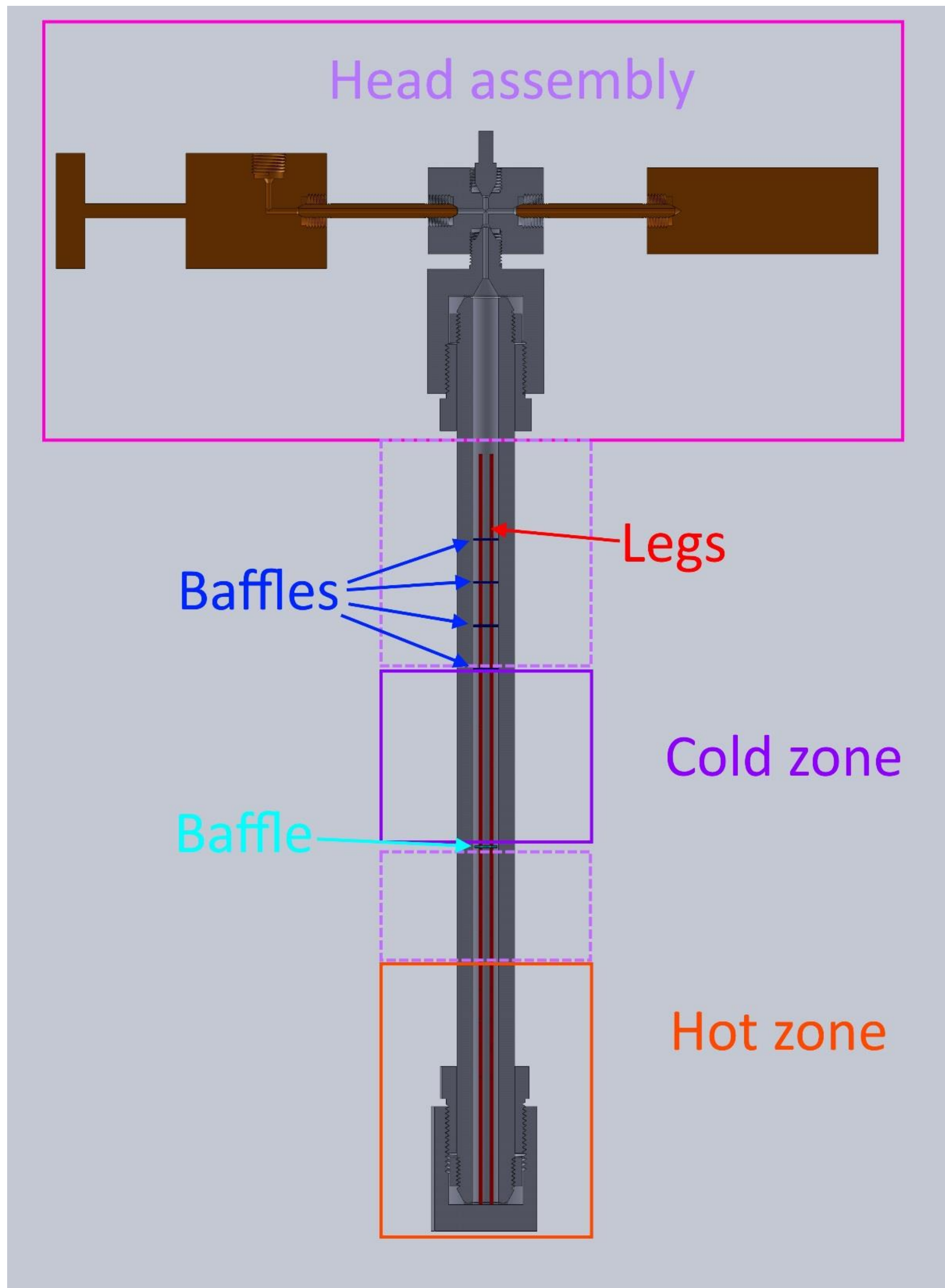

Figure 18. Schematic of TZM reactor used to grow GaN with NH_4Cl. The top baffles are used to separate the cold zone from the head assembly and the bottom baffle is used to separate the hot and cold zones. The brown components are the valve (left) and the pressure transducer (right) and are made of stainless steel. Dashed regions indicate where insulation is present outside the reactor.

The brittle nature of TZM also requires a certain level of care to protect the reactor from damage due to sharp impact, such as collision with a corner. Although TZM has a high yield strength, its low fracture toughness necessitated the design of certain infrastructure to prevent flaws that may act as crack initiation points. The plates that the reactor interfaces with in its stands are generally aluminum due to the low elastic modulus. Steel is used where temperature prevents the use of aluminum, specifically the heated stand where growth occurs. For transport when the reactor is loaded with NH_3 and other chemicals, protective aluminum plates were also fabricated. These plates are each ¼ of an inch thick and encompass the body by clamping to the head and base using steel ½-13 bolts. This prevents accidental damage to the reactor body by giving another mechanism to absorb impact energy. However, this mechanism was not rigorously tested. Aluminum and steel can also be used in cryogenic temperatures, which allows the protective plates to be used during the NH_3 fill rather than being placed afterwards.

The above outlined procedures and protective infrastructure are highly important but one of the most important features is the use of a secondary containment vessel. This infrastructure was adapted from use with Ni alloy reactors using basic mineralizers, but the function of the secondary containment is the same. The containment vessel (CV) serves as a hermetic barrier to shield the lab from shrapnel, in the case of a catastrophic failure, as well as containing any leaking NH_3. The TZM reactors have not yet suffered any catastrophic failures and in no case has a shrapnel producing event occurred, but often the reactors have leaked potentially hazardous NH_3. The CVs were essential in protecting the lab occupants as they allow the leaking gases to be safely exhausted without ever contacting the breathable air in the lab. And while the CVs acted only to protect the lab occupants for the Ni reactors, TZM has a high propensity to oxidize in the form of MoO_3, which is volatile above 400°C.[176] Thus, the CV

also protects the TZM from oxidation by creating an environment where there is no oxygen. As part of the growth process, the CV is pumped out and filled with N_2 gas.

B. The Theory of Solvothermal Growth

"Only I must observe that the vulgar conceive those quantities under no other notions but from the relation they bear to sensible objects. And thence arise certain prejudices, for the removing of which, it will be convenient to distinguish them into absolute and relative, true and apparent, mathematical and common."
–Sir Isaac Newton, *The Mathematical Principles of Natural Philosophy*

Solvothermal growth is a very useful and common technique for growth of crystals that are difficult to obtain from a melt. Several reasons may exist for the difficulty in producing a melt such as decomposition of the compound or excessively high temperatures to produce the melt. GaN actually suffers from both of these problems as the pressure and temperature to form a melt while also preventing decomposition are as high as 12 GPa and 2000°C.[184] The extreme conditions make large scale formation of GaN crystals unfeasible for economic and safety reasons. Solvothermal growth allows the transport of material and recrystallization at significantly lower pressures and temperature by creating an intermediate species (sometimes simply a solvated molecule of the compound and sometimes a chemical complex).

The simplest setup for a solvothermal system is a chamber with two zones that are separated by a volume. Each chamber is defined by walls with a given temperature which will provide the power to determine the temperature of the zone and each zone will have a temperature distinct from the other. In one zone, the dissolution zone, feedstock of the crystal compound of interest will dissolve. In the dissolution zone, the solubility of the compound will be higher than the crystallization zone. The crystallization zone will have a seed crystal upon which the supersaturated solution can deposit the excess material. Fluid will transport between zones, where fluid from the dissolution zone will become supersaturated by changing

temperature and then approaching saturation by depositing excess material onto the seed. The saturated fluid can then return to the dissolution zone and change temperature, becoming undersaturated. Dissolution of the feedstock then occurs and the fluid becomes saturated again. The fluid then returns to the crystallization zone where the temperature change again makes the fluid supersaturated, restarting the process. This process can occur as long as the temperature difference is maintained and both seed and source exist.

Solvothermal growth is usually assumed to be occurring close to thermal equilibrium. The system can never reach equilibrium if growth is occurring, otherwise growth and mass transport would not occur. However, if the mass transport from one zone to the other is slow and the kinetics of attachment of Ga and N are fast enough then a near equilibrium condition will occur where there is a small chemical potential gradient from the fluid to the crystal. The larger the chemical potential gradient, the farther from equilibrium the growth. If the growth kinetics are too slow, a steep chemical potential gradient will occur near the surface of the crystal. Similarly, if mass transport is very rapid then the growth kinetics will not keep up and again a steep chemical potential gradient will form. These two scenarios are actually the same, as "fast" and "slow" are terms relating the growth kinetics to the mass transport between zones. The kinetics and mass transport may also have different functions of temperature. Although neither have been directly measured, the kinetic factor of chemical reactions (here the breakdown of the Ga intermediates into GaN) tends to be Arrhenius with the form $k = Ae^{-Q/k_B T}$, where k is the kinetic factor, A is a prefactor, Q is the energy barrier of the reaction, k_B is Boltzmann's constant, and T is the absolute temperature. Mass transport between zones is far more complicated, but it can be stated that mass transport will be dominated by convection and thus be a function of the temperature difference between zones as long as the

thermal expansion coefficient of the fluid is nearly constant. With passive reactor designs, like the one used in this research, only buoyancy effects are used to mix the fluid. Thus, the mass flow between zones is a convoluted function of the temperature difference between zones as well as solubility and viscosity, both of which also have a temperature dependence. Simulation of the ammonothermal environment using computational methods is an ongoing research topic, but the physical parameters of the fluid are still not well known at the appropriate conditions and extrapolations of known data are used instead.[185]

Growth Far From Equilibrium

Many different techniques exist as methods of growth far from equilibrium. The better known epitaxial methods, including metal organic chemical vapor deposition (MOCVD), molecular beam epitaxy (MBE), and sputtering are occurring far from equilibrium.[186] Although there are some advantages to these growth methods, such as precise control of film thickness, the far from equilibrium growth also has some drawbacks. By definition, far from equilibrium means that there is a large chemical potential gradient present that drives growth. This large chemical potential gradient allows the defects to more readily form, as defects require some energy to form. If the chemical potential gradient is very small, defects are very unlikely to form because there is a positive chemical potential change going from the intermediate to the defect state. One can think of this as a three level system: the chemical potential of the intermediate, the chemical potential of a defect state, and the chemical potential of the perfect crystal. The driving force for growth is always the difference between the chemical potential of the intermediate state and the perfect crystal. If there is a large difference, the defect state may also have a lower chemical potential than the intermediate state (and thus a lower energy) and therefore both the perfect crystal and the defect state may

form. If the driving force is small, the defect state may have a higher chemical potential than the intermediate state, thus only the perfect state has a lower energy and can form.

Mass transport of far from equilibrium growth methods tend to be in gaseous states, as one would expect spurious reactions to occur with unstable molecules in more dense media. The chemical reactions are therefore designed to occur at a surface when the unstable molecules impinge. Often, the surface of interest (the substrate) is heated to cause rapid decomposition of the molecule as well as preferential deposition. Substrate temperatures in MOCVD can be greater than 1000°C while the input gases are close to room temperature.[186]

Growth Near Equilibrium

As mentioned in the prior section, growth near equilibrium has the advantage of having a reduced rate of defect formation. This, of course, does not preclude defects. However, highly perfect crystals can be grown near equilibrium to very large size. Near equilibrium growth generally means that a small supersaturation exists, meaning only a small fraction of material will be deposited from the transport media. So to increase growth rate, it is desirable to have a dense media. Near equilibrium growth should then occur in liquids or supercritical fluids.

The thermodynamics of near equilibrium growth can be approximated by assuming each zone is actually in thermal equilibrium and the intermediates do not decompose until they reached the seed surface. If this is true and we assume that one enthalpy and entropy change govern the intermediates, $\Delta G(T) = \Delta H - T\Delta S$, where $\Delta G(T)$ is the chemical driving force or Gibbs free energy of the reaction going from the intermediate to GaN, ΔH is the enthalpy of the reaction, T is the absolute temperature, and ΔS is the entropy change. Note that here we are using $\Delta\mu$ and ΔG interchangeably. We can also recall from statistical mechanics that the true free energy is modified by the activity of reactants and products, thus we can have a ΔG^0

at saturation and upon supersaturation it is modified with the form $\Delta G(T) = \Delta G^0 + RT_g ln\left(\frac{c_g\gamma_g}{c_d\gamma_d}\right)$, where c_g and c_d are the equilibrium concentrations at the growth and dissolution temperatures, respectively, and γ_g and γ_d are the activity coefficients of the intermediate at the growth and dissolution temperatures. If the reference state is GaN itself, then $\Delta G^0 = 0$ (this implies that if $c_g\gamma_g$ and $c_d\gamma_d$ are equal then there is no driving force for growth). Only the logarithmic term remains. If a singular ΔG governs the reaction, then $c\gamma = e^{-\Delta G/RT}$ regardless of the temperature so the driving force can be simplified to $RT_g * \left(-\frac{\Delta H - T_g\Delta S}{RT_g} + \frac{\Delta H - T_d\Delta S}{RT_d}\right) = \Delta H\frac{T_d - T_g}{T_d} = \Delta H\frac{\Delta T}{T_d}$. This indicates that even with a fixed temperature difference between zones, the chemical driving force for growth decreases with increasing temperature.

Unfortunately, no consensus exists on the solubility of GaN in the ammonothermal environment. The chlorides are plagued with a lack of reproducibility. Three significant studies have been published and each differs by between a factor of five and forty near 600°C.[124,126,127] The research outlined below has some circumstantial data indicating that the solubility is actually very high, but no careful study of solubility was conducted. A careful study of solubility and its temperature dependence would allow the calculation of ΔG and thus be useful in determining the chemical driving force for growth during a run.

C. Ammonothermal Growth of GaN in a TZM Reactor Using NH_4Cl Mineralizer

"Give me a place to stand, and I can move the earth."
-Archimedes

The main thrust of this research was to enable acidic ammonothermal growth of GaN at UCSB. The obvious conclusion to this is a new research initiative of acidic growth to further

understand ammonothermal growth in general. After the successful development of the TZM reactor, NH_4Cl mineralizer was added to the NH_3 fluid to enable transport of GaN. Initial tests were at relatively high temperatures with cold temperatures of 575°-600°C and hot temperatures of 600-650°C. Dissolution of GaN was obvious, and high NH_4Cl masses were used (from 0.6-0.9 g). However, under the assumption of normal solubility, seeds were continually etched. There were several possibilities for such a result due to a lack of data. Inconclusive solubility data means that the seeds may etch and then grow slowly, leading to effective etching. Unfortunately, in situ monitoring has not been developed making this difficult to directly measure. The other possibility, which was eventually realized, is that the system in this temperature regime exhibits retrograde solubility.

Although the system was tested for retrograde solubility, it took several months to realize the error. The reactor always leaked upon cooling due to the thermal expansion mismatch of the gasket and gland with the reactor body. Small GaN crystallites were found around a TZM plug that was used to adjust the height of the reactor furniture (the stands for the seeds, baffles and source material). The leak always occurred through the hot zone gasket, and the presumption was that the NH_3 rapidly supersaturated at that zone and precipitated the GaN. However, upon removal of the standoff and another growth run with the seed in the hot zone and the source in the cold zone, growth was confirmed. The plug was acting to reduce fluid flow around the reactor walls, creating an artificially hot region. The rest of the fluid in the hot zone could mix with fluid from the cold zone. The high temperature fluid acted as a sink for incoming GaN, thus masking the nature of the solubility. Figure 19 shows the hot zone after a run. Literature supports this conclusion, but higher temperatures with growth occurring at 700-720°C and dissolution occurring at 650-700°C.[128] Based on the temperatures where

growth was performed under normal and retrograde solubility, the likely changeover temperature is somewhere between 600°C and 650°C.

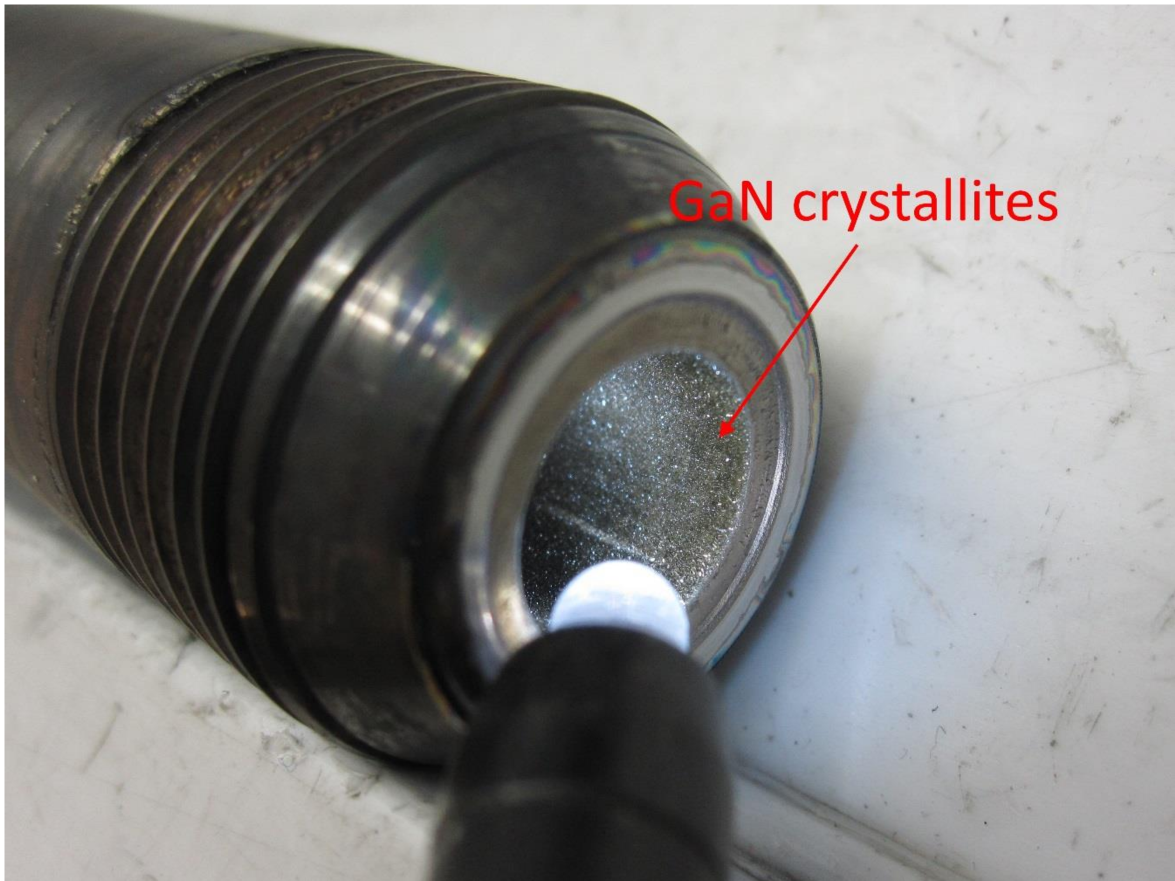

Figure 19. Hot zone after a growth run. T_{cold} = 500°C, T_{hot} = 650°C, P~100 MPa.

Polycrystalline GaN and Heteronucleation

The general goal of bulk crystal growth is the synthesis of large, perfect crystals. However, even seeded growth often has parasitic polycrystalline growth on non-seed surfaces, such as reactor walls or furniture. Such growth can give clues as to what is happening in the growth environment. The roughness of a wall, for example, can result in many nucleation sites and cause massive parasitic nucleation. However, if the chemical driving force is small enough then no nucleation will occur because the formation of nuclei will have an associated energy

cost. A significant portion of this energy cost can come from the solid-solid interface of GaN on reactor wall. Thus, the extent of wall nucleation can indicate where large chemical driving forces for growth exist. The continuation of a GaN crystal has no such nucleation energy cost because the same surface is created when material is deposited. Thus, even very small chemical driving forces can induce growth, although the growth will likely be slow as well.

Growth run	Growth temperature (°C)	Dissolution temperature (°C)	NH_4Cl (g)	Parasitic polyGaN (g)	Growth rate (µm/day)
160415I	650	500	.625	.14	24
160517I	650	500	.638	.06	19
160604I	700	650	.638	.50	60
160614I	750	697	.640	.58	82
160630I	700	650	.205	.49	57
160707I	700	675	.206	.70	99
160714I	700	650	.640	.09	30

Table 1. Growth summary of seeded growths in TZM reactor using NH_4Cl mineralizer. Red indicates the reactor leaked. Orange indicates a different reactor body was used for growth.

All growth runs with GaN source material exhibited polycrystalline GaN (polyGaN) deposition on the walls. This is not entirely unexpected, as temperature differences of 25°C or greater were used. However, nearly all of these runs also had polyGaN on the walls already. It would be advisable to prevent parasitic nucleation in some manner and in most cases 0.25-0.5 g of GaN were removed from the walls after the run (although this was not all that was present). As the surface area of the polyGaN gets larger, it will more quickly deplete the solution of supersaturated GaN. Large quantities of polyGaN growth have occurred, though this is likely more akin to seeded growth once nuclei are established. Although smaller

depositions of around 10-20 mg have occurred on the reactor walls, as much as 700 mg has been deposited over a 4 day stretch.Table 1 shows the correlation of seeded growth rate, temperature, and parasitic polyGaN growth. The masses of polyGaN growth were calculated by measuring the mass change of the reactor body.

GaN deposition is a very important phenomena to track for growth, but other compounds present can also yield useful information. EDX of powder deposition in the head assembly of the reactor indicated a type of $GaCl_x$ present. The measured ratios indicated $GaCl_{2.4}$, but this could be a mix of GaCl and $GaCl_3$. There is no strong consensus as to the form of the Ga intermediates, but Zhang et al. has proposed the formation of an ammoniated gallium chloride cation $[Ga(NH_3)_5Cl]^{2+}$ with counterbalancing Cl^- ions.[187] Figure 20 shows the white powder from run 150627I which initially indicated a $GaCl_x$ compound. However, no N was detected. This may be due to NH_3 being a relatively weakly bonding ligand and evaporation occurring during evacuation of the chamber, but this cannot be said with certainty.

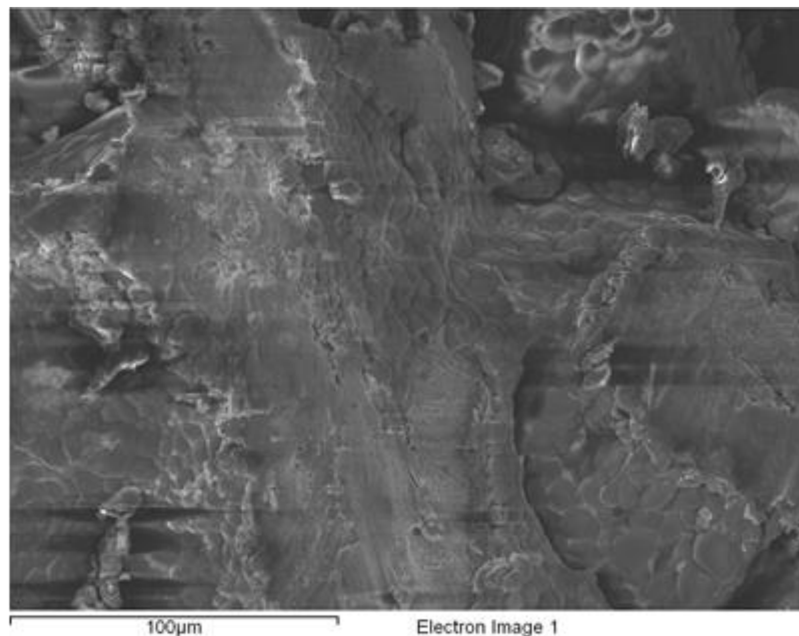

Figure 20. Scanning electron micrograph of white powder collected from the head assembly of a growth run. Ga and Cl atomic concentrations were measured at 29% and 71%, respectively.

The necessity of preventing oxygen contamination appears quite dramatically when EDX data from early growth attempts are examined. Very high oxygen concentrations are found such that the deposited material is really gallium oxide rather than gallium nitride. This explains why the mass was not a continuation of the crystal but was rather deposited on the surface as show in Figure 21 below.

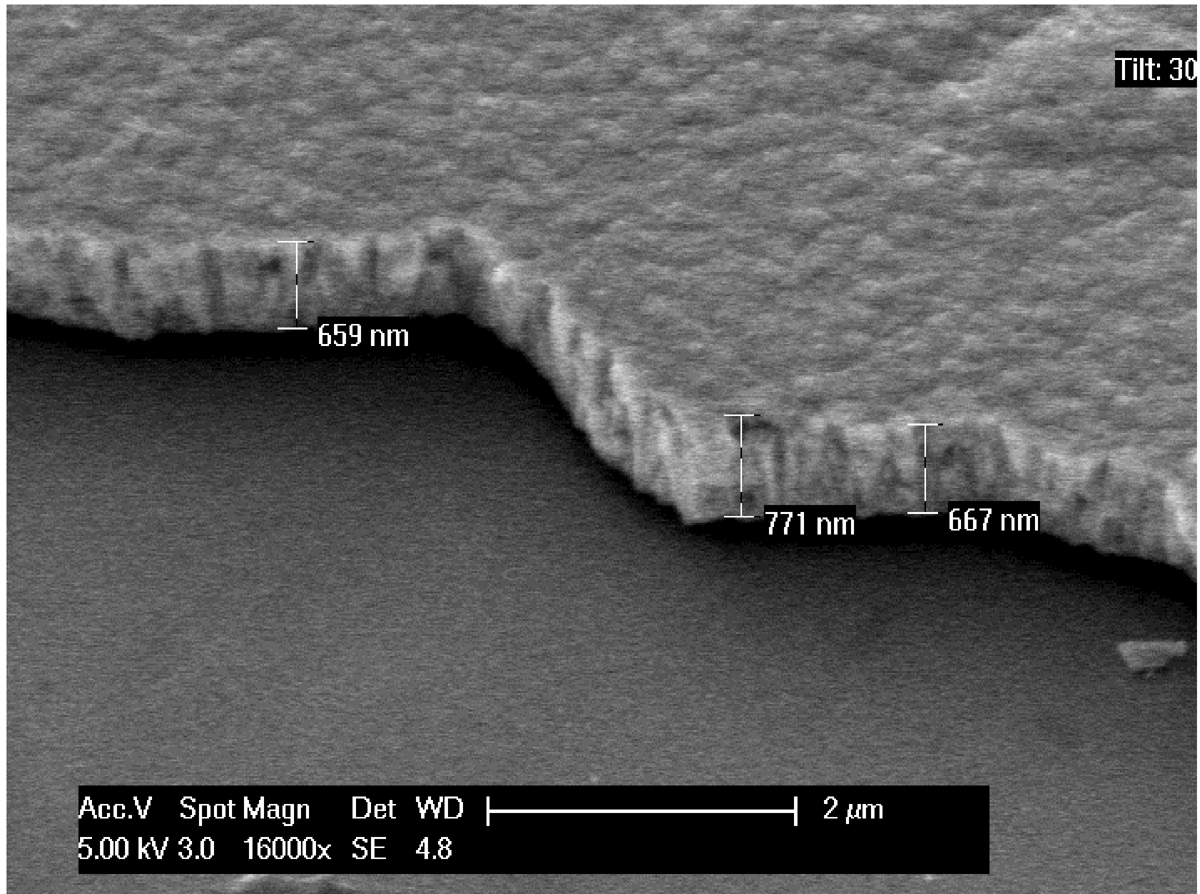

Figure 21. Gallium oxide mesa on a GaN template. The atomic composition as measured by EDX are as follows: Ga 31%, O 60%, N 8%, Cl 1%. The material was grown in normal solubility conditions with a hot zone at 535°C and a cold zone at 245°C.

The small lessons learned from the polyGaN growth and early experimental runs pave the way forward to develop seeded growth. But demonstration of seeded growth is paramount in order to truly prove the viability of the TZM reactor and the growth method. Unforeseen problems can potentially develop when trying to extrapolate from polycrystalline wall growth to seeded growth. The next section outlines the seeded growth experiments performed in the TZM reactor.

Methodology and Observations in Seeded Growth

Growth of GaN in the TZM reactor has been developed into a specific procedure that only requires modification of the seeds and furniture. The seeds were prepared by first drilling a hole in the center of the seed (which was used to hang the seed in the reactor) with a 0.75 mm diameter diamond drill bit. The seeds were clamped in an acrylic mount and the drill was manually aligned. The seeds were characterized using x-ray diffraction (XRD) as well as optical pictures, mass measurements, and thickness measurements at the corners of the seed. After the hole was drilled, the seeds were cleaned in acetone and isopropyl alcohol for three minutes each then weighed, pictures were taken, and thickness measurements were made. XRD measurements were then made, after which the seeds were cleaned again and stored in plastic sample containers until reactor loading.

The furniture design is meant to be adjustable but is generally kept the same once growth has been established. Four legs (rods with holes for wires to pass through) are connected to the baffles (discs with holes in them) by passing the legs through the holes. Other than the holes for the legs, the baffles have holes to allow fluid flow between regions. Small holes in the legs are present to allow a wire to feed through above and below each baffle to hold the baffle in place. Similar holes for wires exist in the hot and cold zones for wires that will hang the seed crystals and source material. An image of the full furniture setup (left) and zoomed in images of the source and seeds (right) are shown in Figure 22.

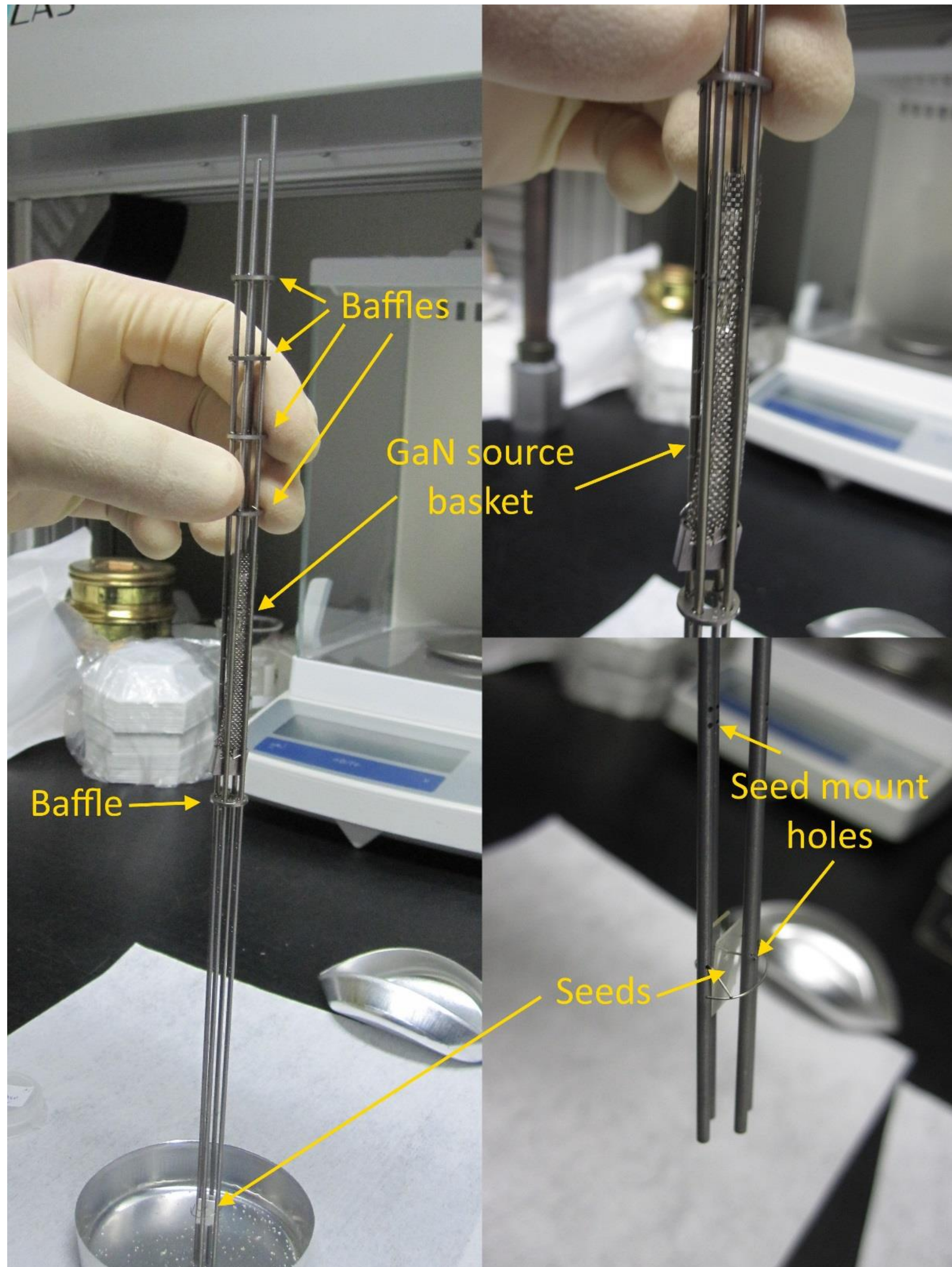

Figure 22. Furniture setup for a growth run. The GaN source and seeds are in position for retrograde solubility. Holes similar to the seed mount holes are present around each baffle. When wire is fed through these holes around the baffles, the baffle is locked in place. The top right and bottom right images show the GaN source and seed, respectively.

The reactor parts were all kept in vacuum ovens with the TZM parts stored at 80°C and stainless steel parts kept at 50°C. The vacuum ovens were used to prevent water adsorption to the surfaces. The effect of this storage was not directly measured, but it was found that TZM parts left out in ambient conditions without being cleaned (after machining) took on a blue coloration after several weeks that was water soluble. The exact origin of this blue substance was not verified, but it may be a molybdenum oxide that forms molybdenum blue.[188] The sealing surfaces of the reactor body (the sealing bead) were polished by hand using the lathe at the physics machine shop with 600 grit SiC sandpaper followed by 2000 grit SiC sandpaper. The inner surface of the head and base were polished using a custom one inch diameter aluminum rod with 600 grit SiC sandpaper attached to the end.

The following procedure was used to load a reactor for a growth run. First, the seed or seeds were prepared as described above. All reactor components were removed from their respective ovens and allowed to cool to room temperature. The reactor body was weighed and the sealing glands for all connections were lubricated with either a polytetrafluoroethene (PTFE) based lubricant or MoS_2 dry lubricant. The head assembly parts were connected and the reactor base was attached to the body using the appropriate torque (initially 140 ft-lbs with the Nb gasket and 1/16th radius sealing bead but this was reduced to 100 ft-lbs later and yielded consistent seals with properly polished surfaces; the torque was further reduced to 60 ft-lbs with the 1/32nd radius sealing bead with consistent seals). Head assembly connections were sealed with 16 ft-lbs of torque. The appropriate polyGaN was weighed out in the source basket and then the seeds and source basket were mounted into the furniture which was immediately loaded into the reactor body. The reactor body, a weighing tray and spatula (for measuring out NH_4Cl), the head assembly, two pairs of tweezers, and two gaskets (one extra in case the

first is scratched) were loaded into the N_2 glovebox. The appropriate mass of NH_4Cl was placed in the weighing tray. A reactor stand in the glovebox was used to tilt the reactor and allow the furniture to be partially pulled out so the NH_4Cl could be added to the bottom of the reactor. Tweezers were required to pull the furniture out as well as controllably lower it in. A torque wrench and a breaker bar with a crowfoot were used to partially seal the reactor in the glovebox. While the reactor was always removed from the glovebox and a final torque was applied to ensure sealing at high pressure, once the torque was reduced to 100 ft-lbs or below the torque was usually fully set in the glovebox. A custom stand was used to keep the flats of the head and base aligned such that the ¼ inch thick aluminum protective plates could be clamped tightly and relatively straight with respect to the reactor body. The reactor was then attached to a gas manifold where it was evacuated and held under vacuum for a minimum of fifteen minutes. The pressure was monitored to ensure less than 1 mbar change was detected as a leak check. The reactor was then cooled with liquid N_2 for four minutes before being filled with the appropriate amount of NH_3. Initial trials used only one fill of NH_3, but it was noted that the vapor pressure measured by the pressure transducer was low. Later runs included a step where the reactor was vented, allowing the original fill of NH_3 to be removed and then the reactor refilled with NH_3. The reactor was then allowed to warm up with a fan blowing air on it. Significant water and ice condensation on the reactor was observed which had to melt and evaporate before the reactor was reweighed and then loaded into the CV. The reactor was loaded and thermocouples to both monitor temperature as well as control the power going into the heaters were pressed against the reactor. Insulation was placed also (see Figure 18 earlier in this chapter for where insulation and heaters were placed). The CV was then sealed and pumped down to .02 MPa and refilled with N_2 gas. The pump and refill process

was repeated a total of three times before a purge of N_2 gas was continuously pushed through the CV at a rate of around 1 cubic foot per minute (CFM). This purge was to remove the oxygen from inside the CV in order to protect the reactor. The CV was allowed to purge overnight before the run was started. The runs had a ramp rate of 2°C/minute for the hot zone with the cold zone having the same ramp time (resulting in a lower ramp rate). The ramp was also paused for thirty minutes at a hot zone temperature of 400°C to partially saturate the fluid.

The unloading procedure is similar to the loading procedure but in reverse order. After the heater circuits have been manually switched off, the purge gas is stopped, the CV pressure is checked to ensure it is not pressurized with respect to the lab, and the exhaust gas detectors are monitored for a minimum of ten minutes. While purge gas is flowing, the NH_3 and H_2 detectors are less sensitive to the environment of the CV. Upon cooldown, the reactors leak (likely from thermal expansion mismatches in reactor components) and thus it must be verified that minimal concentrations of NH_3 gas are present. If the NH_3 detectors measure a concentration less than 75 ppm, the CV is considered safe to open. In all cases, full face respirators were used which had a safety factor of approximately ten (meaning 250 ppm in the environment would effectively reach the user at 25 ppm). The Occupational Safety and Health Administration has a general permissible exposure limit (PEL) of 50 ppm, which means with a respirator an individual can work safely in concentrations significantly highly than the detectors would be capable of measuring.[189] However, the highest NH_3 concentration measured after a growth run was 37 ppm. Once the CV is ready to be opened, a second NH_3 detector was used to verify the NH_3 concentration while maintaining an open exhaust port. A separate exhaust line was then attached to the reactor valve and the reactor was vented to exhaust to guarantee no pressure remained in the reactor. The reactor was then weighed as a

precaution in case gas could not escape because of a clog. It is worth noting that during this research, at no point has the TZM reactor ever had a clog that prevented exhausting of the gas. The reactor was then transported to a stand where the top seal was broken by loosening the head assembly gland and the head assembly was removed with the entire reactor inside a fumehood. Pictures were taken of the inside of the head assembly and occasionally some of the powder was collected for analysis. The white powder was mildly soluble in water, but it often took significant time to fully dissolve. Pure NH_4Cl powder appeared to dissolve much faster, suggesting that the Ga complexes present are also water soluble but dissolve much more slowly. All components were cleaned in an ultrasonic bath with water twice (3-5 minutes each time) after the powder was no longer visible. The components were then cleaned in isopropyl alcohol for 3-5 minutes and stored in their respective ovens. Seeds were cleaned in water, acetone, and then isopropyl alcohol for 3-5 minutes each. Contrary to what was seen in the Inconel 625 reactors, only white powder was ever observed in the TZM reactors. However, the stainless steel tubing leading to the pressure transducer and valves appeared to have $FeCl_3$, as black and sometimes green deposition was rinsed out with water. The dark color would be replaced with orange to orange-yellow solutions as the solution sat, which is consistent with $FeCl_3$.[168]

Characterization of the seeds was accomplished using several different methods, but the most technical methods include SIMS and XRD. SIMS uses an ion beam to mill away material of the sample, primarily an oxygen ion beam for positively charged species and a cesium ion beam for negatively charged species. The charged species are collected and the mass is measured using a mass spectrometer. With the use of substrates that are precisely ion implanted (such as have GaN implanted with Si to measure a relative sensitivity factor, the

ratio of a substrate ion such as ^{69}Ga or ^{83}GaN to the ion of interest), accurate concentrations of impurities can be measured. XRD is useful in measuring the crystal's structural quality. Defects in the crystal alter the diffracted peaks by changing the shape and intensity of reflected x-rays. Misalignment in the diffractometer itself can also cause peak broadening. However, defects can also broaden the reflected peak by slightly altering when the Bragg conditions are satisfied. The Bragg condition is met when $n\lambda = 2d \sin \theta$, where n is the order of the reflection (an integer), λ is the wavelength of the x-rays, d is the spacing of the planes responsible for the reflection, and θ is the angle between the plane and the detector. One can see that if there is a range of wavelengths used, then there will be a range of angles where a signal will be detected. This would be an example of instrument broadening. Modern XRD instruments are highly monochromatic and thus have little instrument broadening, but some may still be present. The reflected signal relies on the coherent orientation of atoms with respect to each other. Defects break this coherency, thus altering the reflection properties. The type of defect also determines which reflections are affected. For example, in GaN the $(000l)$ reflections are broadened by screw and mixed dislocations but not edge dislocations (screw dislocations are best thought of as a shift in atom positions such that if you trace radially around the dislocation line, one revolution will result in a displacement of one Burger's vector, edge dislocations are an inserted or missing plane of atoms). Edge and mixed dislocations affect reflections where the first or second indices of the reflection are non-zero.[190] However, there is a small but finite minimum width of any peak reflection, known as the Darwin width.[191] The ideal XRD reflection is then a Darwin width peak which may be further broadened by instrument broadening. For reference, the Darwin width for a GaN (0002) ω–scan is around 12 arcseconds.[192]

The facets were identified using the LEO stripes on the seeds (which have been specified to be in the a-plane) and then identifying the main m-plane which is perpendicular to both the LEO stripes and the c-plane. In all of the LEO seeds, this corresponded to one of the main edges of the seed. Optical micrographs of the seed facets were taken using an optical microscope and holding the seed with self-clamping tweezers such that the m-plane facet and the semipolar facet are collinear with the microscope line of sight. This creates a 2D image of the two planes as two intersecting lines such that imaging software can be used to measure the angle between the planes. The non-LEO seeds had no such reference and the seeds were assumed to facet into m-planes. The facets were then analyzed in the same way as the LEO seeds and the measured angles were consistent with semipolar planes of m-plane character and not planes of a-plane character.

Single Crystal Growth in a TZM Reactor Using NH_4Cl Mineralizer

The methods outlined in the previous section led to multiple successful growth attempts with a growth temperature range of 650-750°C and a dissolution temperature range of 500-700°C. All growths were performed under retrograde growth conditions. The baffle separating the two temperature zones had an open area of 30% while the baffles separating the cold zone from the head assembly had an open area of 10%. In general, the growth was transparent or translucent, although there was almost always some level of coloration ranging from a strong green color (similar to the work by Yoshida et al. with growth >700°C or the work of Mikawa et al. with a growth temperature range of 500-650°C), to a slight yellow or grayish color.[128,138] The quality of the growth is somewhat convoluted with the lack of data on an optimal design for the reactor itself. The fluid flow within the reactor is not well understood yet and thus the growth may be occurring at suboptimal positioning for temperature as well as mass flow.

Early seeds were grown by lateral epitaxial overgrowth (LEO) (also referred to as ELOG in Chapter 1) and were supplied by Mitsubishi Chemical Corporation (MCC) while the smooth seeds grown on later were supplied by Nanowin Corporation, with the exception of an m-plane seed supplied by MCC. All seeds were c-plane with the exception of the single m-plane seed. NH_4Cl powder was purchased from Alfa Aesar with a purity of 99.999% on a metals basis. The O concentration of the powder was not available, but it is assumed that H_2O and O_2 are present on the surface in high concentrations. PolyGaN was purchased from MCC and fine grains (<1 mm in diameter) were used. The furniture was made from 99.98% pure Mo rods from ESPI while the head assembly and base were made from TZM from Eagle Alloys Corporation. Two TZM reactor bodies were used, one was made by Plansee Corporation and one by Eagle Alloys Corporation. The valve (30-12HF4) and stainless steel tubing (60-HM4-2.75) were supplied by High Pressure Equipment Corporation and the pressure transducer (PX02S1-30K-G-10T) was supplied by Omegadyne Engineering Corporation. Each growth run designation is date encoded in the form of YYMMDDR, where Y is the year, M is the month, D, is the day, and R is the reactor. The date indicates the start of the growth run.

160415I

Growth run 160415I was the first highly successful growth run but had a rather high chemical driving force. While growth can be achieved with ΔT as low as 25°C (and likely even lower), here ΔT was 150°C with a growth temperature of 650°C and a dissolution temperature of 500°C. The NH_4Cl content was 0.625 g and the growth time was 96 hours. The run was still part of an experimental series to determine where the optimal position for a seed was, and thus two seeds were placed in the hot zone, A1 and A2. A1 was further from the cold

zone than A2 and exhibited net growth while A2 was significantly etched. XRD ω-rocking curves indicate similar crystal quality between the seed and grown material, although it should be noted that the beams were not necessarily aligned in the same way with respect to the crystal (see Figure 24). Because the LEO stripes break the symmetry of the c-plane, this may partially be the reason why the peak shapes are different. The full width at half maximum (FWHM) of the peak before and after are comparable, around 110 arcseconds. Optical images are shown for both A1 and A2 in Figure 23. Note that A1 has a highly rough surface. The surface roughening is suspected to be from the high chemical driving force coupled with a low surface mobility due to the lower growth temperature. The seed grew approximately 96 μm in the c-direction with a growth rate of 24 μm/day. Although this is a rather low growth rate, there is no reason to believe that this is optimal. In fact, it is assumed that by changing the seed position as well as the furniture in the reactor, growth rates more ten times greater can be achieved based on what has been accomplished by other groups. Another very discernable feature is the intense green coloration. This is similar to the coloration of the crystals grown by Yoshida et al. in 2014 and Mikawa et al. in 2015, which was attributed to oxygen related point defects.[128,138] A1 also picked up 14.38 mg of material, although it is rather evident from the optical images that significant material was lost along the edges of the sample perpendicular to the c-direction.

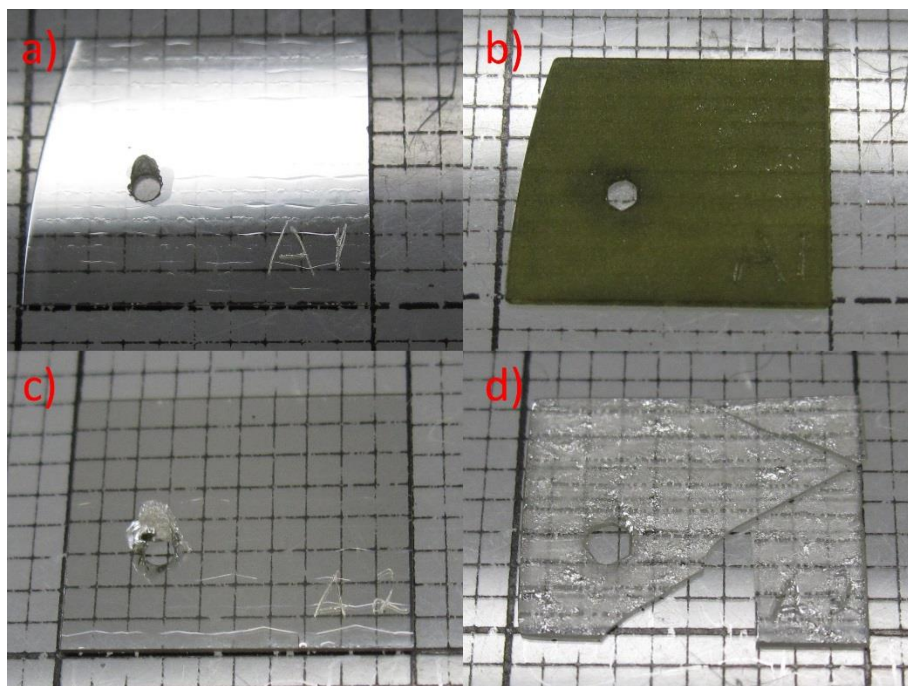

Figure 23. Images of 160415I A1 a) before and b) after and 160415I c) before and d) after growth. Each small square division is 1 mm on a side.

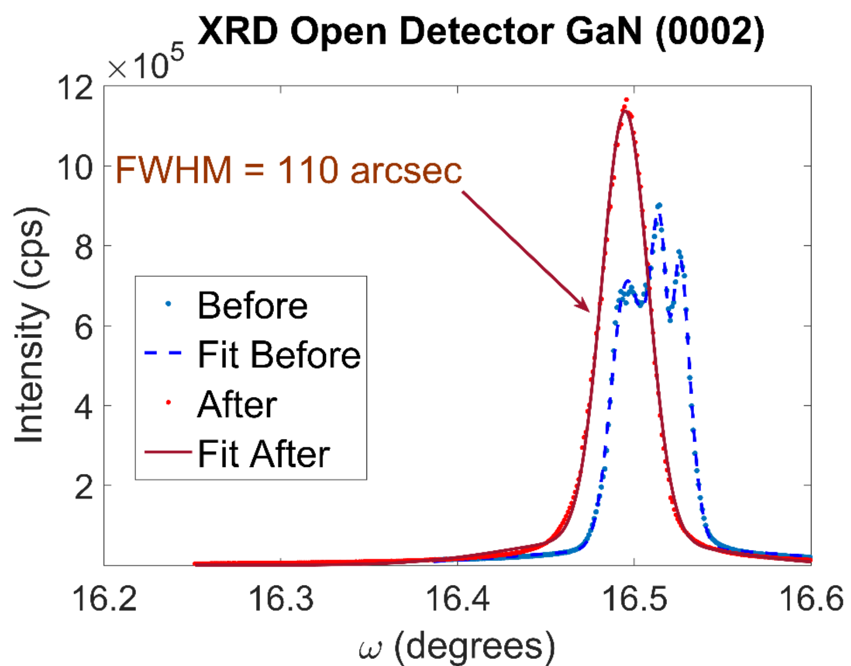

Figure 24. XRD of sample 160415I A1 before and after growth. Note that the peak does not significantly alter its FWHM, indicating that the quality of the seed is reproduced in the grown material.

160517I

The growth configuration for 160517I was rather unusual compared to other growth runs. This growth was an effort to more dramatically enforce isothermal zones in the reactor. From Figure 18, one can see that there will be a temperature gradient along the walls of the reactor in the hot zone because the insulated region (outside the reactor) is in contact with the walls inside the reactor connected to the fluid in the hot zone. Thus, as these walls cool the fluid in contact with the walls will also cool. A second baffle (40% open area) was placed at the height of the top of the hot zone heaters and both 160517I A1 and A2 were placed within the hot zone. Again, A2 was closer to the cold zone. The NH_4Cl mass was 0.638 g and the growth time was 96 hours. The temperature profile was as expected in this run with growth and dissolution temperatures of 650°C and 500°C but it was found that the power to the heaters was greater than what was expected based on two prior runs (for the top heater, runs with only the 30% open baffle had power outputs of 35%, this run had a power output of 38%). Although this is relatively circumstantial, it was also noted that the sum of the masses of both seeds along with the polyGaN deposition in the hot zone was constant before and after the run, which implies that the second baffle dramatically reduced mass transport between the hot and cold zone. The mass flow from the hot zone would heat the cold zone, thus reducing the power required by the cold zone heater to maintain the same temperature. In this case, the cold and hot temperatures were again 500°C and 650°C, respectively.

The transparency of the GaN grown was actually highly improved, suggesting that starting with low impurities in the source GaN can yield high purity growth (see Figure 25). The growth rate on the large faces of the seed (the c-plane) is also highly non-uniform, ranging from 16-26 μm/day. SIMS data is show in below, but an important note is that the O

concentration is around 4×10^{18} cm^{-3} (see). Although this is not reaching the level of semi-insulating GaN, it appears to be slightly lower than the O concentration of the GaN source material (~10^{19} cm^{-3}). Again, this is circumstantial, but it certainly warrants investigation of using high purity source material with these reactors and mineralizers. Of similar interest is the very low concentration of Mo and Ti, indicating that even if very small reactor corrosion is present, the reactor constituents do not incorporate into the GaN and thus do not poison the grown material. It should be noted, however, these elements in solution may still have the potential to alter growth rate. Similar to the prior growth, this run also appears to mimic the seed quality somewhat. Runs with more precise XRD alignment were done later, but the beam did not have a highly specific alignment with the LEO stripes on this seed, which may account for the increase in FWHM after growth. However, it is more reasonable to state that seed quality is possibly maintained but this is not guaranteed. The seed gained 11.95 mg of material and, as seen in the prior seed, slight etching is noted perpendicular to the c-direction. Faceting of the edges was noted and optical micrographs were used to measure the angles. The five facet to m-plane angles measured were 29.5°, 48.4°, 31.8°, 47.5°, and 29.8 with respect to m-plane and toward c-plane. These angles are consistent with the $\{10\bar{1}1\}$ planes at 28° from c-plane and $\{10\bar{1}2\}$ planes at 46.8° from c-plane.

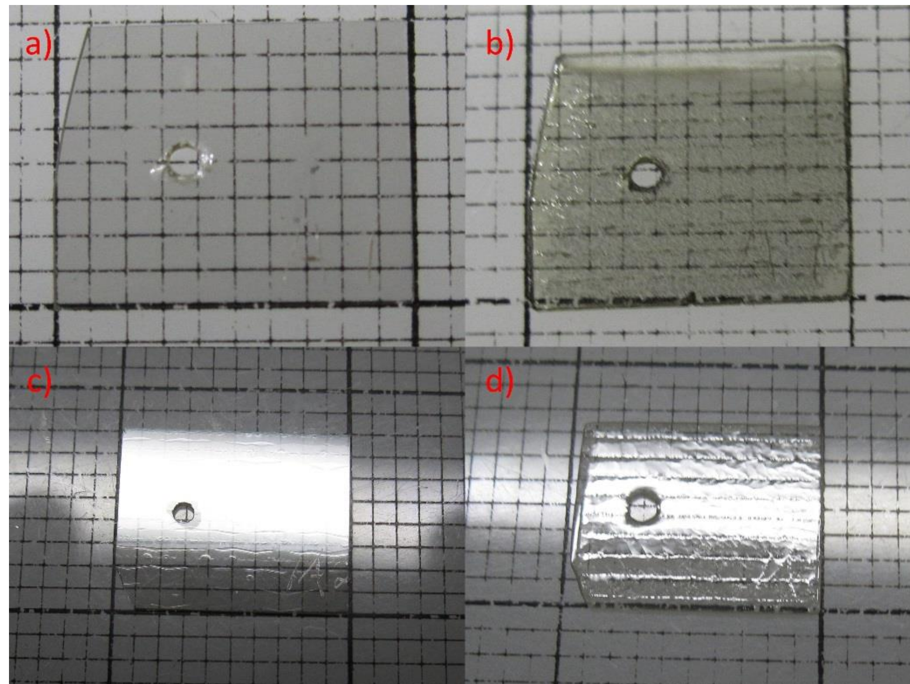

Figure 25. Optical images of 160517I A1 a) before growth and b) after growth as well as 160517I A2 c) before growth and d) after growth. Note the lack of coloration in the grown material on A1, although there is a slight gray tint, likely due to free carrier absorption. Panels c) and d) illustrate the etching that occurring, especially around the highly defective stripes from the LEO growth.

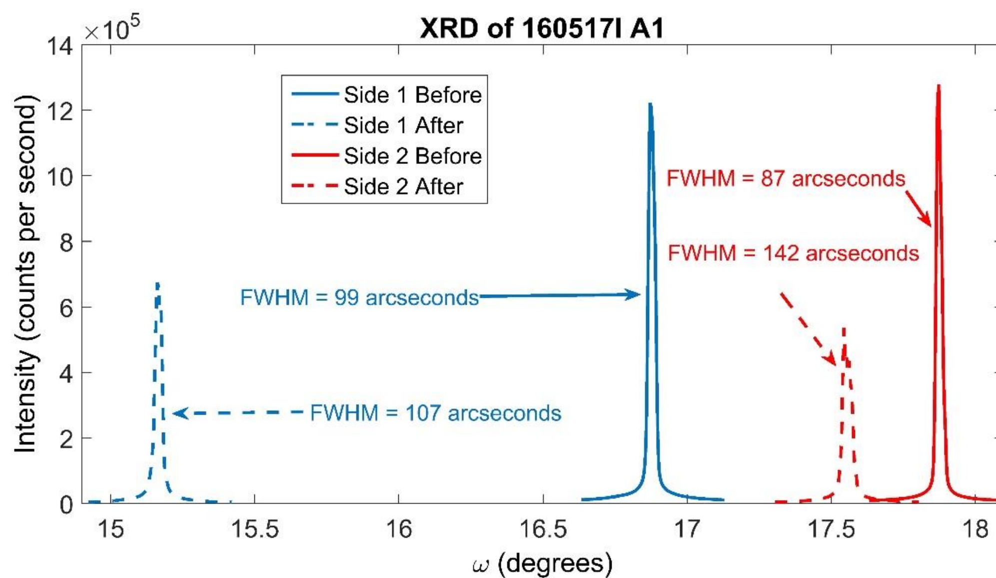

Figure 26. XRD data for sample 160517I A1. Note that for both sides, the grown material has a larger FWHM, which may indicate defect formation. However, the spread in where the peaks are centered also indicates that the beam direction is not the same for the before and after growth measurements. Due to the LEO stripes present, different

beam directions may have significantly different FWHM and even somewhat different peak shapes.

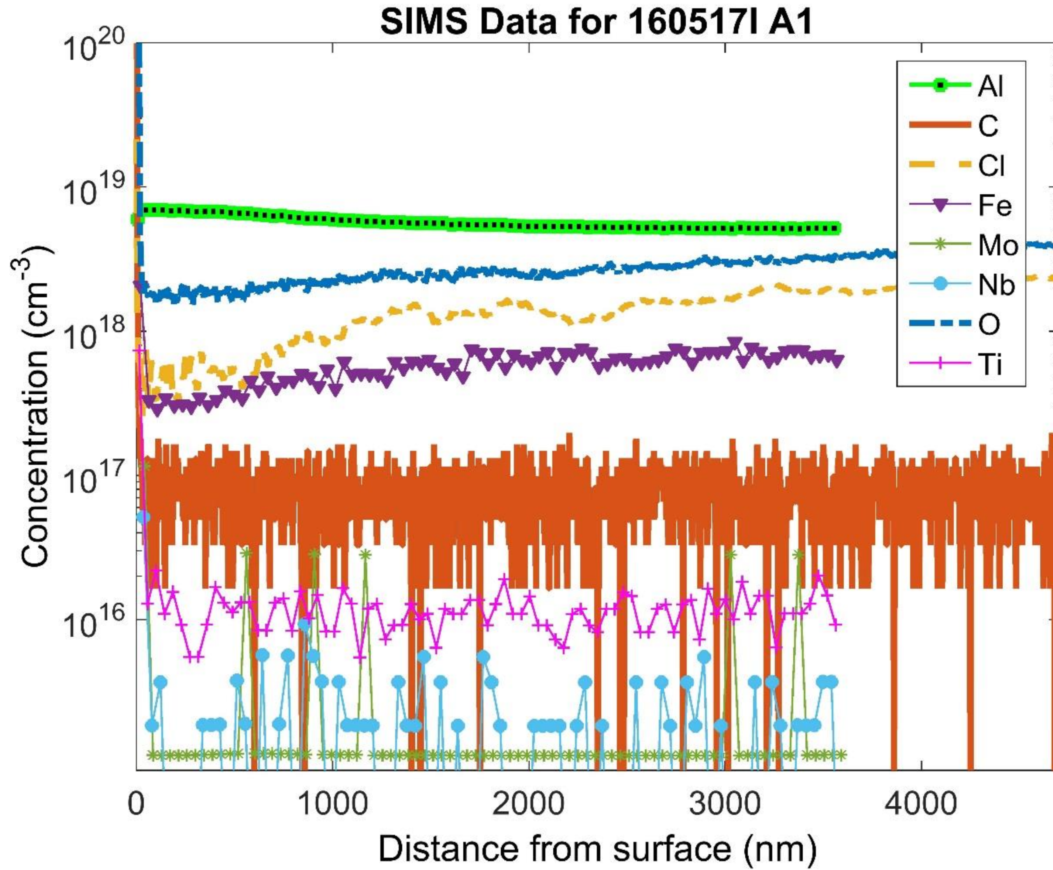

Figure 27. SIMS data for 160517I A1 after growth. C, O, and Cl (the data without symbols) was taken using a Ce gun. Al, Fe, Mo, Nb, and Ti (data with symbols and lines) was taken using an O gun. Note that the depths are estimates, as the seed surface wasn't completely planar and no depth measurement was made to determine the exact etch depth. The Al concentration is somewhat anomalous, as no reactor component has Al as an alloying element or common impurity. However, the Nb gaskets were polished on an Al block, and thus the Al concentration may come from the polishing method and therefore the gaskets.

160604I

Run 160604I had a single seed present and had a growth temperature of 700°C and a dissolution temperature of 650°C with 0.638 g of NH_4Cl. The growth time was 96 hours. The non-uniform growth on the surface became even more pronounced, with growth rates at the corners nearing a factor of 1.5 that of the growth rate at the center of the seed. However, one

can see from the optical images of the grown material that the transparency is largely maintained until the very edges of the seed. SIMS has not yet been performed, but one may speculate that the O concentration at the edges is significantly higher than at the center. If this were the case, then one could conclude that either the grown material is acting as an O getter or the higher chemical driving force enables higher O content. Until SIMS or some other elemental analysis is performed, this interpretation will remain speculative. However, it can be said that the seed edges also have a more significant green coloration than the seed center. This could also be from the material thickness difference, but in either case the coloration is far less noticeable than for 160415I A1.

Another important feature of the seed is the formation of new facets. This is found most readily at the corners of the seed (see Figure 28d). The angles between the LEO stripes on the seed (which are parallel to the a-plane) and the new facets is 30°, indicating that the new facets have m-plane character. Optical measurements of the angles of the new planes to c-plane indicate $\{10\bar{1}2\}$ planes, no $\{10\bar{1}1\}$ planes were observed. This is in agreement to the quasi-equilibrium crystal shapes determined by Bryant et al. which indicated that $\{10\bar{1}1\}$ planes develop with transient $\{10\bar{1}n\}$ planes where $n > 1$, although that work was done under HVPE conditions rather than ammonothermal conditions.[193]

Nucleation phenomena at the surfaces also appears to be highly important for subsequent growth. The use of a diamond scribe to mark the seed with A1 led to a deformed surface and what looks like possible faceting at the scribed area. Highly polished growth surfaces appeared to lend themselves to favorable growth while damaged or scratched surfaces (including the defective stripes) may lead to undesirable faceting at the surface (see Figure 28d).

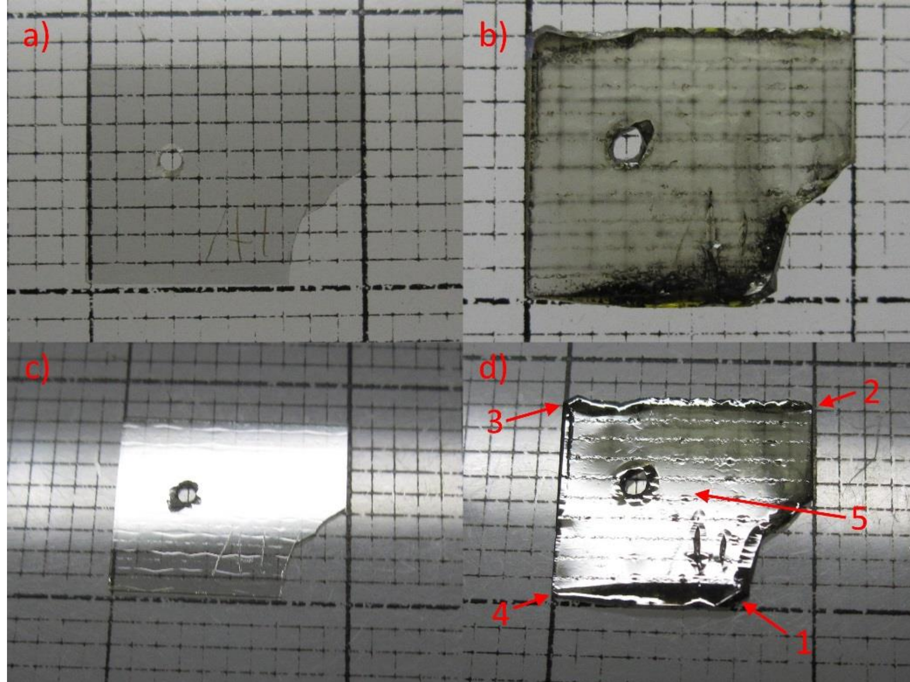

Figure 28. Optical images of 160604I A1. Images are taken normal to the c-plane a) before and b) after growth. Images inclined to the c-plane c) before and d) after growth. Growth rates measured at positions 1-5 are as follows: 1-175 µm/day, 2-97 µm/day, 3-136 µm/day, 4-148 µm/day, and 5-82 µm/day. Note the faceting at positions 1 and 3.

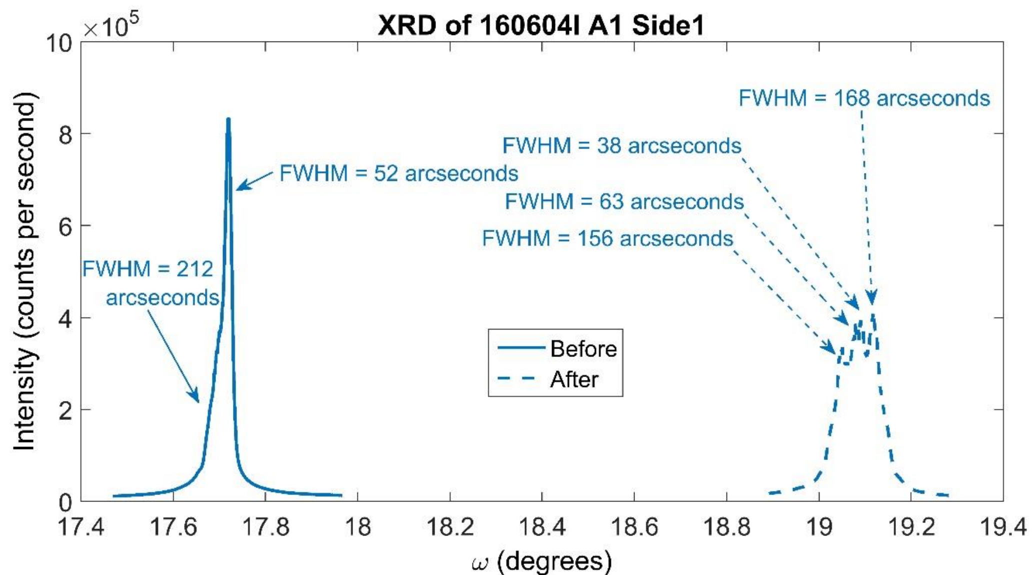

Figure 29. XRD ω-scan of 160604I A1. The large shift between peaks may be from slight misalignment of the sample on the XRD mount or a rotation with respect to the LEO grown material. It is interesting to note the increased separation of the peaks after growth. The distinct peaks indicate multiple grains are present and are illuminated by the x-ray beam.

160614I

Run 160614I had a single sample (A1) present during the run with a growth temperature of 750°C and a dissolution temperature of 697°C with 0.640 g of NH_4Cl. The growth suffered multiple leaks during its 96 day growth run, but it was allowed to continue as no leak was catastrophic. The pressure did drop significantly, however, and the average pressure of the growth was around 90 MPa. The growth appeared to behave similarly to prior growths at 700°C. Again, facets appear (see Figure 30d, position 1). The grown material appears to be more optically absorbing than prior growths as well. The fact that the absorption is broadband leading to a gray color (rather than green as seen in early growths) indicates that free carriers may be the cause. However, if a higher free carrier concentration is present then the reason for this is unknown. Several runs were attempted at these higher temperatures, but no run could be completed without leaks. All other runs attempted at this temperature profile suffered catastrophic leaks, venting all of the ammonia in the reactor within a few hours. The loss of material through the leak may be the cause for the degradation of the seed toward the right (see Figure 30). Post-run examination of the gasket in the hot zone indicated gas leaked through the hot zone, possibly due to softening of the gasket due to the high temperature.

Again, seed faceting is present but the $\{10\bar{1}4\}$ and $\{10\bar{1}5\}$ planes are present in addition to the $\{10\bar{1}2\}$ planes. The seeds also showed what appeared to be a second c-plane face that formed. The initial c-plane face also showed growth, but to a much smaller extent. It is possible that high chemical driving force at the edges initiated significant growth which propagated the semipolar facets, leading to the steps seen in Figure 30. It is interesting to note that the higher c-plane step surface is smoother than the growth in the sample center.

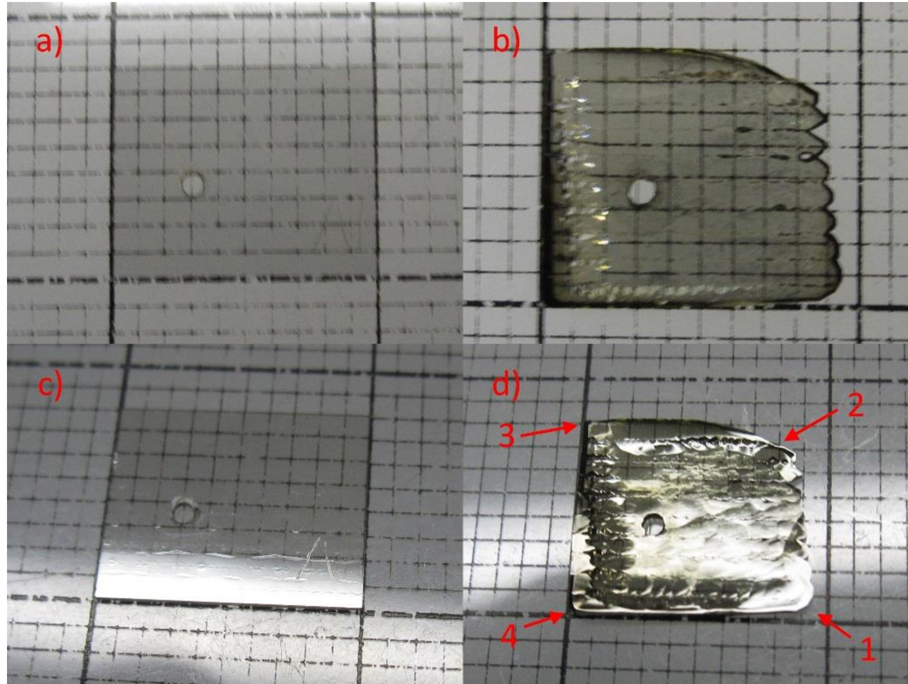

Figure 30. Optical images of 160614I A1 normal to the c-plane a) before and b) after growth and tilted from the c-plane c) before and d) after growth. Growth rates for positions 1-4 shown in d) are as follows: 1-48 µm/day, 2-32 µm/day, 3-145 µm/day, 4-96 µm/day. Note the step in d) around the edges of the sample and the smoother surface of the thicker step compared to the rounded surface in the sample center.

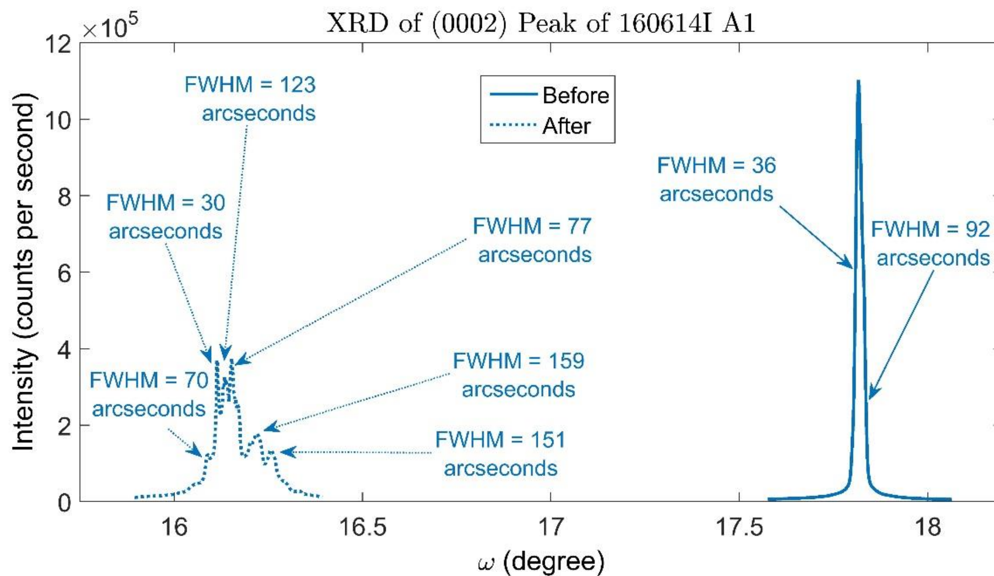

Figure 31. XRD data for 160614I A1 before and after growth. Note the large number of peaks that are present as seen in other samples after growth.

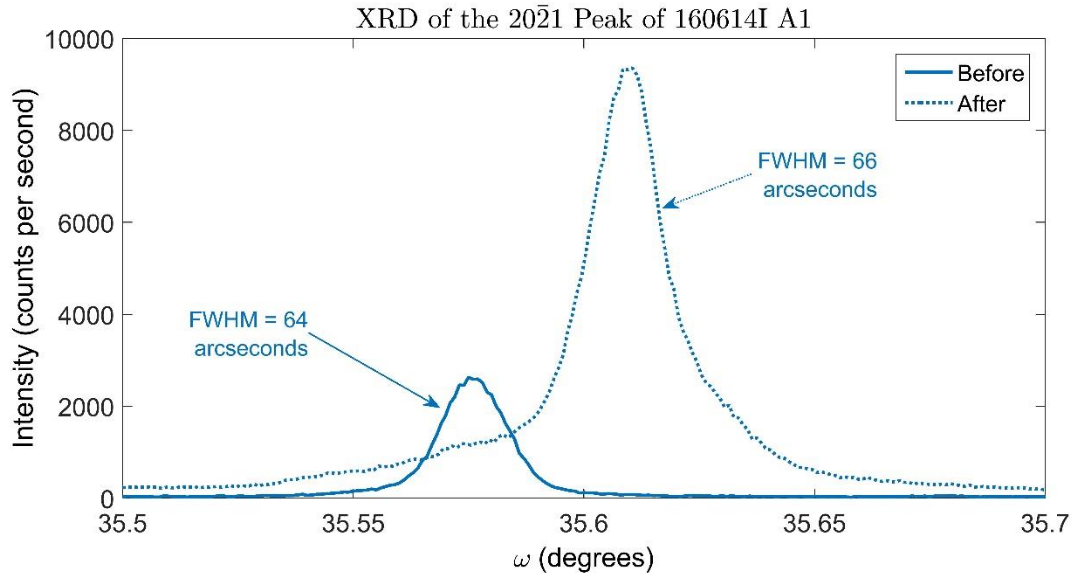

Figure 32. XRD data for $(20\bar{2}1)$ of 160614I A1. Note that the FWHM is essentially the same, but again a new peak appears to be present closer to where the original peak was.

160630I

Growth 160630I had a single sample present (A1) which was not a LEO c-plane seed but was a c-plane seed from Nanowin. The growth and dissolution temperatures were 700°C and 650°C, respectively. A smaller amount of NH_4Cl was used, 0.205 g, and the growth time was reduced to 48 hours. Unfortunately, the seed diagonal length exceeded that of the inner diameter of the reactor. As the seed was being removed from the reactor after growth it became wedged due to the polyGaN present on the walls. Attempts to remove it resulted in fracture of the seed. The lower NH_4Cl concentration appeared to have little effect on the growth rate normal to c-plane which indicated that mass transport of GaN was not the limiting factor for growth rate. Given the high polyGaN on the walls and the fact that it was not removed between each run, it seems entirely likely that the GaN on the walls removed a significant amount of GaN from the fluid.

The growth rates were measured at 57 μm/day at the center of the seed and 153 μm/day at the edges. The difference in thickness is clear from the optical images (see Figure 33). As seen with prior growths, there is little to no coloration near the center of the seed, but the edges have a yellowish color. This is indicative of possible C contamination, but it appears to be more likely that V_{Ga}-H complexes form, as discussed in The Ammonothermal Method in Chapter 1. The slight gray in the center of the seed is indicative of a relatively high free carrier concentration, although this was not measured. Facets of $\{10\bar{1}2\}$ and $\{10\bar{1}1\}$ planes were observed in this sample.

The XRD data indicated that the seed quality slightly deteriorated through growth. The FWHM increased for both (0002) and $(10\bar{1}1)$ peaks. However, the change appeared noticeable but not drastic.

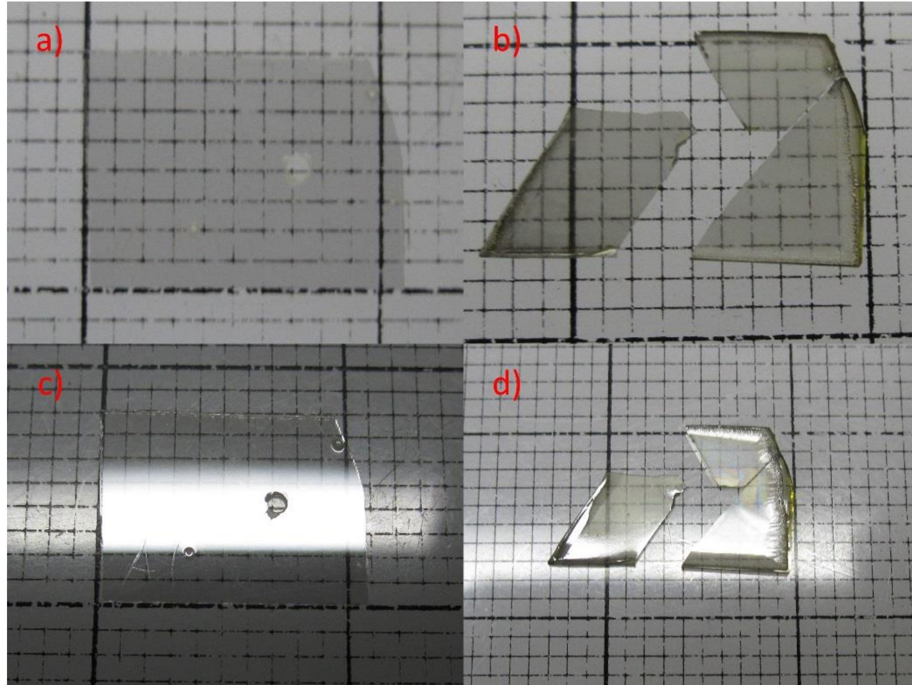

Figure 33. Optical images of 160630I A1 normal to the c-plane a) before and b) after growth and tilted with respect to the c-direction c) before and d) after growth. The seed fractured during removal from the reactor rather than before or during the run.

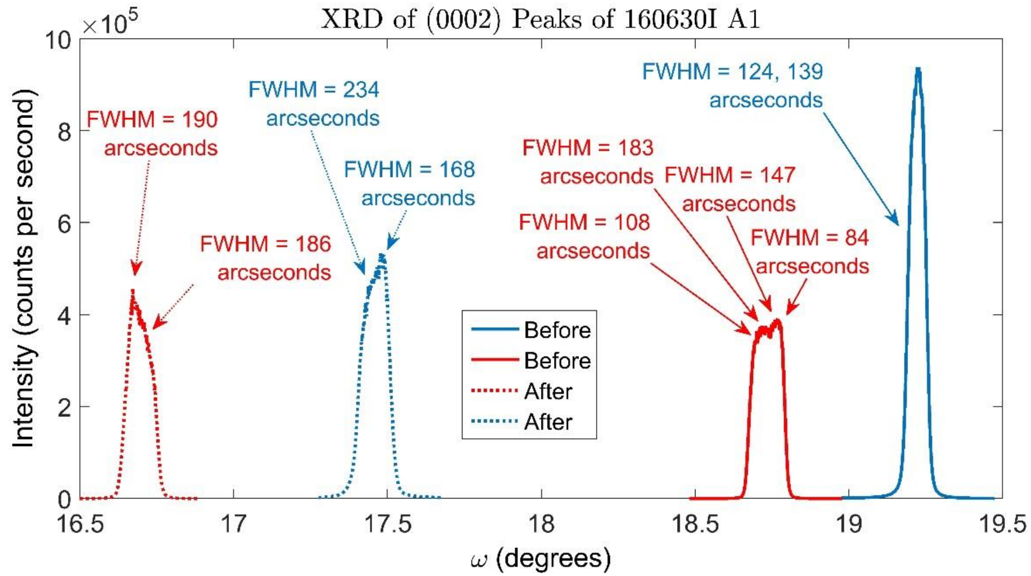

Figure 34. XRD of (0002) plane of 160630I A1. Due to the fracturing of the seed, the front and back side of the sample could not be distinguished. However, it can be seen that the red face before (at 18.72°) has essentially the same FWHM as both peaks after growth. The peak at 19.2° has two FWHM indicated because the fit was best for two Gaussian peaks centered at nearly the same coordinates with similar peak intensity but different FWHM.

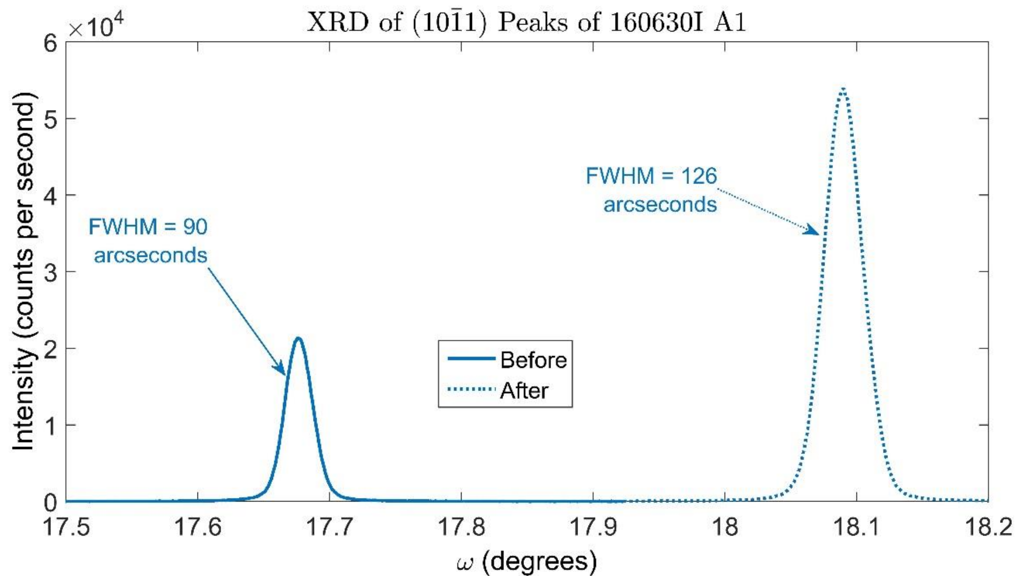

Figure 35. XRD of $(10\bar{1}1)$ plane of 160630I A1. The significant increase in the FWHM may be due to deterioration of the crystal quality.

160707I

Growth run 160707I was an exploratory run to determine the impact of chemical driving force on growth rate. The growth and dissolution temperatures were 700°C and 675°C, respectively, with 0.206 g of NH_4Cl. The minimum growth rate measured with a micrometer was 99 μm/day and the maximum growth rate was 191 μm/day with a growth time of 48 hours. Unfortunately, the sample suffered a similar fate to 160630I A1 and was broken during retrieval after growth. The seed was a high quality c-plane sample from Nanowin Corporation. As observed in earlier growths, a step was formed at the edge of the sample which appears smoother than the center of the sample. Also similar to the earlier growths was the slightly darkened edges, possibly from higher free carrier concentrations, with the center of the sample appearing rather clear. The yellow coloration appeared to be roughly the same as 160630I A1 or perhaps slightly less pronounced. Again, faceting was present at the edges of the sample. As was the case in 160630I A1, only the $\{10\bar{1}2\}$ planes were present.

The crystal quality in the grown material appears to be rather high, although a secondary peak was present with a slightly larger FWHM than the initial peak. Although this doesn't imply superior crystal quality to the initial seed, it is reasonable to deduce that seed quality can also be maintained at low chemical driving force. The change of the seed to grown material appears more favorable with the lower driving force, but such a conclusion would be hasty given this singular data point.

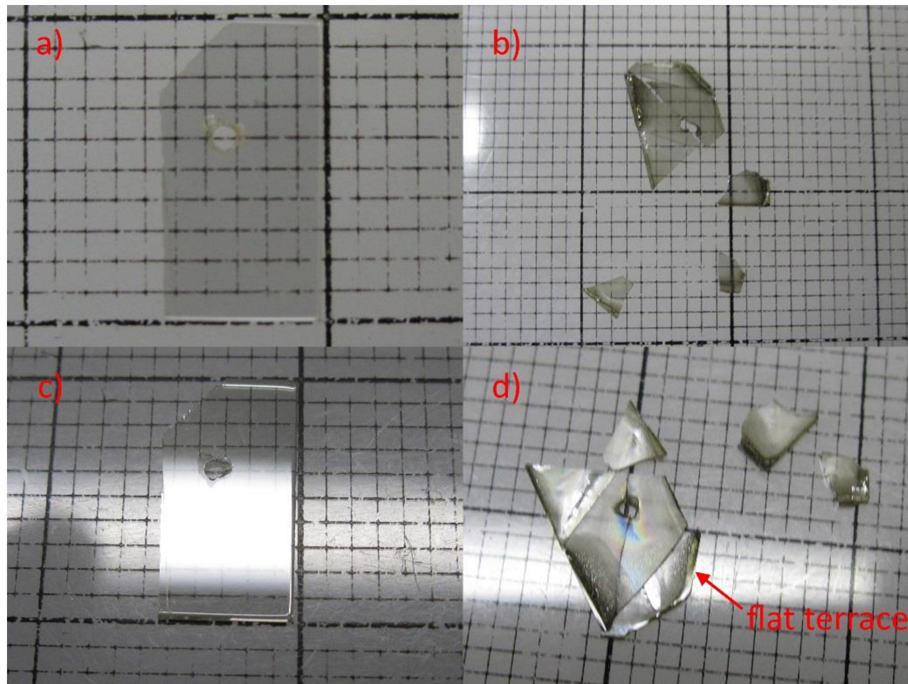

Figure 36. Optical images of 160707I A1 normal to the c-plane a) before and b) after growth and tilted from the c-direction c) before and d) after growth. Note the step formed in panel d, similar to prior growths.

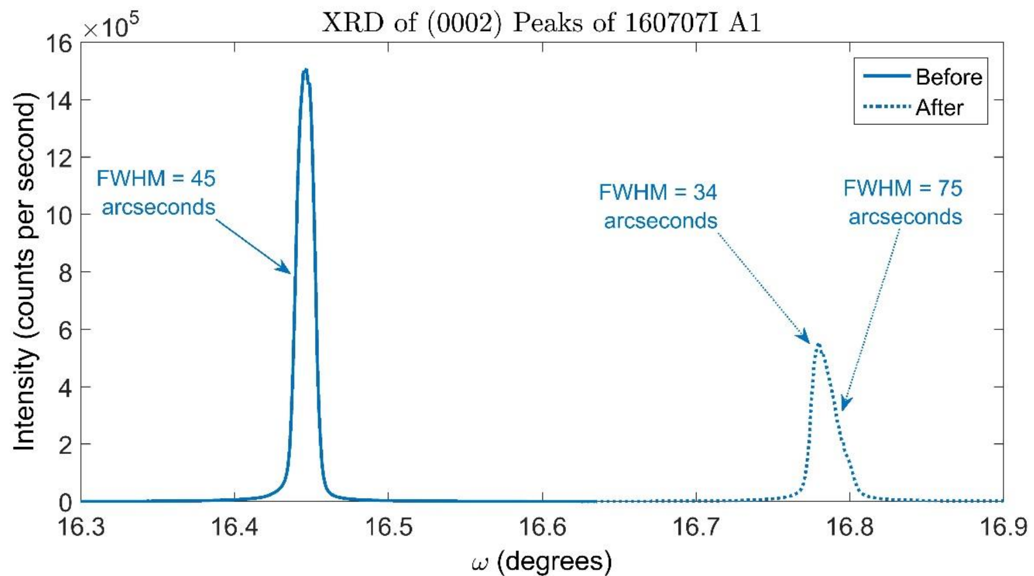

Figure 37. XRD data of (0002) peaks of 160707I A1. Note the peak after growth was best fit with two Gaussian peaks and thus has two FWHM associated with it.

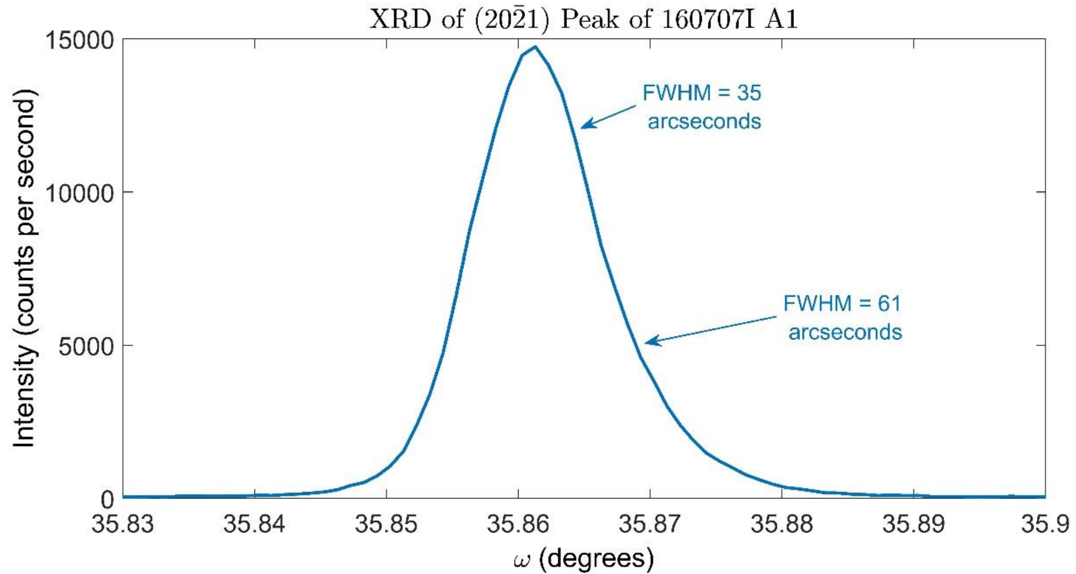

Figure 38. XRD data for $(20\bar{2}1)$ peak of 160707I A1. The exceptionally narrow peak is indicative of high quality material.

160714I

Growth run 160714I was similar to 160604I but had a different reactor body. Although not detected until after the run, the body for 160714I was significantly smaller than 160604I. Although in absolute terms, the diameter was only smaller by .01 inches, the baffle to inner diameter difference was only designed to be .03 inches. With such tight tolerances, the diameter difference appeared to dramatically reduce fluid flow between zones, resulting in a much smaller growth rate. The growth and dissolution temperatures were 700°C and 650°C with 0.640 g of NH_4Cl and the run lasting 96 hours. Two seeds were placed in the growth zone, both at the same height (approximately .75 inches above the reactor bottom), one a c-plane seed from Nanowin (A1) and one an m-plane seed from MCC (A2).

Neither seed exhibited highly desirable growth. Both seeds exhibited significant green coloration and A1 was no longer specular. A1 was also somewhat absorbing, leading to a dark green coloration. The growth rates were also much smaller and the polyGaN deposition on

the walls was a much smaller mass than average leading to the conclusion of reduced mass transport between zones. Neither seed appeared to have significant edge growth as seen in the earlier growths. However, the seeds only grew by around 100-132 μm (25-33 μm/day) and thus perhaps the edge growth did not have enough material to be easily distinguished. The A2 growth was very small, around 5-16 μm (1.25-4 μm/day). It was specular, unlike the growth on A1. Unfortunately due to the very thin growth, XRD of the growth is rather difficult because the substrate will also be probed. This doesn't preclude any analysis using XRD, but it does require caution when making conclusions from the results. Possible faceting was observed on A1, but the roughness of the growth prevented any measurements on angle.

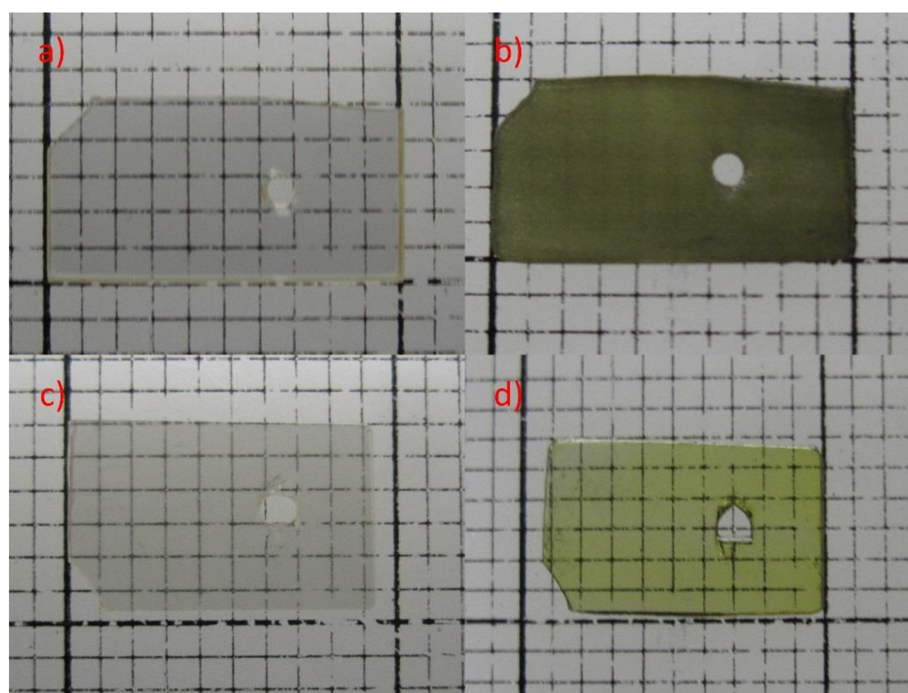

Figure 39. Optical images of 160714I a) A1 before growth and b) A1 after growth as well as c) A2 before growth and d) A2 after growth. Note that the seeds were grown at the same position in the reactor and the growth on A1 (panel b) is much thicker than the growth on A2 (panel d).

General Trends in Growth

The work presented in this chapter represents a preliminary study of growth and the impact of different environmental conditions as well as seed conditions that affect the growth. The results certainly warrant a larger and more in-depth study on parameters ranging from chemical driving force to absolute temperature to seed quality. It would be suspected that larger chemical driving force would increase the probability of defect generation, but certainly there is some limit where defects are not generated. Chemical driving force would be expected to be positively correlated with growth rate and thus high chemical driving force may be desirable. Although baffle design was not varied in this study, the fluid dynamics of the transport fluid can dramatically impact growth rate. It would be advisable then to also study the effect of baffle design on growth rate as well as the temperature stability of the growth and dissolution zones.

Although preliminary in nature, this study can yield valuable conclusions for future work. High transparency, single crystal GaN has been demonstrated in a new reactor design with a novel reactor material, indicating that molybdenum and TZM can be used for ammonothermal growth without detrimental effects. Reasonable growth rates were achieved while little to no optimization of fluid flow in the system was attempted, suggesting that some optimization may dramatically increase growth rate. The origin of the non-uniformity of growth on the seeds is still not explained, but at least two possible conclusions exist. The proximity of the seed edges to the walls may have produced a temperature gradient across the seed, thus increasing the chemical driving force at the seed edges resulting in excess growth. Alternatively, the fluid passing over the seed must first encounter the edges and with a high attachment rate of GaN, much of the supersaturated GaN intermediate reacted at the edges,

leaving less to be deposited on the seed center. Faceting may also occur at the seed edges, leading to other planes that can preferentially grow out. The higher temperature at the walls explanation indicates that the uniformity problem is a reactor design issue. The faceting would indicate that the edge growth is actually not a problem, but instead is the evolution of the seed to the equilibrium crystal shape.

Sample	NH_4Cl (g)	T_{growth} (°C)	$T_{dissolution}$ (°C)	Min. Growth Rate (µm/day)	Max Growth Rate (µm/day)	Wall growth (g)	Growth time (days)
160415I A1	0.625	650	500	24	24	0.14	4
160517I A1	0.638	650	500	16	26	0.06	4
160604I A1	0.638	700	650	82	175	0.50	4
160614I A1	0.640	750	697	32	145	0.58	4
160630I A1	0.205	700	650	57	153	0.49	2
160707I A1	0.206	700	675	99	191	0.70	2
160714I A1	0.640	700	650	25	33	0.09	4
160714I A2	0.640	700	650	1.25	4	0.09	4

Table 2. Summary of growth data for seeded growth of GaN.

Samples 160630I A1, 160614I A1, and 160604I A1 all were larger seeds but 160630I A1 exhibited reduced edge growth. Sample 160707I A1 also exhibited reduced edge growth while also having a smaller seed. All of the samples had comparable growth rates, (see Table 2) but the lower NH_4Cl samples appeared to have better growth uniformity. This could be related to the reduced mineralizer content, but those samples also had a shorter growth time. A thermal gradient across the seed should make the edge growth become more pronounced or stay the same (at least proportional to the growth rate) as the mineralizer content is reduced, as more GaN in solution would either be limited by site attachment (meaning the supersaturation would not change by changing the mineralizer content) or by the amount of GaN present in solution (meaning that as mineralizer content decreases less GaN is in solution so the same amount of GaN precipitated would reduce the supersaturation more so). We see a significant contradiction, essentially the opposite trend. Suppose then, that faceting occurs at the edges

and attachment at the edges is preferred because less stable planes are formed. The better uniformity could be explained by the reduced growth time as the growth step would initiate at the edges and grow inward toward the center of the sample. If this is the case, we should see inclined planes on the outer edges of all of the samples. This is clear in most of the samples, as shown in Figure 40 and Figure 41. The reduced edge growth on the shorter growth runs then was not due to a thermal gradient, but rather the transition toward an equilibrium shape was not as advanced as in the longer growths. This is also supported by the presence of the less stable planes from the $\{10\bar{1}2\}$, $\{10\bar{1}4\}$, and $\{10\bar{1}5\}$ families. This conclusion is rather interpretive, but more data with varying growth times should elicit a solution to the question. Such an experimental growth series should lead to one of two conclusions. Either the edge will continue to have significantly higher growth rates leading to a bowl-shaped sample, which would indicate that higher supersaturation at the edges is the cause, or the facets growing into the center of the sample will meet and form a single, flat face. After the flat face has formed, the seed growth will continue in a planar fashion. The formation of a planar growth face with time would indicate that the seed was instead simply forming an equilibrium shape. Bryant et al. found $\{10\bar{1}1\}$ planes forming by HVPE but there was some mention of transient $\{10\bar{1}n\}$ planes, where $n > 1$.[193] Similarly, Mikawa et al. found $\{10\bar{1}1\}$ planes when growing out an m-plane seed and made no mention of $\{10\bar{1}2\}$ planes were mentioned. However, their growth was performed at slightly lower temperature (max of 650°C, although only a range of 500-650°C was specified) and possibly for much longer (they specify a grow rate of several hundred micrometers per day with a crystal thickness of several millimeters).[138] Perhaps at significantly longer growth times, the $\{10\bar{1}1\}$ facets will emerge and become the dominant semipolar plane. It is interesting to note that $\{10\bar{1}4\}$ and $\{10\bar{1}5\}$ appeared in the higher

temperature growth. This may be an artifact of the pressure leaks that were observed during the run, causing etching or prohibiting the transition toward the less inclined planes. The $\{10\bar{1}4\}$ and $\{10\bar{1}5\}$ planes were observed on the high growth corner and on the dissolved edge.

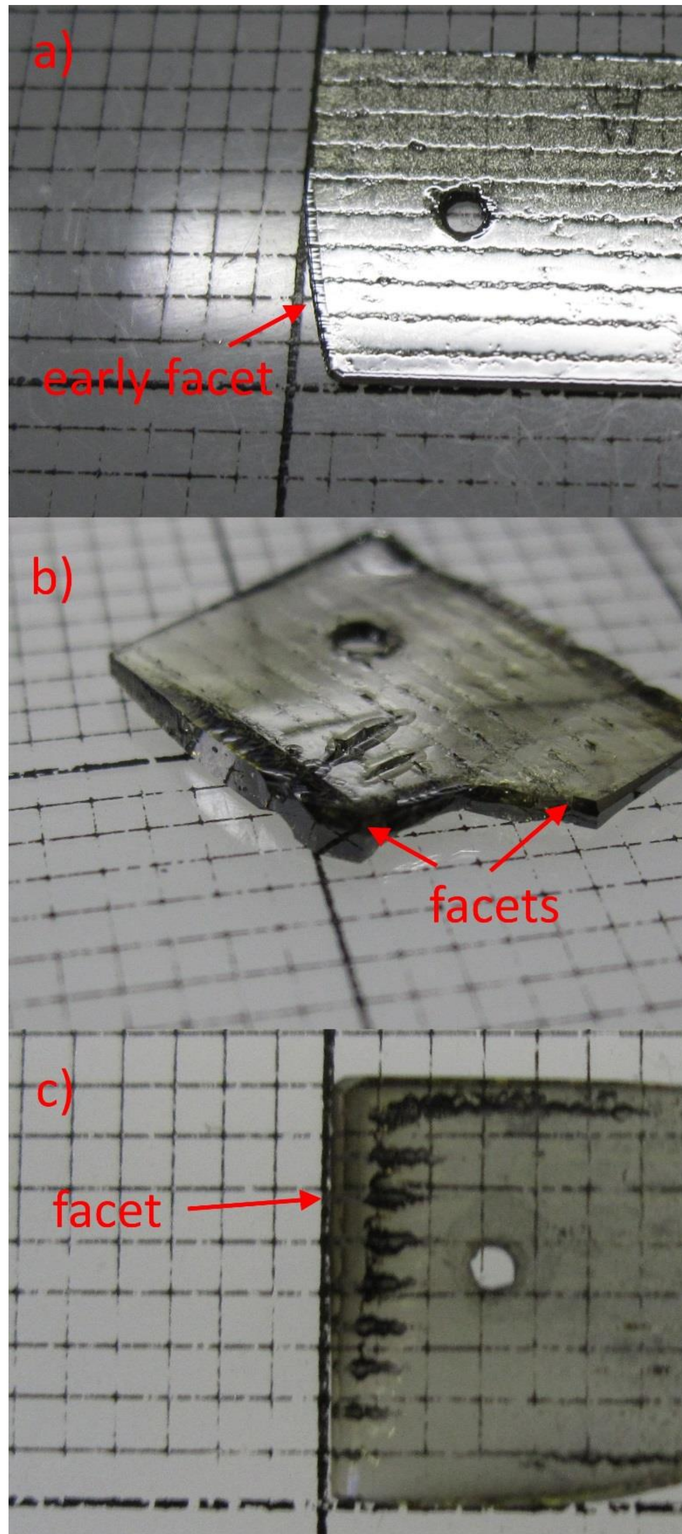

Figure 40. Optical images of a) 160517I A1, b) 160604I A1, and c) 160614I A1. Arrows indicate where the faceting inclined between the m-plane and c-planes is occurring.

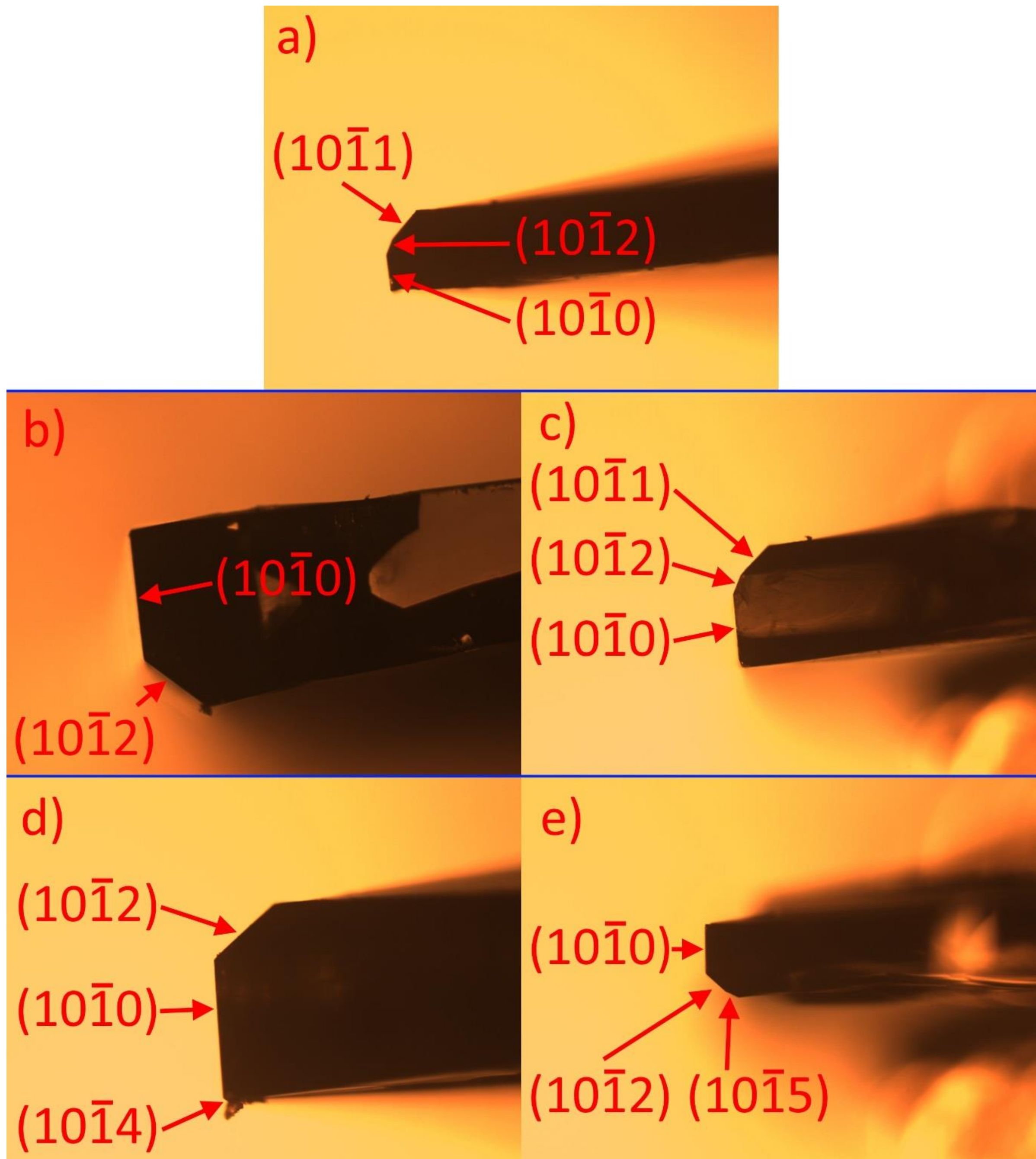

Figure 41. Optical micrographs of facets on a) 160517I A1, b) and c) 160604I A1, d) and e) 160614I A1. Note all semipolar planes observed have m-plane character.

With respect to impurity incorporation, no real conclusion can be drawn yet. The variance in seed type as well as the lack of SIMS data precludes any useful quantitative conclusion. However, the lack of coloration is a highly encouraging result. The coloration on the new

facets forming may be a result of differing oxygen incorporation on different planes. It is worth noting that planar growth appears fairly transparent, while the faceted growth is either highly absorbing or greenish in color. Care should be taken with this analysis, however, as differences in thickness will alter absorption. Longer growths with polished samples surfaces would yield more reasonable absorption data than what would be attainable with the current samples. Part of the problem is the source polyGaN. The measured oxygen concentration was rather high, as measured by a previous researcher using SIMS (~10^{19} cm^{-3}). Cleaner source material would eliminate this source of oxygen. The possibility also exists that the reactor walls themselves have some oxygen dissolved into the metal and the oxygen is leached out into the growth environment. With a high oxygen presence in the source, such a determination is not really possible.

The TZM reactor still allows for the possibility of even higher growth temperatures and the lack of ammonothermal growth data makes this temperature regime an area of high interest. This work has been a preliminary step for high temperature growth and should be followed by more systematic and directed studies. The impact of chemical driving force and temperature on growth is all but unknown, while the demonstration of high quality growth has been at least somewhat satisfied. One could suspect that higher temperatures will lead to faster growth while maintaining high quality crystals, but until the understanding and a demonstration of such a feat is presented it will remain speculation.

REFERENCES

1. Denbaars, S. P. *et al.* Development of gallium-nitride-based light-emitting diodes (LEDs) and laser diodes for energy-efficient lighting and displays. *Acta Mater.* **61,** 945–951 (2013).
2. Dollen, P. Von, Pimputkar, S. & Speck, J. S. Let There Be Light — With Gallium Nitride : The 2014 Nobel Prize in Physics. *Angew. Chem. Int. Ed. Engl.* **53,** 13978–13980 (2014).
3. Chowdhury, S., Swenson, B. L., Wong, M. H. & Mishra, U. K. Current status and scope of gallium nitride-based vertical transistors for high-power electronics application. *Semicond. Sci. Technol.* 074014 (2013). doi:10.1088/0268-1242/28/7/074014
4. Scott, M. J. *et al.* Merits of gallium nitride based power conversion. *Semicond. Sci. Technol.* 074013 (2013). doi:10.1088/0268-1242/28/7/074013
5. Keller, S. *et al.* Influence of sapphire nitridation on properties of gallium nitride grown by metalorganic chemical vapor deposition. *Appl. Phys. Lett.* **68,** 1525–1527 (1996).
6. Keller, S. *et al.* Growth of bulk InGaN films and quantum wells by atmospheric pressure metalorganic chemical vapour deposition. *J. Cryst. Growth* **170,** 349–352 (1997).
7. Bulman, G. E. *et al.* Pulsed Operation Lasing in a Cleaved-Facet InGaN/GaN MQW SCH Laser Grown on 6H-SiC. *Electron. Lett.* **33,** 1556–1557 (1997).
8. Briot, O., Alexis, J. P., Tchounkeu, M. & Aulombard, R. L. Optimization of the MOVPE growth of GaN on sapphire. *Mater. Sci. Eng. B* **5107,** 147–153 (1997).
9. Nakamura, S. The Roles of Structural Imperfections in InGaN-Based Blue Light-Emitting Diodes and Laser Diodes. *Science (80-.).* **281,** 956–961 (1998).
10. Nakamura, S., Senoh, M. & Mukai, T. Highly P-Typed Mg-Doped GaN Films Grown with GaN Buffer Layers. *Jpn. J. Appl. Phys.* **30,** L1708–L1711 (1991).
11. Wu, X. H. *et al.* Nucleation layer evolution in metal-organic chemical vapor deposition grown GaN. *Appl. Phys. Lett.* **68,** 1371 (1996).
12. Amano, H., Akasaki, I., Hiramatsu, K., Koide, N. & Sawaki, N. Effects of the buffer layer in metalorganic vapour phase epitaxy of GaN on sapphire substrate. *Thin Solid Films* **163,** 415–420 (1988).
13. Bläsing, J., Reiher, a., Dadgar, a., Diez, a. & Krost, a. The origin of stress reduction by low-temperature AlN interlayers. *Appl. Phys. Lett.* **81,** 2722 (2002).
14. Nakamura, S. III-V Nitride-Based Blue LDs with Modulation-Doped Strained-Layer Superlattices. *24th IEEE Symp. Compd. Semicond.* **156,** 1–4 (1998).
15. Jeng, M.-J., Lee, Y.-L. & Chang, L.-B. Temperature dependences of In x Ga 1− x N multiple quantum well solar cells. *J. Phys. D. Appl. Phys.* **42,** 105101 (2009).
16. Adgar, A. D. *et al.* Metalorganic Chemical Vapor Phase Epitaxy of Crack-Free GaN on Si (111) Exceeding 1 μm in Thickness. *Jpn. J. Appl. Phys.* **39,** L1183–L1185 (2000).
17. Ploog, K. H., Brandt, O., Yang, H., Menniger, J. & Klann, R. Interplay between growth kinetics and material quality of cubic GaN. *Solid. State. Electron.* **41,** 235–237 (1997).
18. Kurobe, T., Sekiguchi, Y., Suda, J., Yoshimoto, M. & Matsunami, H. Preferential

growth of cubic GaN on sapphire (0001) substrates by metal organic molecular beam epitaxy. *Appl. Phys. Lett.* **73,** 2305 (1998).
19. Ploog, K. H. Nucleation and growth of GaN layers on GaAs, Si, and SiC substrates. *J. Vac. Sci. Technol. B Microelectron. Nanom. Struct.* **16,** 2229 (1998).
20. Hardy, M. T., Feezell, D. F., Denbaars, S. P. & Nakamura, S. Group III-nitride lasers: A materials perspective. *Mater. Today* **14,** 408–415 (2011).
21. Masui, H. *et al.* Light-polarization characteristics of electroluminescence from InGaN/GaN light-emitting diodes prepared on (11-22) -plane GaN. *J. Appl. Phys.* **100,** 0–5 (2006).
22. Masui, H., Nakamura, S., DenBaars, S. P. & Mishra, U. K. Nonpolar and semipolar III-nitride light-emitting diodes: Achievements and challenges. *IEEE Trans. Electron Devices* **57,** 88–100 (2010).
23. Kolbe, T. *et al.* Optical polarization characteristics of ultraviolet (In)(Al)GaN multiple quantum well light emitting diodes. *Appl. Phys. Lett.* **97,** 16–19 (2010).
24. Zhao, Y. *et al.* High optical polarization ratio from semipolar (2021) blue-green InGaN/GaN light-emitting diodes. *Appl. Phys. Lett.* **99,** 18–21 (2011).
25. Ansari, A., Gokhale, V. J., Thakar, V. A., Roberts, J. & Rais-Zadeh, M. Gallium nitride-on-silicon micromechanical overtone resonators and filters. *Tech. Dig. - Int. Electron Devices Meet. IEDM* 485–488 (2011). doi:10.1109/IEDM.2011.6131590
26. Ansari, A. *et al.* GaN Micromechanical Resonators with Meshed Metal Bottom Electrode. *Materials (Basel).* **8,** 1204–1212 (2015).
27. Liu, L. & Edgar, J. H. H. Substrates for gallium nitride epitaxy. *Mater. Sci. Eng. R Reports* **37,** 61–127 (2002).
28. Ito, K. *et al.* Effects of TiN Buffer Layer Thickness on GaN Growth. *J. Electron. Mater.* **38,** 511–517 (2008).
29. Okamoto, K., Inoue, S., Nakano, T., Ohta, J. & Fujioka, H. Epitaxial growth of GaN on single-crystal Mo substrates using HfN buffer layers. *J. Cryst. Growth* **311,** 1311–1315 (2009).
30. Rozhavskaya, M. M. *et al.* Gallium nitride nanowires and microwires with exceptional length grown by metal organic chemical vapor deposition via titanium film. *J. Appl. Phys.* **117,** (2015).
31. Wölz, M. *et al.* Epitaxial Growth of GaN Nanowires with High Structural Perfection on a Metallic TiN Film. *Nano Lett.* **15,** 3743−3747 (2015).
32. LEWIS, J., SCHWARZENBACH, D. & FLACK, H. D. Electric-Field Gradients and Charge-Density in Corundum, Alpha-Al2O3. *Acta Crystallogr. Sect. A* **38,** 733–739 (1982).
33. Romanov, A. E., Baker, T. J., Nakamura, S. & Speck, J. S. Strain-induced polarization in wurtzite III-nitride semipolar layers. *J. Appl. Phys.* **100,** (2006).
34. Leszczynski, M. *et al.* Thermal expansion of gallium nitride. *J. Appl. Phys.* **76,** 4909 (1994).
35. Kozawa, T. *et al.* Thermal stress in GaN epitaxial layers grown on sapphire substrates. *J. Appl. Phys.* **77,** 4389 (1995).
36. Hanser, A. D. & Evans, K. R. Development of the Bulk GaN Substrate Market. *Challenges*
37. Yuchao, Z. *et al.* Threading dislocation density comparison between GaN grown on the patterned and conventional sapphire substrate by high resolution X-ray

diffraction. *Sci. China Physics, Mech. Astron.* **53,** 465–468 (2010).
38. Usui, A., Sunakawa, H., Sakai, A. & Atsushi, A. Y. Thick GaN Epitaxial Growth with Low Dislocation Density by Hydride Vapor Phase Epitaxy. *Jpn. J. Appl. Phys.* **36,** L899–L902 (1997).
39. Ikeda, M. & Uchida, S. Blue-violet laser diodes suitable for blu-ray disk. *Phys. Status Solidi Appl. Res.* **194,** 407–413 (2002).
40. Ali, M. *et al.* Void shape control in GaN re-grown on hexagonally patterned mask-less GaN.pdf. *J. Cryst. Growth* **315,** 188–191 (2011).
41. Yu, Z. *et al.* Study of the Epitaxial Lateral Overgrowth (ELO) Process for GaN on Sapphire Using Scanning Electron Microscopy and Monochromatic Cathodoluminescence. *MRS Internet J. Nitride Semicond. Res.* **3,** 6 (1998).
42. Singh, R., Barrett, R. J., Gomes, J. J., Dabkowski, F. P. & Moustakas, T. D. Selective Area Growth of GaN Directly on (0001) Sapphire by the HVPE Technique. *MRS Internet J. Nitride Semicond. Res.* **3,** 13 (1998).
43. H. Marchand *et al.* Atomic force microscopy observation of threading dislocation density reduction in lateral epitaxial overgrowth of gallium nitride by MOCVD. *MRS Internet J. Nitride Semicond. Res.* **3,** e3 (1998).
44. Polyakov, A. Y., Smirnov, N. B., Yakimov, E. B., Lee, I. H. & Pearton, S. J. Electrical, luminescent, and deep trap properties of Si doped n-GaN grown by pendeo epitaxy. *J. Appl. Phys.* **119,** (2016).
45. Keller, S. *et al.* Growth and Characterization of InGaN/GaN Double Heterostructure LEDs grown by MOCVD. in *Proceedings IEEE/Cornell Conference on Advanced Concepts in High Speed Semiconductor Devices and Circuits* 56–63 (Ieee, 1995). doi:10.1109/CORNEL.1995.482420
46. Edmond, J. *et al.* Nitride-based emitters on SiC substrates. *Silicon Carbide, Iii-Nitrides Relat. Mater. Pts 1 2* **264-2,** 1421–1424 (1998).
47. Kimoto, T. Material science and device physics in SiC technology for high-voltage power devices. *Jpn. J. Appl. Phys.* **54,** 040103 (2015).
48. Polymorphs of Silicon Carbide. *Wikipedia* at <https://en.wikipedia.org/wiki/Polymorphs_of_silicon_carbide>
49. Taylor, B. A. The Formation and Crystal Structure of Silicon Carbide The Formation and Crystal Structure of Silicon Carbide. **174,** (1950).
50. Edmond, J. *et al.* High efficiency GaN-based LEDs and lasers on SiC. *J. Cryst. Growth* **272,** 242–250 (2004).
51. Linthicum, K. *et al.* Pendeoepitaxy of gallium nitride thin films. *Appl. Phys. Lett.* **75,** 196 (1999).
52. Zheleva, T. S. *et al.* Pendeo-Epitaxy : A New Approach for Lateral Growth of Gallium Nitride Films. *J. Electron. Mater.* **28,** L5–L8 (1999).
53. Mullin, J. B. in *Handbook of Crystal Growth: Bulk Crystal Growth: Second Edition* **2,** 105–130 (Elsevier B.V., 2015).
54. Sanorpim, S., Takuma, E., Ichinose, H., Katayama, R. & Onabe, K. Structural transition control of laterally overgrown c-GaN and h-GaN on stripe-patterned GaAs (001) substrates by MOVPE. *Phys. Status Solidi* **244,** 1769–1774 (2007).
55. Paskova, T., Hanser, D. a & Evans, K. R. GaN Substrates for III-Nitride Devices. *Proc. IEEE* **98,** 1324–1338 (2010).
56. Friedrich, J., Ammon, W. von & Müller, G. in *Handbook of Crystal Growth: Bulk*

Crystal Growth: Second Edition 45–104 (Elsevier B.V., 2015). doi:10.1016/B978-0-323-29965-7.00002-6
57. Falster, R., Voronkov, V. V & Mutti, P. The Control and Engineering of Intrinsic Point Defects in Silicon Wafers and Crystals. *Mater. Sci. Eng. B* **73,** 87–94 (2000).
58. Gehrke, T. *et al.* Pendeo-epitaxial growth of gallium nitride on silicon substrates. *J. Electron. Mater.* **29,** 306–310 (2000).
59. Davis, R. F. *et al.* Conventional and pendeo-epitaxial growth of GaN (0 0 0 1) thin films on Si (1 1 1) substrates. *J. Cryst. Growth* **231,** 335–341 (2001).
60. Kikkawa, T. *et al.* 600 v JEDEC-qualified highly reliable GaN HEMTs on Si substrates. *Tech. Dig. - Int. Electron Devices Meet. IEDM* **2015-Febru,** 2.6.1–2.6.4 (2015).
61. Selvaraj, S. L., Suzue, T. & Egawa, T. Breakdown Enhancement of AlGaN/GaN HEMTs on 4-in Silicon by Improving the GaN Quality on Thick Buffer Layers. *IEEE Electron Device Lett.* **30,** 587–589 (2009).
62. Lee, J. *et al.* Growth of high-quality InGaN/GaN LED structures on (111) Si substrates with internal quantum efficiency exceeding 50%. *J. Cryst. Growth* **315,** 263–266 (2011).
63. Armitage, R. *et al.* Lattice-matched HfN buffer layers for epitaxy of GaN on Si. *Appl. Phys. Lett.* **81,** 1450 (2002).
64. Bru-Chevallier, C. *et al.* Optical Properties of Cubic Gallium Nitride on SiC/Si Pseudo-Substrates. *Phys. Status Solidi* **183,** 67–73 (2001).
65. Sorokin, L. M. *et al.* Structural Characterization of GaN Epilayers on Silicon : Effect of Buffer Layers. *Tech. Phys. Lett.* **37,** 326–329 (2011).
66. Koukitu, A. & Kumagai, Y. in *Technology of Gallium Nitride Crystal Growth* 31–60 (2010).
67. Bickermann, M. & Paskova, T. in *Handbook of Crystal Growth: Bulk Crystal Growth: Second Edition* **2,** 621–669 (Elsevier B.V., 2014).
68. Richter, E., Gründer, M., Netzel, C., Weyers, M. & Tränkle, G. Growth of GaN boules via vertical HVPE. *J. Cryst. Growth* **350,** 10–13 (2011).
69. Fujito, K. *et al.* Bulk GaN crystals grown by HVPE. *J. Cryst. Growth* **311,** 3011–3014 (2009).
70. Richter, E. *et al.* Hydride vapor phase epitaxy of GaN boules using high growth rates. *J. Cryst. Growth* **312,** 2537–2541 (2010).
71. Oshima, Y. *et al.* in *Technology of Gallium Nitride Crystal Growth* 79–96 (2010).
72. Motoki, K. Development of Gallium Nitride Substrates. *SEI Tech. Rev.* **70,** 28–35 (2010).
73. Liu, J. Q. *et al.* High-resolution X-ray diffraction analysis on HVPE-grown thick GaN layers. *J. Cryst. Growth* **311,** 3080–3084 (2009).
74. Etzkorn, E. V. & Clarke, D. R. Cracking of GaN films. *J. Appl. Phys.* **89,** 1025 (2001).
75. Yamane, H., Shimada, M., Clarke, S. J. & Disalvo, F. J. Preparation of GaN Single Crystals Using a Na Flux. *Chem. Mater.* 413–416 (1997).
76. Yamane, H., Kinno, D., Shimada, M. & Disalvo, F. J. Growth of GaN from Melt in BN Containers. *J. Ceram. Soc. Japan* **929,** 925–929 (1999).
77. Yamane, H., Kinno, D., Shimada, M., Sekiguchi, T. & DiSalvo, F. J. GaN single crystal growth from a Na-Ga melt. *J. Mater. Sci.* **35,** 801–808 (2000).

78. Avrutin, V. *et al.* Growth of Bulk GaN and AlN : Progress and Challenges. *Proc. IEEE* **98,** 1302–1315 (2010).
79. Yamane, H., Shimada, M., Sekiguchi, T. & DiSalvo, F. J. Morphology and characterization of GaN single crystals grown in a Na flux. *J. Cryst. Growth* **186,** 8–12 (1998).
80. Lakshmanan, a. R. R., Prasad, M. V. R. V. R., Ponraju, D. & Krishnan, H. A novel method of non-violent dissolution of sodium metal in a concentrated aqueous solution of Epsom salt. *J. Solid State Chem.* **177,** 3460–3468 (2004).
81. Yano, M. *et al.* Control of Nucleation Site and Growth Orientation of Bulk GaN Crystals. *Jpn. J. Appl. Phys.* **38,** L1121–L1123 (1999).
82. Yano, M. *et al.* Growth of nitride crystals , BN , AlN and GaN by using a Na flux. *Diam. Relat. Mater.* **9,** 512–515 (2000).
83. Kawamura, F. *et al.* Effect of carbon additive on increases in the growth rate of 2in GaN single crystals in the Na flux method. *J. Cryst. Growth* **310,** 3946 (2008).
84. Aoki, M., Yamane, H., Shimada, M., Sarayama, S. & Disalvo, F. J. Growth Conditions and Morphology of GaN Single Crystals Fabricated by the Na Flux Method. *J. Ceram. Soc. Japan* **109,** 858–862 (2001).
85. Aoki, M., Yamane, H., Shimada, M., Sarayama, S. & DiSalvo, F. J. Growth of 5 mm GaN Single Crystals at 750 ° C from Na-Ga Melt. *Cryst. Growth Des.* **1,** 119–122 (2001).
86. Onda, M. *et al.* Influence of pressure control on the growth of bulk GaN single crystal using a Na flux. *J. Cryst. Growth* **237-239,** 2112–2115 (2002).
87. Aoki, M. *et al.* Dissolution and Recrystallization of GaN in Molten Na. *Jpn. J. Appl. Phys.* **42,** 7272–7275 (2003).
88. Yamada, T., Yamane, H., Ohta, T., Goto, T. & Yao, T. Preparation of GaN crystals by heating a Li3N-added Ga melt in Na vapor and their photoluminescence. *Cryst. Res. Technol.* **42,** 13–17 (2007).
89. Song, Y., Wang, W., Yuan, W., Wu, X. & Chen, X. Bulk GaN single crystals: growth conditions by flux method. *J. Cryst. Growth* **247,** 275–278 (2003).
90. Morishita, M. *et al.* Growth of Bulk GaN Single Crystals Using Li-Na Mixed Flux System. *Jpn. J. Appl. Phys.* **42,** L565–L567 (2003).
91. Lee, K. K., Cai, Z., Ziemer, K. & Doolittle, W. A. The origin of the residual conductivity of GaN films on ferroelectric materials. *J. Cryst. Growth* **311,** 4001–4006 (2009).
92. Kawamura, F. *et al.* Synthesis of Bulk GaN Single Crystals Using Na-Ca Flux. *Jpn. J. Appl. Phys.* **41,** L1440–L1442 (2002).
93. Morishita, M. *et al.* Promoted nitrogen dissolution due to the addition of Li or Ca to Ga-Na melt; some effects of additives on the growth of GaN single crystals using the sodium flux method. *J. Cryst. Growth* **284,** 91–99 (2005).
94. Kawamura, F. *et al.* Growth of Transparent, Large Size GaN Single Crystal with Low Dislocations Using Ca-Na Flux System. *Jpn. J. Appl. Phys.* **42,** L729–L731 (2003).
95. Kawamura, F. *et al.* Novel Liquid Phase Epitaxy (LPE) Growth Method for Growing Large GaN Single Crystals: Introduction of the Flux Film Coated-Liquid Phase Epitaxy (FFC-LPE) Method. *Jpn. J. Appl. Phys.* **42,** L879–L881 (2003).
96. Imade, M. *et al.* Growth of Large GaN Single Crystals on High-Quality GaN Seed by Carbon-Added Na Flux Method. *Appl. Phys. Express* **3,** 075501 (2010).

97. Mori, Y. *et al.* Growth of bulk GaN crystals by Na flux method. *Phys. Status Solidi* **8,** 1445–1449 (2011).
98. Kawamura, F. *et al.* Growth of a Two-Inch GaN Single Crystal Substrate Using the Na Flux Method. *Jpn. J. Appl. Phys.* **45,** L1136–L1138 (2006).
99. Yamane, H. *et al.* Time Dependence of the Growth Morphology of GaN Single Crystals Prepared in a Na–Ga Melt. *Jpn. J. Appl. Phys.* **44,** 3157–3160 (2005).
100. Pimputkar, S., Kawabata, S., Speck, J. S. & Nakamura, S. Improved growth rates and purity of basic ammonothermal GaN. *J. Cryst. Growth* **403,** 7–17 (2014).
101. Dwiliński, R. *et al.* On GaN Crystallization by Ammonothermal Method. in *Proceedings of the XXV International School of Semiconducting Compounds* 763–766 (1996).
102. Ehrentraut, D. & Fukuda, T. Ammonothermal crystal growth of gallium nitride – A brief discussion of critical issues. *J. Cryst. Growth* **312,** 2514–2518 (2010).
103. Dwiliński, R. *et al.* GaN Synthesis By Ammonothermal Method. in *Proceedings of the XXIV International School of Semiconducting Compounds* (1995).
104. Dwiliński, R. *et al.* Some Optical and EPR Properties by Strain-Free GaN Crystals Obtained by Ammono Method. in *Proceedings of the XXVI International School on Physics of Semiconducting Compounds* **92,** 737–741 (1997).
105. Pimputkar, S. *et al.* Free electron concentration dependent sub-bandgap optical absorption characterization of bulk GaN crystals. *J. Cryst. Growth* **432,** 49–53 (2015).
106. Lan, Y. ., Chen, X. ., Xu, Y. ., Cao, Y. . & Huang, F. Syntheses and structure of nanocrystalline gallium nitride obtained from ammonothermal method using lithium metal as mineralizator. *Mater. Res. Bull.* **35,** 2325–2330 (2000).
107. Ketchum, D. R. & Kolis, J. W. Crystal growth of gallium nitride in supercritical ammonia. *J. Cryst. Growth* **222,** 431–434 (2001).
108. Bai, J. *et al.* Correlated structural and optical characterization of ammonothermally grown bulk GaN. *Appl. Phys. Lett.* **84,** 3289 (2004).
109. Hashimoto, T. *et al.* Phase selection of microcrystalline GaN synthesized in supercritical ammonia. *J. Cryst. Growth* **291,** 100–106 (2006).
110. Hashimoto, T. *et al.* Seeded growth of GaN by the basic ammonothermal method. *J. Cryst. Growth* **305,** 311–316 (2007).
111. Callahan, M. *et al.* GaN single crystals grown on HVPE seeds in alkaline supercritical ammonia. *J. Mater. Sci.* **41,** 1399–1407 (2006).
112. Lopatiuk, O. *et al.* Electron trapping effects in C- and Fe-doped GaN and AlGaN. *Solid. State. Electron.* **49,** 1662–1668 (2005).
113. Hashimoto, T. *et al.* Ammonothermal Growth of GaN Utilizing Negative Temperature Dependence of Solubility in Basic Ammonia. *Mater. Res. Soc. Symp. Proc.* **831,** 1–6 (2005).
114. Callahan, M. J. *et al.* Growth of GaN crystals under ammonothermal conditions. *Mater. Res. Soc. Symp. Proc.* **798,** 1–6 (2004).
115. Pimputkar, S. *et al.* Stability of materials in supercritical ammonia solutions. *J. Supercrit. Fluids* **110,** 193–229 (2016).
116. Wang, B. & Callahan, M. J. Transport growth of GaN crystals by the ammonothermal technique using various nutrients. *J. Cryst. Growth* **291,** 455–460 (2006).
117. Wang, B. *et al.* Ammonothermal growth of GaN crystals in alkaline solutions. *J. Cryst. Growth* **287,** 376–380 (2006).

118. Dwiliński, R. *et al.* Excellent crystallinity of truly bulk ammonothermal GaN. *J. Cryst. Growth* **310,** 3911–3916 (2008).
119. Chichibu, S. F. *et al.* Impacts of dislocation bending and impurity incorporation on the local cathodoluminescence spectra of GaN grown by ammonothermal method. *Appl. Phys. Lett.* **91,** 251911 (2007).
120. Meissner, E. *et al.* Cathodoluminescence imaging for the determination of dislocation density in differently doped HVPE GaN. *J. Cryst. Growth* **340,** 78–82 (2012).
121. Bao, Q. *et al.* Ammonothermal Crystal Growth of GaN Using an NH4F Mineralizer. *Cryst. Growth Des. Des.* **13,** 4158–4161 (2013).
122. Ehrentraut, D. *et al.* Temperature effect of ammonium halogenides as mineralizers on the phase stability of gallium nitride synthesized under acidic ammonothermal conditions. *J. Mater. Chem.* **17,** 886 (2007).
123. Purdy, A. Growth of cubic GaN crystals from hexagonal GaN feedstock. *J. Cryst. Growth* **281,** 355–363 (2005).
124. Ehrentraut, D., Kagamitani, Y., Yokoyama, C. & Fukuda, T. Physico-chemical features of the acid ammonothermal growth of GaN. *J. Cryst. Growth* **310,** 891–895 (2008).
125. Tomida, D. *et al.* Effect of halogen species of acidic mineralizer on solubility of GaN in supercritical ammonia. *J. Cryst. Growth* **325,** 52–54 (2011).
126. Schimmel, S. *et al.* Determination of GaN solubility in supercritical ammonia with NH4F and NH4Cl mineralizer by in situ x-ray imaging of crystal dissolution. *J. Cryst. Growth* **418,** 64–69 (2015).
127. Tomida, D. *et al.* Solubility of GaN in supercritical ammonia with ammonium chloride as a mineralizer. *J. Cryst. Growth* **312,** 3161–3164 (2010).
128. Yoshida, K., Aoki, K. & Fukuda, T. High-temperature acidic ammonothermal method for GaN crystal growth. *J. Cryst. Growth* **393,** 93–97 (2014).
129. Hertweck, B., Steigerwald, T. G., Alt, N. S. A. & Schluecker, E. Different corrosion behaviour of autoclaves made of nickel base alloy 718 in ammonobasic and ammonoacidic environments. *J. Supercrit. Fluids* **95,** 158–166 (2014).
130. Hertweck, B. *et al.* Applicability of Metals as Liner Materials for Ammonoacidic Crystal Growth. *Chem. Eng. Technol.* **37,** 1835–1844 (2014).
131. Purdy, A. P., Case, S. & Muratore, N. Synthesis of GaN by high-pressure ammonolysis of gallium triiodide. *J. Cryst. Growth* **252,** 136–143 (2003).
132. Purdy, A. P., Jouet, R. J. & George, C. F. Ammonothermal Recrystallization of Gallium Nitride with Acidic Mineralizers. *Cryst. Growth Des.* **2,** 141–145 (2002).
133. Yoshikawa, a., Ohshima, E., Fukuda, T., Tsuji, H. & Oshima, K. Crystal growth of GaN by ammonothermal method. *J. Cryst. Growth* **260,** 67–72 (2004).
134. Kagamitani, Y. *et al.* Ammonothermal Epitaxy of Thick GaN Film Using NH 4 Cl Mineralizer. *Jpn. J. Appl. Phys.* **45,** 4018–4020 (2006).
135. Kagamitani, Y. *et al.* Ammonothermal epitaxy of wurtzite GaN using an NH4I mineralizer. *J. Cryst. Growth* **312,** 3384–3387 (2010).
136. Jiang, W. *et al.* Highly transparent ammonothermal bulk GaN substrates. *J. Cryst. Growth* **403,** 18–21 (2014).
137. Ehrentraut, B. D. & Fukuda, T. The Ammonothermal Crystal Growth of Gallium Nitride -- Technique on the Up Rise. *Proc. IEEE* **98,** 1316–1323 (2010).
138. Mikawa, Y., Ishinabe, T., Kawabata, S. & Mochizuki, T. Ammonothermal Growth of

Polar and Non-polar Bulk GaN Crystal. *Proc. SPIE* **9363,** 936302 (2015).
139. Ehrentraut, D. *et al.* Ammonothermal synthesis of thick gallium nitride film employing acidic mineralizers. *J. Mater. Sci.* **43,** 2270–2275 (2007).
140. Bao, Q. *et al.* Acidic ammonothermal growth of GaN crystals using GaN powder as a nutrient. *CrystEngComm* **15,** 5382 (2013).
141. Jouet, R. J., Purdy, A. P., Wells, R. L. & Janik, J. F. Preparation of Phase Pure Cubic Gallium Nitride , c-GaN , by Ammonothermal Conversion of Gallium Imide , {Ga(NH)3/2}n. *J. Clust. Sci.* **13,** 469–486 (2002).
142. D'Evelyn, M. P. *et al.* Ammonothermal Bulk GaN Substrates for Power Electronics. *ECS Trans.* **58,** 287–294 (2013).
143. Bao, Q. *et al.* Ammonothermal growth of GaN on a self-nucleated GaN seed crystal. *J. Cryst. Growth* **404,** 168–171 (2014).
144. Mason, P. E. *et al.* Coulomb explosion during the early stages of the reaction of alkali metals with water. *Nat. Chem.* **7,** 1–5 (2015).
145. Saito, M. *et al.* Plane Dependent Growth of GaN in Supercritical Basic Ammonia. *Appl. Phys. Express* **1,** 121103 (2008).
146. Wagman, D. D. *et al.* The NBS Tables of Chemical Thermodynamic Properties. *Journal of Physical and Chemical Reference Data* **11,** 1–407 (1982).
147. Lane, R. W. & McDonald, H. J. Kinetics of the Reaction Between Copper and Aqueous Ammonia. *J. Am. Ceram. Soc.* **68,** 1699–1704 (1946).
148. Kempter, C. P., Krikorian, N. H. & McGuire, J. C. The Crystal Structure of Yttrium Nitride. *J. Phys. Chem.* **61,** 1237–1238 (1957).
149. Spedding, F. H., Daane, A. H. & Herrmann, K. W. The crystal structures and lattice parameters of high-purity scandium, yttrium and the rare earth metals. *Acta Crystallogr.* **9,** 559–563 (1956).
150. Pebler, A. & Wallace, W. E. Crystal Structures of Some Lanthanide Hydrides. *J. Phys. Chem.* **66,** 148–& (1962).
151. Sōmiya, S., Yoshimura, M. & Toraya, H. Reactions of titanium metal powders with high-temperature high-pressure ammonia. *J. Mater. Sci. Lett.* **4,** 91–93 (1985).
152. Cuthill, R., Hayes, W. D. & Seebold, R. E. I. Nitriding Phenomena in Titanium and the 6Al-4V Titanium Alloy. **64,** 119–125 (1960).
153. Nishikiori, T., Nohira, T. & Ito, Y. Hydrogen Impermeability of TiN Films and Its Dependence on Nitrogen Concentration at High Temperatures. *J. Electrochem. Soc.* **148,** E52 (2001).
154. Mueller, M. H. The lattice parameter of tantalum. *Scr. Metall.* **11,** 693 (1977).
155. Herman, R. von Niob und Tantal. **332,** (1953).
156. Hauck, B. Y. J. Structural Relations between Vanadium , Niobium , Tantalum Hydrides and Deuterides. *Acta Crystallogr. Sect. A* **34,** 389–399 (1978).
157. Duwez, P. & Odell, F. Phase Relationships in the Binary Systems of Nitrides and Carbides of Zirconium, Columbium, Titanium, and Vanadium. *J. Electrochem. Soc.* **97,** 299–304 (1950).
158. Hull, A. Crystal Structures of Vanadium, Germanium, and Graphite. *Phys. Rev.* **20,** 113 (1922).
159. Klemm, M. & Heusler, K. E. Hydrogen Deposition at Iron From Liquid Ammonia. *Electrochim. Acta* **36,** 283–290 (1991).
160. Adekore, B. T. *et al.* Ammonothermal Synthesis of Aluminum Nitride Crystals on

Group III – Nitride Templates. *J. Electron. Mater.* **35,** 1104–1111 (2006).
161. Usami, N. Fabrication of solar cell with stacked Ge islands for enhanced absorption in the infrared regime. *Thin Solid Films* **451-452,** 604–607 (2004).
162. Mitchell, D. W. Heat Contents and Heat of Formation of Magnesium Nitride. *Ind. Eng. Chem.* **41,** 2027–2031 (1949).
163. Juza, R. Ammonothermal Synthesis of Magnesium and Beryllium Amides. *Angew. Chem., Int. Ed.* **5,** 247–247 (1966).
164. Flanagan, T. E. D. B. & Lewis, F. A. Absorption of Hydrogen by Palladium/Platinum Alloys - Part 1: Electrical Resistance as a Function of Hydrogen Content and One-Atmosphere Isobars. *Trans. Faraday Soc.* **56,** 363–370 (1960).
165. Liu, C. T. & Inouye, H. Internal Oxidation and Mechanical Properties of TZM-Mo Alloy. *Metall. Trans.* **5,** 2515–2525 (1974).
166. Baimakov, Y. & Lebedev, O. Titanium and Hydrogen. *Metall. Nonferrous Met. Trans. Leningr. Polytech. Inst.* **223,** 25–34 (1963).
167. Mahmoud, M. H. H. Leaching platinum-group metals in a sulfuric acid/chloride solution. *J. Miner. Met. Mater. Soc.* **55,** 37–40 (2003).
168. Iron(III) Chloride. *Wikipedia* (2016). at <https://en.wikipedia.org/wiki/Iron(III)_chloride>
169. Copper(I) Chloride. *Wikipedia* at <https://en.wikipedia.org/wiki/Copper(I)_chloride>
170. Copper(II) Chloride. *Wikipedia* at <https://en.wikipedia.org/wiki/Copper(II)_chloride>
171. Nickel(II) Chloride. *Wikipedia* at <https://en.wikipedia.org/wiki/Nickel(II)_chloride>
172. Davidson, T. E. & Kendall, D. P. *The Design of Pressure Vessels for Very High Pressure Operation*. (1969). at <www.dtic.mil/dtic/tr/fulltext/u2/690183.pdf>
173. Cockeram, B. V, Chan, K. S. & Mifflin, W. B-T-3613 In-situ Fracture Studies and Modeling of the Toughening Mechanism Present in Wrought LCAC , TZM , and ODS Molybdenum Flat Products Bechtel-Bettis Atomic Power Laboratory , P . O . Box 79 , West Mifflin , PA 15122-0079. **0079,** (2007).
174. Cockeram, B. V. The mechanical properties and fracture mechanisms of wrought low carbon arc cast (LCAC), molybdenum–0.5pct titanium–0.1pct zirconium (TZM), and oxide dispersion strengthened (ODS) molybdenum flat products. *Mater. Sci. Eng. A* **418,** 120–136 (2006).
175. Plansee. Molybdenum. at <http://www.plansee.com/en/materials/molybdenum.html>
176. Smolik, G. R., Petti, D. A. & Schuetz, S. T. Oxidation and volatilization of TZM alloy in air. *J. Nucl. Mater.* **283-287,** 1458–1462 (2000).
177. Dolejš, D. & Baker, D. R. Phase transitions and volumetric properties of cryolite , Na3AlF6: Differential thermal analysis to 100 MPa. *Am. Mineral.* **91,** 97–103 (2006).
178. Lindoo, A., Larsen, J. F., Cashman, K. V, Dunn, A. L. & Neill, O. K. An experimental study of permeability development as a function of crystal-free melt viscosity. *Earth Planet. Sci. Lett.* **435,** 45–54 (2016).
179. Métrich, N. & Rutherford, M. Low pressure crystallization paths of H2O-saturated basaltic-hawaiitic melts from Mt Etna : Implications for open-system degassing of basaltic volcanoes. *Geochemica Cosmochim. Acta* **62,** 1195–1205 (1998).
180. Rader, E. L. & Larsen, J. F. Experimental phase relations of a low MgO Aleutian basaltic andesite at XH2O=0.7–1. *Contrib. to Mineral. Petrol.* **166,** 1593–1611 (2013).

181. Williams, D. W. Externally heated cold-seal pressure vessels for use to 1200°C at 1000 bars. *Mineral. Mag.* **35,** 1003–1012 (1966).
182. Ã, Y. M., Suzuki, A., Ishiguro, T. & Yokoyama, C. Numerical Simulation of Heat and Fluid Flow in Ammonothermal GaN Bulk Crystal Growth Process. **52,** 16–18 (2013).
183. Zieliñska, M., Yavorska, M., Porêba, M. & Sieniawski, J. Thermal properties of cast nickel based superalloys. *Arch. Mater. Sci. Eng.* **44,** 35–38 (2010).
184. Porowski, S. *et al.* The challenge of decomposition and melting of gallium nitride under high pressure and high temperature. *J. Phys. Chem. Solids* **85,** 138–143 (2015).
185. Erlekampf, J. *et al.* Numerical time-dependent 3D simulation of flow pattern and heat distribution in an ammonothermal system with various baffle shapes. *J. Cryst. Growth* **403,** 96–104 (2014).
186. Brice, J. C. & Rudolph, P. in *Ullmanns Encyclopedia of Industrial chemistry* 673–710 (Wiley-VCH Verlag GmbH & Co., 2007). doi:10.1002/14356007.a08_099.pub2
187. Zhang, S., Hintze, F., Schnick, W. & Niewa, R. Intermediates in Ammonothermal GaN Crystal Growth under Ammonoacidic Conditions. *Eur. J. Inorg. Chem.* **2013,** 5387–5399 (2013).
188. Molybdenum Blue. *Wikipedia* (2016). at <https://en.wikipedia.org/wiki/Molybdenum_blue>
189. Chemical Sampling Information: Ammonia. *Occupational Safety and Health Administration* at <https://www.osha.gov/dts/chemicalsampling/data/CH_218300.html>
190. Moram, M. a & Vickers, M. E. X-ray diffraction of III-nitrides. *Reports Prog. Phys.* **72,** 036502 (2009).
191. Darwin M.A., C. G. The theory of X-ray reflexion. Part II. *Philos. Mag. Ser. 6* **27,** 315–333 (1914).
192. Heying, B. *et al.* Role of threading dislocation structure on the x-ray diffraction peak widths in epitaxial GaN films. *Appl. Phys. Lett.* **643,** 643 (1995).
193. Bryant, B. N., Hirai, A., Young, E. C., Nakamura, S. & Speck, J. S. Quasi-equilibrium crystal shapes and kinetic Wulff plots for gallium nitride grown by hydride vapor phase epitaxy. *J. Cryst. Growth* **369,** 14–20 (2013).